UNIVERSITY OF CALIFORNIA
SANTA CRUZ

# EFFECTS OF FRESHWATER FORCING IN THE DYNAMICS OF THE LABRADOR SEA

A dissertation submitted in partial satisfaction of the requirements for the degree of

DOCTOR OF PHILOSOPHY

in

EARTH AND PLANETARY SCIENCES

by

**Saffia Hossainzadeh**

December 2016

The Dissertation of Saffia Hossainzadeh is approved:

_____
Professor Slawomir M. Tulaczyk, chair

_____
Professor Noah J. Finnegan

_____
Professor Emeritus Gary Glatzmaier

_____
Research Professor Wieslaw Maslowski

_____
Tyrus Miller
Vice Provost and Dean of Graduate Studies

Table of Contents

List of Figures

Abstract

Effects of Freshwater Forcing on the Dynamics of the Labrador Sea

Saffia Hossainzadeh

The Labrador Sea is a climatically important region for the entire globe. As one of the main locations of deep water formation, this subpolar sea helps modulate the strength of the Atlantic Meridional Overturning Circulation. The deep water formation rate is influenced by freshwater originating from the Arctic Ocean as well as from the Greenland Ice Sheet. The freshwater entering the sea is then distributed across the Labrador Sea by boundary currents and eddy circulation. In this study we analyze a suite of simulations using a high resolution earth system model, the Regional Arctic System Model (RASM), to explore the freshwater forcing methods needed to properly represent the Labrador Sea dynamics.

The first simulation, the H-case, uses an actively coupled ocean and sea ice models only, with sea surface salinity (SSS) restored to mean climatology. The G-case removed the SSS restoring method and instead incorporated land runoff fluxes from the Coordinated Ocean-Ice Reference Experiments version 2 (COREv2) to evolve SSS. The final simulation, the R-case, is a fully coupled run that relies minimally on reanalysis forcings, but instead allows the coupled model physics to drive the simulation, with air-sea-land fluxes that develop and grow without artificial forcing.

The critical oceanographic conditions that permit deep water formation can be assessed in our model results by analyzing the strength of water column stratification within the Labrador basin. We explore three methods for calculating the mixed layer depth (MLD) methods. The MLD serves as a measure of the vertical extent of conditions amenable to deep convection and as an indicator of the deep water formation rate. We find that all three methods create a MLD signal that overpredicts, as compared to the existing observations, the spatial and temporal extent of water stratification conducive to deep convection in the Labrador Sea. The maximum density gradient (MDG) method produces on average the lowest MLD values, and hence may best represent the intermittent nature of the deep convection process in the region. Out of the three numerical experiments considered in this study, the R-case shows the most realistic depictions of the extent and depth of MLDs when compared to the G and H-cases. However, even in the R-case, the results of this study highlight the need for further improvements of the ability of the model to produce realistic levels of vertical stratification across this critical high latitude ocean basin.

Beyond the MLD analysis, we find that the R-case outperforms the G and H-cases in a number of surface ocean dynamics measures compared to observations. First, it displays a stronger West Greenland Current System (WGCS) from which Irminger Current Anticyclones are generated and buoyancy is distributed across the rest of the

basin. The eddy activity in the R-case is not only more frequent, but the eddies are also more effective at supplying freshwater to the interior Labrador Sea compared to the other two simulations. We find that the salinity gradient within the WGCS and the sea surface height (SSH) gradient across the west Greenland shelf are the strongest in the R-case. These characteristics stem from freshwater entering the region through boundary currents and from local sources. The R-case also displays a realistic seasonal variation of surface hydrography, and it more closely follows the evolution of sea ice on a mean annual basis compared to the G and H-cases. This shows that the coupled modeling framework provides great improvement to the surface dynamics of the Labrador Sea.

Acknowledgements

This work was supported by the U.S. Department of Energy grant DE-SC0007090 and computational resources were provided by the Department of Defense High Performance Computing Modernization Program (HPCMP). I am thankful to Dr. Maslowski and Dr. Osinski who helped me to advance this project. This work could not have been done without the support of many people who have encouraged me to continue working towards what I started. I will always be indebted to my sisters who spent countless hours listening, laughing, and crying with me, solidifying the deepest connections I have on this earth. I am also extremely fortunate to have met many wonderful people throughout this time of my life. I wish I could have spent more time with all of the good people at UCSC and in the scientific community. To my closest friends, you have been invaluable to me, and I thank you for being there for me. Finally, my main advisor, as a shining example of humility, has taught me many lessons that will carry with me in the next chapter of my life.

# Chapter 1: Introduction

## 1.1 Labrador Sea in the Global Climate System

The Labrador Sea is a sub-polar basin in the North Atlantic situated between Greenland and the Canadian landmass of Labrador (Figure 1). It is the only sea that lies along the water export pathway of the two major Arctic outflows, i.e. the Canadian Archipelago and the Fram Strait (Serreze et al., 2006). As such, the Labrador Sea receives relatively large volumes of freshwater from the north (via the Canadian Archipelago, Baffin Bay and Davis Strait) and south (via the East Greenland Current, originating at Fram Strait and continuing via Denmark Strait). Another sub-polar basin of the northern Atlantic Ocean is the Irminger Sea, located adjacent to southeast Greenland. It also receives freshwater from the Arctic and is situated south of Denmark Strait along the main export pathway of Fram Strait. It also receives a small amount of freshwater from the Barents Sea that may flow southward into the Irminger Sea instead of recirculating around Svalbard (Smedsrud et al., 2013; Serreze et al., 2006). The Irminger and Labrador seas also receive input from sub-tropical Atlantic waters, which are high in heat and salt content. These water masses are transported by the North Atlantic Current and, together with the Arctic freshwater outflow, play a major role in determining the hydrography of the two basins, as well as more climatically significant characteristics such as the sea ice extent.


Figure 1: (top) Map of the Arctic and subpolar region. (bottom) Region focusing on the North Atlantic subpolar basins. Abbreviated labels are: G.S (Greenland Sea), B.S. (Barents Sea), N.S. (Norwegian Sea), F.S (Fram Strait), I.S. (Iceland Sea), G.S.R. (Greenland Scotland Ridge), D.S. (Denmark Strait), and B.B. (Baffin Bay).

These northern high latitude ocean basins are particularly sensitive to variations in freshwater inputs. The Arctic Ocean and adjacent Nordic Seas (Greenland, Iceland,

Norwegian, North and Barents Seas), sometimes referred to as the Arctic Mediterranean Ocean, receives runoff from six major rivers draining the Eurasian and North American continents (Aagard & Carmack, 1989; Simonsen & Haugen, 1996). To balance this buoyancy input, ocean currents are critical in exporting this mass and freshwater to the subpolar seas through the two primary pathways out of the Arctic Ocean - the Fram Strait and the Canadian Archipelago. The annual growth, decay, and export patterns of sea ice further modulate the salinity properties of the Arctic basin. Each of the subarctic seas are subject to seasonal ice growth and decay, and harbor a marginal ice zone, a narrow region where the pack ice conditions transition to open ocean conditions. These regions exhibit extreme gradients in albedo, wind mixing regimes, and the stability of the atmospheric boundary layer that can induce large variability in energy and momentum exchange of the air-ice-ocean system, thereby promoting or inhibiting sea ice melt (McPhee et al., 1987). Moreover, the ice-albedo positive feedback process provides a powerful mechanism in this region that is one reason why the rate of surface temperature warming in the Arctic is amplified compared to the rest of the globe (Serreze & Barry, 2011). A net imbalance of atmospheric or oceanic heat fluxes can have cascading effects on the Arctic, including impacts on the stability of the largest freshwater reservoir in the region, the Greenland Ice Sheet (Zwally et al., 2002; Holland et al., 2008; Pritchard et al., 2009).

The confluence of heat, salt, and freshwater in the Labrador Sea from the Arctic and Atlantic oceans is caused by and, in turn, affects global climate through ocean currents and atmospheric fluxes (Rahmstorf, 2002; Srokosz et al., 2012). The large-scale northward surface flow, primarily by the Gulf Stream and North Atlantic currents, is in part due to the response of the Atlantic Ocean to the latitudinal solar flux gradient. Those currents transport heat from lower latitudes into the subpolar seas of the north Atlantic. They are part of the Atlantic Meridional Overturning Circulation (AMOC), which in turn is a component of the global thermohaline circulation (THC). The ocean currents exiting the Arctic are affected by the presence or absence of sea ice cover. The vast majority of ice export occurs through Fram Strait, as a result of the large scale sea ice circulation associated with the Transpolar Drift and the Beaufort Gyre, forced by a dominant high pressure atmospheric circulation pattern, i.e. the Beaufort High, which provides a mechanical boost for the direction of sea ice outflow (Melling 2012). Freshwater that exits the Arctic and spreads around the north Atlantic and the sub-polar seas serves as an increased buoyancy flux, which can reduce the rate of deep water production, which in turn can slow the AMOC (Aagaard & Carmack, 1989; Jones & Anderson, 2008; Talandier et al., 2014). Similarly, the North Atlantic Oscillation (NAO; Wallace & Gutzler, 1981) modulates the strength and direction of westerlies across the Labrador Sea (Hurrell et al., 1995; Delworth et al., 2016). During strong positive NAO phases, a more northward direction of the westerlies brings air from ice-covered lands of Newfoundland, Labrador and Baffin

Island across the Labrador Sea, drawing a large heat loss from the ocean to the atmosphere (Moore et al., 2014). In these years, deep convection can contribute additional mass to the lower limb of the AMOC via the formation of deep water, which eventually spreads southward, driving the overturning circulation (Delworth et al., 2016). That is how global climate is modulated by processes occurring in the Labrador Sea.

The Labrador Sea is one of the few known locations in the global ocean where deep ocean convection occurs (Vage et al., 2009; Pickart et al., 2002; Lavender et al., 2002; Lazier et al., 2002). Convection is a process where a vertical exchange of seawater occurs due to density differences. A common example of shallow convection occurs ubiquitously in the ocean on a daily basis, when the flexing of a mixed layer depth occurs due to the diurnal cycle. Cold night air, combined with the absence of incoming shortwave radiation, causes a heat flux from the ocean to the atmosphere, leaving the surface layer of the ocean with a buoyancy deficit. The surface layer of water then sinks until it reaches a level of similar density so that there is no net buoyancy force on the parcel. Deep convection in the open ocean is a similar process by which surface waters must plunge to great depth in order to reach their neutral buoyancy level.

In the open ocean, several factors favor the occurrence of deep convection. First, the stratification of the water column must be weak. In each of the north Atlantic sub-polar basins where deep convection occurs, the water is preconditioned so that weakly stratified waters are able to accumulate. This is caused by the cyclonic gyre circulation that domes the isopycnals upward, bringing weakly stratified waters towards the surface. In addition, strong buoyancy loss from a cold atmosphere can reduce the buoyancy further, which can contribute towards a growing subsurface water mass that can remain in the water column for multiple years (Visbeck et al., 2009; Pickart et al., 2002). Fringing sea ice cover helps isolate cold air masses that blow off the land from the underlying warmer ocean until they reach far offshore where deep convection can take place. Hence, the presence of sea ice helps to push a strong atmosphere-ocean heat flux over the open ocean where there are deeper parts of the basin (Moore et al., 2014). As surface water releases heat to the atmosphere and sinks, joining a growing patch of homogenous subsurface water, an additional period of atmospheric forcing can destabilize the water column, bringing the necessary buoyancy loss needed to trigger deep, vigorous, and rapid overturning (Marshall & Schott, 1999). Observations indicate that deep convection occurs in plumes that are only 200-1000m wide (Lilly, 1999) and cannot be resolved directly in regional ocean circulation models. Deep convection has been observed to take place on short time scales too, anytime between a few hours and the duration of strong wind events with vertical speeds between 5-10cm/s. (Gascard & Clarke 1983; Lavender et al., 2002).

Then, these localized plumes of deeply convected water masses become baroclinically unstable with the ambient waters and spread laterally. This adds to the deep water component of the AMOC/THC, helping to drive the circulation on a global scale (Marshall & Schott, 1999). Deep convection in the Labrador Sea has strong interannual variability with some periods showing signs of mixing down to only 500-1100m, like during 1994-2002 in Yashayaev and Loder (2009). Other periods resulted in convection down to 2400m, such as during 1987-1994 (Yashayaev & Loder, 2009).

At high latitudes in both hemispheres, deep water masses form via the process described above and propagate into deep ocean basins. In the Northern Hemisphere, deep water is formed primarily in the Greenland, Iceland, Norwegian, Irminger and Labrador Seas (Clarke & Gascard, 1983; Mauritzen, 1996; Vage et al., 2011). It flows along with the deep western boundary currents as well as over bottom topography as gravitationally driven density plumes. The deep water of the Labrador Sea is populated by North Atlantic Deep Water (NADW), a water mass characterized by cold and saline properties, which stems from the deep water formed in the three subpolar basins upstream. The NADW flowing out of the subarctic is relatively fresh compared to its surface inflows due to the role of freshwater in the high latitudes prior to the formation of the deep water mass (Dickson and Brown 1994). The deepest layer in the Labrador Sea, below 2500m is the Denmark Strait Overflow Water

(DSOW). Above it is the Iceland-Scotland Ridge Overflow Water (ISOW) (Dickson & Brown, 1994; Xu et al., 2015). The Labrador Sea Water (LSW), contained at 500-1500m depth, is the final "deep" water mass of the subpolar basin (Xu et al., 2015). It is is formed by atmospheric and meltwater transformation of warm and saline surface waters and by the aid of the cyclonic gyre circulation of the Labrador Sea (McCartney & Curry, 1996). All three components of NADW (DSOW, LSW and ISOW) help form the bottom limb of the AMOC (Sarafanov et al., 2007).

The Labrador Sea undergoes hydrographic variability on annual, inter-annual, and decadal timescales (Houghton & Visbeck, 2002). The temperature and salinity conditions are governed by a mixture of atmospheric and oceanic forcings. A sufficiently weakened oceanic stratification along with an intense heat loss to a cold atmosphere in winter can prompt deep convection to occur, producing LSW. This water mass is characterized by low salinity, temperature, potential vorticity, oxygen and sigma-density ranges of 27.68-27.80 $kg/m^3$ (Talley & McCartney, 1982; Stramma et al., 2004). LSW exits the Labrador Sea in the region north of the Flemish Cap (Stramma et al., 2004) as part of the North Atlantic Deep Water (NADW) and spreads east into the Irminger Sea and south Icelandic Seas (McCartney & Talley, 1982; Dickson & Brown, 1994). It has also been observed as far south as Antarctica where it mixes with Circumpolar Deep Water (CDW) (Yashayaev & Clarke, 2008).

Although the strong wintertime buoyancy loss due to a cold atmospheric forcing is the immediate cause of deep convection in the Labrador Sea, ocean dynamics directly contribute to this process as well. Boundary currents that encircle the basin bring water masses from diverse sources to the perimeter of the Labrador Sea which can mix into the interior basin, affecting its hydrography. Warm, saline Irminger water along the continental slope of west Greenland provides a substantial source of heat. In fact, the net heat loss to the atmosphere that takes place annually across the Labrador Sea is mainly compensated by the lateral advection of warm Irminger water around the basin (Straneo, 2006). This water lies below fresh and cold surface waters of Arctic origin that flow slightly shoreward from the Irminger water core (Myers et al., 2007; Cuny et al., 2002). Rapid (within two months) restratification occurs in the months following deep convection (Yashayaev & Loder, 2009). Throughout the year, fluxes from the rim currents by mesoscale eddies bring less dense shelf waters into the interior. In addition, the accumulation of intermediate water masses that have been altered by atmospheric forcing can remain over many seasons and precondition the Labrador Sea for an intense convection season (Pickart et al., 2002). Thus, regional processes affecting the lateral buoyancy transport into and within the Labrador Sea are critically important to deep convection, which has repercussions for the global thermohaline circulation.

The hydrological cycle in particular has been implicated as having caused large scale changes in global climate through disruptions in AMOC in the historical and geologic past (Mjell et al., 2016; Rahmstorf et al., 1995). Recent increases in freshwater storage in the north Atlantic due to increased river runoff and Greenland mass loss have caused a weakening of the AMOC since the mid '70s (Rahmstorf et al., 2015). The freshening trend in the upper 1000m of the Nordic Seas may reduce the intensity of the overflows into the subpolar basins (Irminger and Labrador Seas). A further accumulation of freshwater or a reduction of the density gradient across the straits and ridges between the Nordic Seas and subpolar basins could catastrophically disrupt the AMOC (Curry & Mauritzen, 2005). Although instruments monitored since 2004 estimate a declining AMOC strength, the cause of this and its relationship to the north Atlantic freshwater is still unclear since overflow rates across the ridges in the Nordic Seas remain constant during this time (Smeed et al., 2014). The sensitivity of LSW production rates, and therefore AMOC strength, on freshwater is still unclear, especially on our decadal-scale observational time series (Yang et al., 2016).

## 1.2 Oceanography of the Labrador Sea

The Labrador Sea is situated south of Davis Strait between Canada and Greenland and has a wide connection to the Atlantic Ocean in the south (~48°N) (Cuny et al., 2002). It consists of a deep (more than 3500m) basin that is flanked on the east and west by steep continental slopes, with the eastern one being the steeper one of the

two. The northern boundary of the basin has relatively gentle slopes slopes until the 1000m isobath where it narrows and levels off until its northern limit, Davis Strait. The dominant ocean circulation pattern of the Labrador Sea consists of a cyclonic gyre that follows the perimeter of this basin, with strong eastern and western boundary currents, and a weaker recirculation along the northern boundary of the basin. As the East Greenland Current rounds the southern tip of Greenland, it becomes the West Greenland Current (WGC), flowing primarily northwestward. WGC creates the eastern leg of the cyclonic gyre. As the bathymetry shallows towards the northern end of the Labrador basin, much of the WGC flow is deflected westward following the 1000-3000m isobaths (Lavender et al., 2000). The western leg of the gyre, the Labrador Current, flows south and carries Arctic-origin fresh water at its surface from the Baffin Island Current and the Hudson Strait Current (Lazier & Wright, 1993; Schmidt & Send, 2007). There is also a deep western boundary current (DWBC) flowing in a similar cyclonic pattern at depths below 1500m (Pickart & Smethie, 1998). The Labrador Sea cyclonic circulation pattern is a key factor that helps to precondition the region for deep water formation, by doming isopycnals upward and bringing weakly stratified water masses from deeper depths toward the surface (Pickart et al., 2002).

The eastern leg of the Labrador Sea gyre, also referred to as the West Greenland Current System (WGCS), consists of a surface, intermediate and deep component

(Rykova et al., 2015). The surface current is centered along the outer continental shelf region and consists of Arctic origin waters. The intermediate depth waters travel mainly over the continental slope and contains warmer but saltier Irminger Current waters. The WGCS flows northward along the coast of west Greenland beginning at Cape Farewell. There may also be a narrow coastal current along west Greenland driven by continental runoff, similar to the East Greenland Coastal Current, but this has not yet been confirmed by observations (Bacon et al., 2008). Beginning at the 3000m isobath through the 1000m isobath marking the northern boundary of the central Labrador basin, the West Greenland Current System splits, and a significant portion of the flow veers westward following f/H contours. The remaining flow continues northward reaching Davis Strait (Cuny et al., 2002). Beginning offshore of Cape Desolation (~59.5ºN) and further north along the continental slope of Greenland, the WGCS flows over a steepening in the bottom topography where the 500-2500m isobaths merge closely together. This region causes the current to become dynamically unstable and has been called the 'bathymetric gap' (Wolfe & Cenedese, 2006). A large number of mesoscale eddies is generated in this region up to a latitude of ~63ºN, where the 1500m isobath, one of the most shallow isobaths bounding the Labrador Sea, diverges from the coast. Both the westward recirculation, creating the cyclonic gyre, and the large production of eddies play important roles in the deep convection and restratification cycle of the Labrador Sea. A schematic diagram

Figure 2: This plot, originally published by Rykova et al. (2015), shows the main dynamic features of the Labrador Sea that are highlighted in this study. The currents of the Labrador Sea, the West Greenland Current (WGC), Irminger Current (IC), and the Labrador Current (LC), create a cyclonic gyre around the basin. Also depicted in blue the major formation region of Labrador Sea Water (LSW). Green and yellow circular arrows indicate the production and spreading of anticyclonic eddies from the steep continental slope.

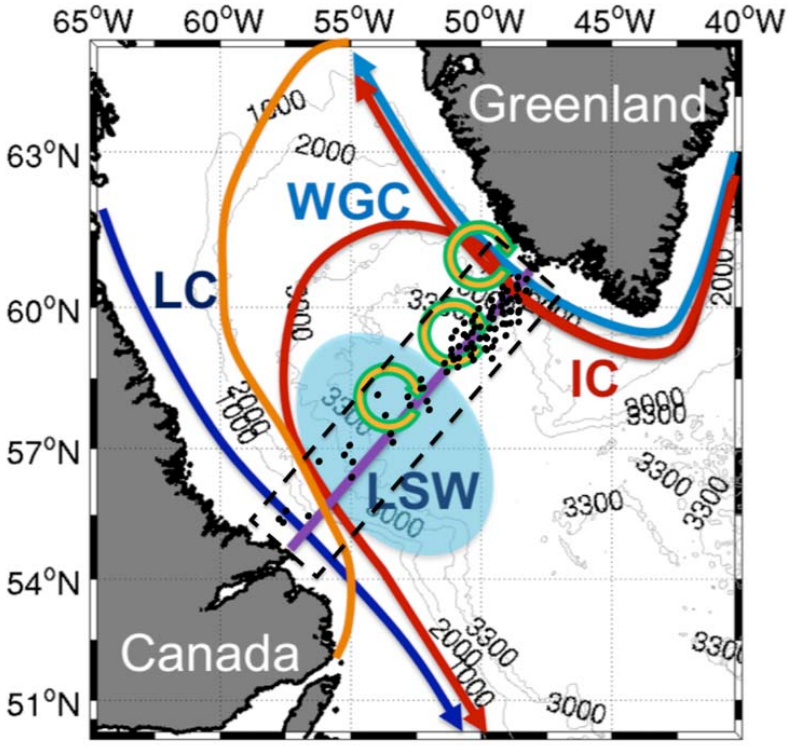


depicting positions of these main dynamic processes, including both eddies and boundary currents, is given in Figure 2.

There are three types of mesoscale eddies found in the Labrador Sea: Irminger Current Anticyclones spawned off the coast of west Greenland, convective eddies that are produced after formation of deep convection patches, and boundary current eddies

(BCEs) that arise from instabilities in the flow of the boundary current and its frontal structure and the quiescent, weakly stratified interior (Chanut et al., 2008; Marshall & Schott, 1999). Irminger Current Anticyclones (ICAs), or Irminger Rings (IRs), and BCEs are the two types of eddies that are shed from the WGCS. They serve as important mechanisms for mixing shelf and interior waters, and can aid or obstruct deep convection. Both arise from baroclinic instabilities, though IRs may also arise from a barotropic instability (Eden & Boning, 2002; Brandt et al., 2004; de Jong et al., 2014). BCEs are generated from the sharp density front created by the warm Irminger-core boundary current and the cold interior Labrador Sea (Gelderloos et al., 2011). ICAs, or IRs, are produced from a steepening of the topographic slope beginning at Cape Desolation and continuing downstream along the coast of west Greenland (Gelderloos et al., 2011; Katsman & Spall, 2004; Eden & Boning, 2002; Chanut et al., 2008; de Jong et al., 2014).

ICAs (or IRs) are anticyclonic, ~30-50 km in diameter and, following the naming convection of Rykova et al., (2009), they can be convected or unconvected depending on whether or not they have undergone a wintertime buoyancy loss. IRs with fresh but cold surface properties, also called fresh-top eddies, can be particularly critical in inhibiting deep water formation, though observations of these eddies have been sparse (Hatun et al., 2007; Rykova et al., 2009). During the restratification period, these eddies can bring lighter waters from the shelf into the interior. During winter, they

can also transport dense water from the marginal ice zones into the interior. They are also thought to be a controlling factor in the position of the present day deep convection site in the southwest Labrador Sea. Other regions of the sea, such as in the northeast along eastern boundary, are not known locations of deep convection because of their proximity to the eddy generation region which transport shelf-derived lighter water masses into the deep basin, disrupting any deepening mixed layer depth that could be occurring (Pickart et al., 2002; Hatun et al., 2007).

## 1.3 Previous Ocean Modeling

Global and regional modeling studies of the north Atlantic Ocean have suggested that the rate of deep water formation will slow under increasing freshwater fluxes to the ocean as the Arctic undergoes an amplified response to climate change compared to the rest of the globe (Junclaus et al., 2006; Weijer et al., 2012; den Toom et al., 2014). However, there is a spread in sensitivity of the AMOC to details surrounding the freshwater forcing, resolution, and model configurations used in models (Yu et al., 2016). Many model configurations have insufficient resolution to resolve coastal and boundary currents or to adequately resolve mesoscale eddies and account for their impacts (Myers et al., 2005; Marsh et al., 2010). These processes have far-reaching consequences that ultimately result in redistributing freshwater from the coast to the interior to modulate deep convection and the AMOC. A recent study showed that resolving the timing and location of Greenland runoff, a potentially large contributor

to freshwater transport by the WGCS, can greatly impact its effect on convection in the Labrador Sea (Dukhovsky et al., 2016). Atmospheric conditions can directly and indirectly prime the ocean to undergo deep convection. Wind direction can control the dominant path of the WGCS, either promoting a northward route along the shelf into Baffin Bay or promoting eddy activity near the bathymetry gap during seasonal cycles (McGeehan & Maslowski, 2012; Luo et al., 2016). Thus, modeling this complex region requires high resolution model configurations where atmosphere, land runoff and ocean components of the earth system are together influencing Labrador Sea dynamics.

Labrador Sea modeling studies have naturally sought the highest resolution possible at the limits of computational resources because of the eddy processes that are critical to accurately represent its role in the global climate (Eden & Boning, 2002; Chanut et al., 2008). The eddy field, essential for redistributing boundary current waters into the basin interior, is made up of eddies that are at the length scale of the Rossby radius of deformation (~7-13km horizontally) (Gascard & Clarke, 1983; Brandt et al., 2004; Luo et al., 2011). Many studies have compared high resolution (1/10° or 1/12°, eddy permitting) to low resolution (1° or 1/4°) models and have shown that the lower resolution models do not transport sufficient freshwater from the boundary currents to the interior (Treguier et al., 2005; Rattan et al., 2010). Saenko et al. (2014) showed that parameterized eddies in a 1° model redistribute the boundary current properties

locally without creating the active region of high eddy kinetic energy near Cape Desolation, as was present in their 1/12° model and seen in drifter and altimeter observations. The rate of decline of the AMOC differs between a regular IPCC type of global model compared to a strongly eddying model (1/10° or 1/12°), with the higher resolution model exhibiting a more gradual decline (Weijer et al., 2012; den Toom et al., 2014). Mesoscale variability in sea surface salinity can produce a difference in surface buoyancy uptake or loss, which may be responsible for the more slowly declining AMOC in the runs with higher resolution (Weijer et al., 2012). Representing the boundary currents themselves are a feature that many global models miss, as global models at 100km horizontal resolution can not even define the bathymetry of the continental shelves. Sharp fronts and narrow boundary currents promote instabilities of the current so that eddies are spawned (Saenko et al., 2014; Chanut et al., 2008), and the water properties that are carried with them are crucial for the Labrador Sea seasonal restratification (Straneo, 2006; Chanut et al., 2008). This is represented more realistically with higher resolution models (Eden and Boning, 2002; Chanut et al., 2008; Gelderloos et al., 2011; McGeehan & Maslowski, 2011; McGeehan & Maslowski, 2012; Zhu et al., 2014).

The freshwater that is contained in the boundary currents of the Labrador Sea, specifically the WGCS, is another significant characteristic that models must capture in order to accurately simulate the Labrador Sea (Myers et al., 2005). The surface

component of cold, freshwater and the subsurface component of warm, Irminger water are the two sources of buoyancy crucial for the seasonal restratification cycle (Straneo, 2006; de Jong et al., 2014). The frontal structure of the boundary current over the shelf, with a high salinity gradient, is enhanced by seasonal fluxes of freshwater which in turn accelerates the current (Schmidt & Send 2007; Rykova et al., 2015). This causes the current to be more unstable and shed more eddies. The freshwater carried by the WGCS and enhanced by local sources are thought to cause the lower MLDs in the northeast Labrador Sea and need to be present in order to properly represent the spatial distribution of deep convection, with the deepest mixed layer depths occurring in the southwest Labrador Sea (Myers et al., 2009; McGeehan and Maslowski 2011; Saenko et al., 2014).

Often, freshwater sources from land runoff are neglected in models, including the large local reservoir of freshwater, the Greenland Ice Sheet (GrIS). With a negative and accelerating mass balance, in fifteen years (1995-2010) GrIS has produced an anomalous freshwater flux on the same order of magnitude as the Great Salinity Anomaly of the ’70s (Velicogna et al., 2009; Bamber et al., 2012). It is projected to continue losing mass, and its surface mass balance is expected to be the dominant source of mass loss once tidewater glaciers retreat above sea level (Vizcaino et al., 2013; Fettweis et al., 2013). This precludes any significant ice dynamical response, as has been implicated in past climate changes, where sea level rapidly rose several

meters per century (Allison et al., 2009). By 2100, the GrIS total surface mass balance is projected to be increasingly negative, between 200 and 1600 Gt/yr relative to the 1980-1999 mean, by a suite of forcing scenarios produced for the IPCC (Fettweis et al., 2013). The Greenland Ice Sheet has already repeatedly broken melt records since the mid '90s, culminating in the historic whole-ice sheet surface melt event in July 2012, which have been linked to NAO influenced atmospheric circulation patterns (Hanna et al., 2014; Fettweis et al., 2013). Recent rapid retreat of the ice sheet's tidewater glaciers in the past two decades have shown the large variability on interannual time scales that can occur as a result of ice dynamics (Moon et al., 2008; Moon et al., 2012). In addition, warm ocean waters that can reach glacier termini in Greenland fjords may increase melt at marine glacier termini that may represent a destabilizing mechanism (Jackson et al., 2014; Nick et al., 2012; Holland et al., 2008). Therefore, with the potential of a growing buoyancy flux supplied to the seas adjacent to Greenland by climate induced dynamic and surface mass loss of the ice sheet, models are well poised to investigate the implications of the increased melt on ocean dynamics.

With the growing freshwater flux entering the ocean and the dynamic implications of salinity gradients across the WGCS, mesoscale variability in the surface salinity field is critical in the study region. The sea surface salinity restoring method, however, smooths this variability in numerical models since the data sets that the surface

salinity are restored to lack the resolution needed to capture the freshwater distribution, especially along the shelves in the Labrador Sea (Chanut et al., 2008). So, when the ocean model is being restored to such a coarse resolution salinity field, the dynamics that result from the salinity gradients are being suppressed in model simulations. Marsh et al. (2010) used an eddy permitting model (~16km horizontal resolution) with spatially realistic freshwater fluxes from post 1990's Greenland mass balance estimates to study the freshwater impacts on Labrador Sea dynamics, but also kept sea surface salinity restoring to maintain realistic overturning rates. They found that very little freshwater was transported into the interior basin, and it had an indiscernible effect on deep convection. Using a much higher resolution model (4-5km) and no SSS restoring for the majority of the simulation, Kawasaki and Hasumi (2014) were able to simulate realistic levels of eddy kinetic energy and mixed layer depths in the southwest Labrador Sea. They attribute this to the realistic freshwater distribution in the WGCS which was left in tact by opting out of SSS restoring. In addition, their study showed that the WGCS provides a significant source of buoyancy not only from heat but also from freshwater to the Labrador Sea interior (Chanut et al., 2008; de Jong et al., 2014; Straneo, 2006). Thus, more realistic treatments of freshwater inputs are necessary, where SSS restoring is less favored compared to freshwater fluxes originating from their natural points of entry and where ocean dynamics are allowed to redistribute and control the fate of freshwater inputs.

For over a decade, climate models have been assessing the impacts of Greenland freshwater on AMOC and deep convection in the Labrador Sea (Gerdes et al., 2005; Van den Berk & Drijfhout, 2014; Boning et al., 2016). The need for higher resolution modeling studies was identified and demonstrated to produce observed levels of eddy kinetic energy but the salinity distribution in the Labrador Sea remained problematic (Marsh et al., 2010; Weijer et al., 2012; McGeehan & Maslowski, 2011; den Toom et al., 2014). More sophisticated freshwater treatments, without the SSS restoring, and with more complex forcings from atmosphere and land models are now beginning to be utilized to improve the Labrador Sea simulations (Yu et al., 2016). Coupled models allow for counteracting heat and salt advection feedbacks to develop. The presence of a dynamic atmosphere and sea ice, especially over the Labrador Sea, may allow large scale circulations to develop due to the ocean's sensitivity to surface conditions (Gerdes et al., 2005; den Toom et al., 2014). A recent paper highlighted the use of a coupled global ocean/sea ice, land and atmosphere model where the surface melt from Greenland was parameterized based on atmospheric temperatures (Lenaerts et al., 2015). This was the first attempt at a fully coupled modeling framework to assess the variability of the AMOC based on increased meltwater fluxes in Greenland. However, at a 1° global resolution, it faces the same shortcomings in reproducing sufficient eddy activity as earlier studies.

In the current investigation, the impact of the freshwater treatment in a regional scale eddy permitting model with varying model configurations is analyzed. The merits of SSS restoring on the Labrador Sea eddy field are directly assessed by comparing such a simulation to a more realistic freshwater treatment where runoff from Greenland is accounted for as a swath of freshwater flux to the ocean model. This study examines if high resolution simulations with a realistic freshwater forcing can simulate a more realistic eddy field in the Labrador Sea, and if SSS restoring may be doing more harm than good in such high resolution simulations. The final component of the study analyzes the results of a fully coupled model at eddy-permitting resolution. This is the first fully coupled model at 1/12° resolution covering the Labrador Sea within the pan-Arctic domain (Maslowski et al., 2012) that the author is aware of.

The following section will further explain the suite of model simulations that were executed by Drs. Robert Osinski and Wieslaw Maslowski. The author, Saffia Hossainzadeh, subsequently analyzed each of the selected simulations and compiled the results in the following dissertation. The remaining sections in this chapter cover a detailed explanation of the model configurations, including differences in the freshwater forcing between the simulations. In Chapter 2 the surface conditions in the Labrador Sea are compared to observations as well as between each of the models. The next chapter focuses on the evaluation of mixed layer depth and the vertical stratification in the interior basin. The final chapter of analysis, Chapter 4, evaluates

the generation of eddies and the resulting transport of freshwater to the interior before a general conclusion in Chapter 5.

## 1.4 RASM Configuration: G, H and R-cases

The Regional Arctic System Model (RASM) is a fully coupled regional model focusing on the northern polar regions of the globe (Maslowski et al., 2012; Roberts et al., 2015; DuVivier et al., 2016; Hamman et al., 2016a; Hamman et al., 2016b). In this study, we investigate how RASM's treatment of freshwater inputs in the Labrador Sea affects simulated eddy production and boundary current properties. RASM's domain includes the central Arctic Ocean, its marginal seas and extends southward of 30° latitude in the Pacific Ocean, and southward of 45° in the Atlantic Ocean. Having such extensive domain boundaries allows storms to develop and migrate to the polar and subpolar regions, and the total runoff accumulated in each drainage basin entering the Arctic Ocean is accounted for (Hamman et al., 2016b). The ocean model, Parallel Ocean Program (POP), and the sea ice model, or Community ICE (CICE), are actively coupled on the same grid at $1/12^{o}$ or ~9km horizontal resolution. The bathymetry of the POP domain used in RASM is shown in Figure 3, with the black rectangle depicting the focus area of this study, i.e. the Labrador Sea region. The atmosphere, Weather Research and Forecasting (WRF), and the land hydrology model, Variable Infiltration Capacity with river routing scheme (RVIC), are

Figure 3: The bathymetry (m) of the POP domain in RASM is shown above. Horizontal resolution is 1/12º. The box outlined indicates the study region used in subsequent analyses.

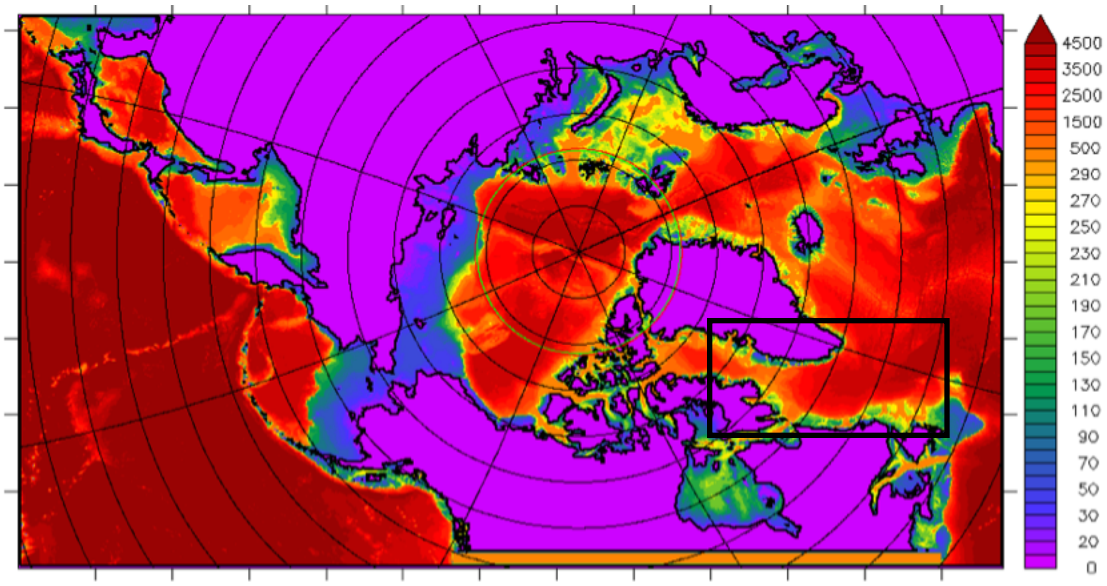


configured at a 50 km resolution. All model components are coupled via the flux coupler (CPL7; Craig et al., 2012) at a high temporal frequency.

POP was developed at Los Alamos National Laboratory and is part of the Bryan-Cox-Semtner class of ocean models (Smith et al., 1992; Semtner, 1988). It solves the primitive equations in three dimensions with the hydrostatic and Boussinesq approximations on a B-grid. The lateral and bottom boundary conditions are no flux for tracers and no-slip for velocities. The surface allows for forcings from buoyancy fluxes and wind stress. The horizontal grid-spacing in this model is 1/12° (~9km) (increasing resolution in the latitudinal direction), with 45 fixed-depth z-levels of increasing thickness in the vertical direction. The vertical resolution decreases from 5

Figure 4: The bathymetry (m) within the study region. (a) The bathymetry with a rectangle of the interior Labrador Sea outlined in black, and the mean surface freshwater analysis outlined in blue. (b) The transect line locations are indicated on this map.

a)

b)

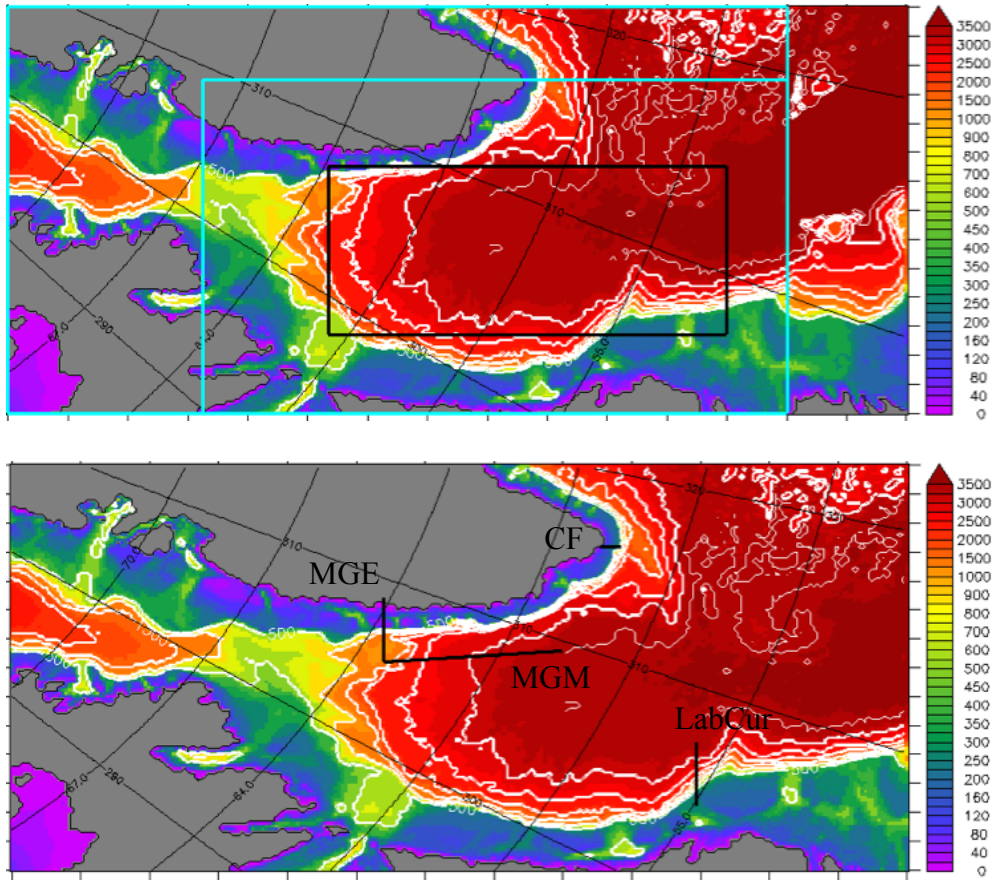


m in the upper 20 m to 300 m resolution below 4750 m. At the horizontal resolution used in RASM, POP is eddy permitting, but not eddy resolving, at all latitudes including the Labrador Sea region (Osinski et al., 2010). The bathymetry of the study region outlined in Figure 3 is shown in Figure 4, with labeled transect lines and sub-regions outlined that are used in subsequent analysis.

We analyze output from three RASM simulations for its ability to represent ocean dynamics in the Labrador Sea. First, we analyze two model simulations that differ from each other only in the treatment of freshwater forcing to the ocean. The first simulation, labeled as H-case, runs RASM in an actively coupled POP-CICE model only, forced with atmospheric reanalysis. The sea surface salinity (SSS) is restored to monthly mean climatology (the PHC data set; Steele et al., 2001), as it has been commonly practiced in ocean-sea ice modeling (Gerdes et al., 2006). In the second run, called G-case, the model configuration is exactly the same as in the H-case except that the ocean SSS is free evolve under the prescribed realistic forcing from the atmosphere and from land (i.e. runoff) buoyancy fluxes to the ocean. This approach allows interannual variability in runoff and surface buoyancy fluxes due to net precipitation and land runoff. We compare the results of the SSS-restoring run (H-case) with an interannually varying freshwater forcing case (G-case).

The third simulation, the R-case, utilizes the fully coupled RASM, with RVIC, WRF, and POP-CICE all actively coupled. One of many differences in the R-case is that this version of the model requires no data set to force POP-CICE, except at the lateral boundaries, and that WRF uses spectral nudging applied to the upper half of the atmosphere. The atmosphere and land models interact with the ocean and sea ice models in a fully consistent manner so that fluxes are passed and evolve realistically

in each model. WRF is coupled every 20 minutes to POP-CICE, enabling a very realistic wind forcing and ice-ocean response to it, resulting in the resolution of inertial oscillations. Compared to the G and H-cases, the overall skill in the R-case in reproducing ocean dynamics in the Labrador Sea is similar to the forced models.

## 1.5 Resolution and Topography on Eddy Generation

The ability for eddies to form and develop in RASM's Labrador Sea is of fundamental importance in this study. The first baroclinic mode of the Rossby radius of deformation, $L_{def}$, is used to define the minimum lengthscale that mesoscale eddies can form (Kantha and Clayson 2000). At this length scale, rotational effects govern the adjustment and smoothing that an ocean perturbation receives and eddies are formed (Gill 1982). The greatest variables in an ocean Rossby radius are its stratification and latitude, since $L_{def} = c_1/f$, and $c_1$ is the first mode of the baroclinic internal gravity wave speed, which depends on the ocean stratification, and f is the Coriolis parameter for Earth's rotation rate, which is a function of latitude (Saenko, 2006; Gill, 1982).

Previous studies have calculated $L_{def}$ from model outputs. The first such study by Chelton et al. (1998) reached up to 60ºN, capturing the southern end of the Labrador Sea with an estimated $L_{def}$ of approximately 10km. Later, a study by Nurser and Bacon (2014) evaluated $L_{def}$ in the same way but focused on the Arctic Ocean and its

Figure 5: The all-time mean potential density profiles (left) for the top 20 layers and the all-time mean buoyancy frequency (right) for the entire column of the main Labrador Sea region indicated in Figure 4 for all model simulations and the PHC data set.

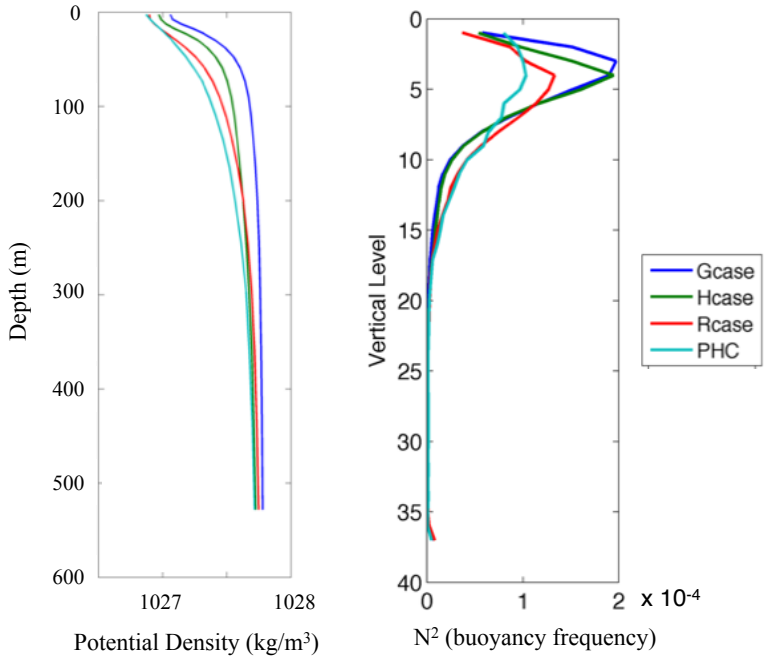


sub-polar seas. This provided detailed maps of the geographically varying field but still missed the bulk of the Labrador basin. To display an order of magnitude estimate of $L_{def}$ focusing on the Labrador Sea, this study follows the same prior methods and calculate the all-time mean buoyancy frequency, $N^2(z)$, for the G,H, and R-case model simulations as well as the buoyancy frequency of the PHC reanalysis (Steele et al., 2001). $N^2(z)$ is then used to find the speed of the first mode of the baroclinic gravity wave speed, and hence $L_{def}$. In Figure 5, the mean potential density and buoyancy frequency profiles in this region are shown, which control the speed of $c_1$.

The results of both the Rossby radius of deformation and the first mode baroclinic wave speed are shown in Figure 6, which encompasses the region outlined in cyan in Figure 4. All of the calculations are in general agreement, with the PHC exhibiting ~2km larger $L_{def}$ values than all other cases. Though not apparent from the single average density and buoyancy frequency plots of Figure 5, the PHC has a higher stratification in the interior than the models, which results in the large Rossby radii. The results also show significant variation in $L_{def}$ between the shelf and the interior basin, with lower values occurring along the shelves in all cases. The shallow water depths along the shelves control to a large extent the lower $L_{def}$ values (through smaller $c_1$ compared to the interior basin). Buoyant surface water due to local freshwater runoff and upstream coastal currents can also reinforce lower Rossby radii along the coasts. These freshwater conditions act to increase the stratification of the water column, thereby decreasing the wave speed.

Although typical $c_1$ speeds in the mid-latitudes are 2-3 m/s, in the higher latitudes they decrease to less than 1 m/s (Kantha & Clayson, 2000; Rainville & Pinkel, 2006; Saenko, 2006). A single measurement of the gravity wave speed in the south western Labrador Sea, interior of the continental slope by Wain et al. (2015) determined a velocity of 0.3 m/s at 60m depth. The calculated wave speeds shown here (Figure 6)

Figure 6: top row: The Rossby radius of deformation (km) for the Labrador Sea region, $c_1/f$; bottom row: the first mode of the baroclinic internal gravity wave speed, $c_1$, (m/s) calculated from the all-time mean G, H, R and PHC hydrography.

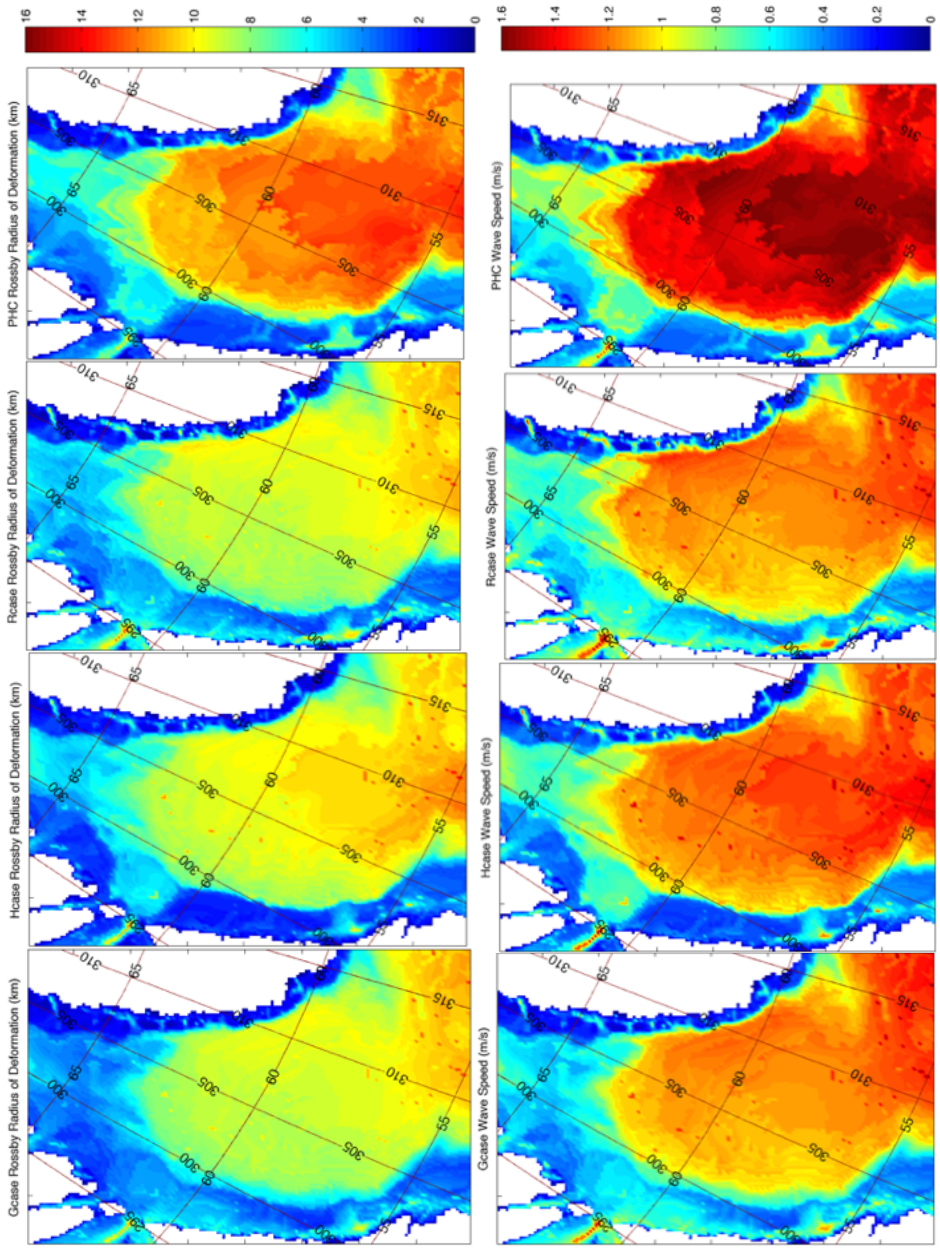


are in agreement with the general trend of decreasing values with higher latitude and with the single measurement in the region.

Averaging the typical coastal and interior $L_{def}$ value within the Labrador Sea focus area gives an order of magnitude estimate of $L_{def}$ that is approximately 10km across all model and climatology based results. This yields RASM as an eddy-permitting model since at ~9km resolution, only 1-2 grid cells can represent a distance equal to $L_{def}$ (McGeehan & Maslowski, 2011; Rattan et al., 2010). However, some studies (Gascard & Clarke, 1983; Lilly et al., 2003) have estimated $L_{def}$ as low as 5-7km, and if local and seasonal variations are taken into account from our maps in Figure 6, the Rossby radius can be as little as ~2km along the shelf of Greenland. Therefore, a higher resolution than this order of magnitude estimate may be needed for a model to capture all the eddy activity generated in this region.

The other aspect of model resolution that plays a critical role particularly in the Labrador Sea is the resolved steepness of model bathymetry, including the 'bathymetry gap.' Studies have shown that coarse resolution studies smooth out this topographic step and greatly reduces the amount of eddies that are shed because the stability of the WGCS depends on the steepness of the bathymetry and the sudden drop in topography after the East Greenland current rounds Cape Farewell (Chanut et al., 2008; Luo et al., 2011; Kawasaki & Hasumi 2014). Here, the bathymetry within the main part of the study region is derived from a 5-minute global grid of the Earth's surface (World Data Service for Geophysics, n.d.), but north of 64º, the bathymetry is derived from the International Bathymetric Chart of the Arctic Ocean at resolution of

Figure 7: (a) Bathymetric slope of the Labrador Sea region used in RASM. The 'bathymetry gap' is clearly visible along the continental slope of southwest Greenland. (b) A histogram of the total range of the slopes shown in the map on the left depicts its unusual and distinct steep slope values along the 'bathymetry gap'.

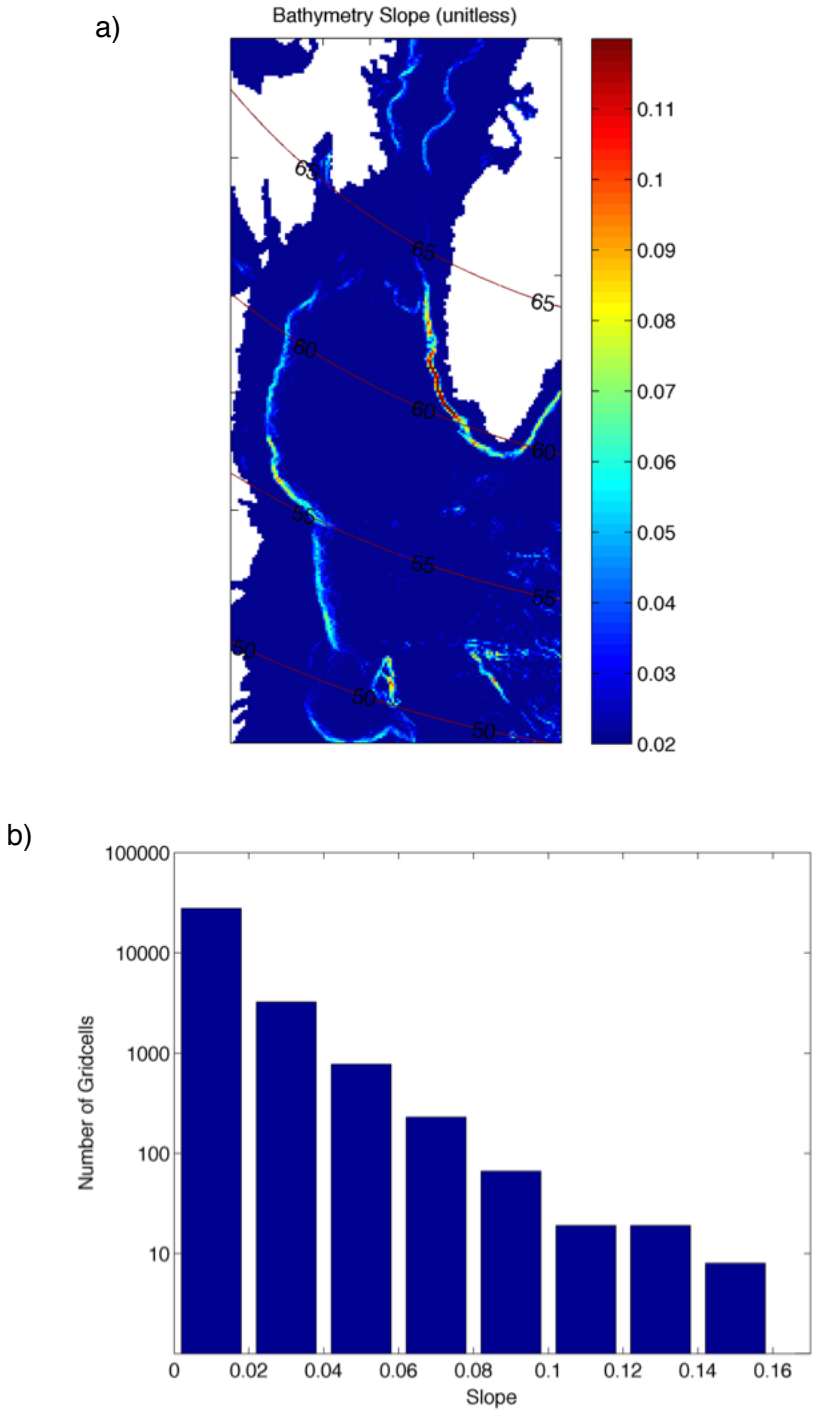

2.5 km (Jakobsson et al., 2000). Based on this data, the slope of the Labrador Sea bathymetry is shown in Figure 7. The 'bathymetric gap' is clearly evident along the slope of west Greenland, with tens of grid cells exhibiting slope values in excess of 0.1. These fall in the range of sufficiently steep bathymetry (~0.06-0.12) that have been shown to be conducive to mesoscale eddy production in numerical simulations (Chanut et al., 2008; Kawasaki & Hasumi, 2014). The steepest slope along the 'bathymetric gap' exceeds 0.15, whereas the average slope outside of this region is 0.02, which is in agreement with RASM bathymetry in this region (Wolfe & Cenedese, 2006).

## 1.6 Model Drift

The G, H and R-cases were initialized with 'cold start' conditions, i.e. with no sea ice cover, no ocean motion and the 3-dimensional January monthly mean PHC climatology for temperature and salinity within the ocean domain. All three cases have been spun up for 119 years before the production run and analysis that began in 1980. With such a long spin up time, the upper ocean is assumed to be in a steady state climate and it should not exhibit a numerical drift (Neelin, 2011). Since most of our analyses revolve around salinity and freshwater dynamics, we analyze any potential drift only in this field. We quantify the underlying trend in the salinity conditions during the analysis period, as shown in Figure 8. We find that the trend, or drift, for each of these runs is negligible, at most 0.004 PSU per 30 years which is

Figure 8: The G, H, and R-case average salinity across the entire domain for all time. The table indicates the constants for the linear fit used to estimate the numerical drift for each case.

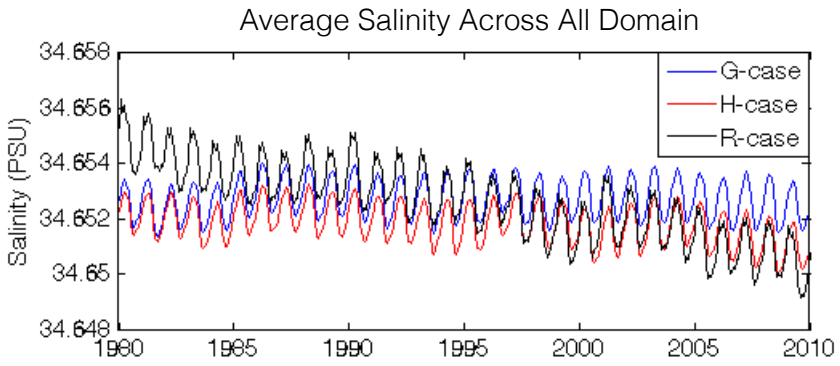


| Linear Fit* | p1 (PSU/ 30 yrs) | p2 (PSU) |
|---|---|---|
| **Gcase** | -0.0000380 | 34.65 |
| **Hcase** | -0.000983 | 34.65 |
| **Rcase** | -0.00448 | 34.66 |

** Linear Fit: D = p1*x + p2*

well below the 0.03 threshold rate of change allowed in an ocean model (sen Gupta et al., 2012). The larger drift in the R-case salinity time series is expected since the R-case introduces more degrees of freedom as a fully a coupled simulation, whereas the G and H-cases are more constrained. Since each of these drift rates are negligible, our model results can be analyzed in terms of external forcings and natural variability.

## 1.7 Freshwater Forcing

The G and H-cases are forced by the National Centers for Environmental Prediction/ National Center for Atmospheric Research (NCEP/NCAR) reanalysis Coordinated Ocean-ice Reference Experiments version 2 (COREv2) data set (Kalnay et al., 1996; Large & Yeager, 2009; Griffies et al., 2009). A freshwater source of precipitation (P) is shared by both simulations as well as solid and liquid river runoff. The precipitation field is based on a blended product using satellite, in-situ and numerical data, the Climate Prediction Center Merged Analysis of Precipitation (CMAP) (Xie & Arkin, 1996). The evaporation field is calculated from model SST and other COREv2

Figure 9: The sea surface salinity remapped onto the RASM grid from the PHC climatology used to restore the H-case simulation.

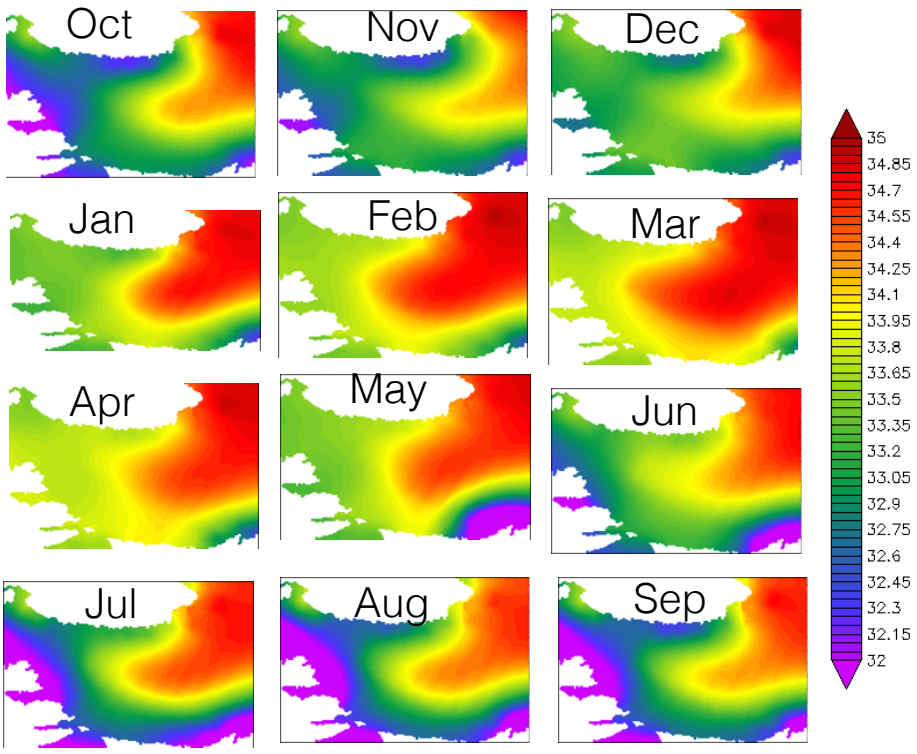

forcing fields such as air temperature, pressure, humidity and wind that determine the turbulent and thermodynamic transfer coefficients (Large & Yeager, 2004).

In the H-case, the SSS in POP is restored to a monthly mean climatology from the Polar Hydrographic Climatology (PHC) at a monthly resolution (Steele et al., 2001). The SSS is remapped by the coupler (CPL7) onto the POP grid from its original projection and 1º global climate model resolution. It is used to force the H-case RASM with an annual cycle repeated throughout the entire simulation. This forcing field is shown in Figure 9. In the G-case, however, the SSS restoring is not used, so SSS is allowed to freely evolve based on surface buoyancy fluxes and runoff. The runoff is taken from the CORE2 data set, it is remapped onto the RASM POP grid, and it is resolved monthly over 1948-2009. This data set captures interannual variability in the freshwater forcing. The all-time mean of the runoff forcing for the

analysis period of the simulation (1980-2009) used in RASM's G-case from CORE2 is shown in the top panel of Figure 10. Similarly, for the R-case, the all-time mean liquid runoff flux from the land model (RVIC) to the ocean model which is calculated and produced throughout the model simulation is given in the bottom plot of Figure 10. Comparison of the land runoff between CORE2 used in the G-case and that produced by RVIC in the R-case shows that the greatest difference emanates from Greenland. This will be discussed further below.

Figure 10: The all-time mean runoff for the G and R-cases in logscale (kg/m$^2$). Though there are some similarities in the spatial distribution of the runoff, the R-case produces a much larger magnitude around Greenland than the G-case.

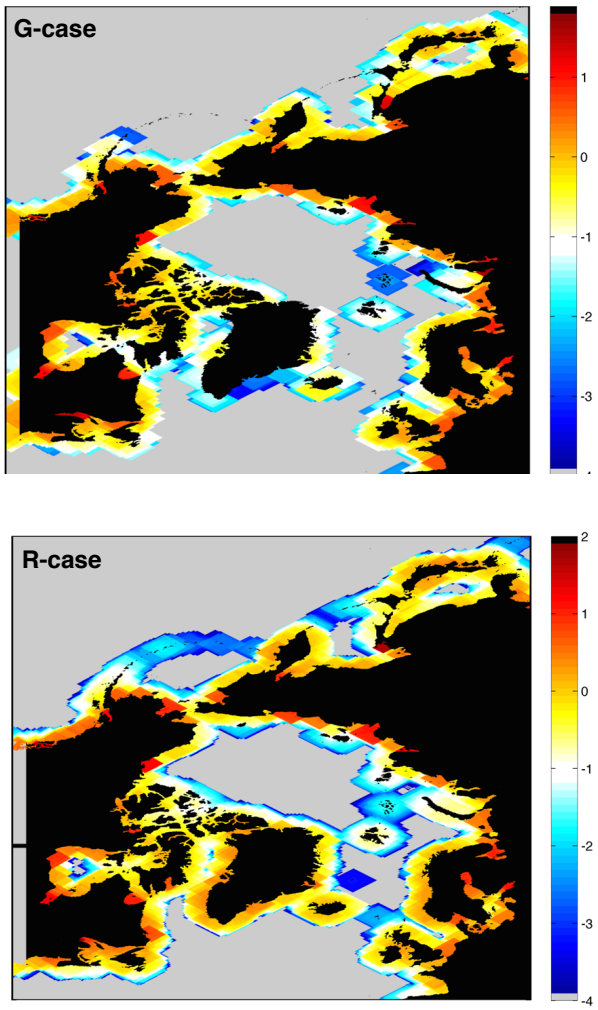


Figure 11 shows the monthly mean total accumulated runoff given to POP from CORE2 (blue curve) across the entire domain in the G-case as well as the equivalent field that is produced by RVIC in the R-case (red curve). There is a strong seasonality in the mean annual cycle of integrated runoff, which peaks in June. Each simulation

produces runoff that varies on a monthly basis, resulting in an interannual variability during the analysis period (1980-2009). The G and R-cases introduce a more physically realistic set-up than the H-case due to this variable runoff forcing. The land runoff in the CORE2 data set is determined by stream gauge records in most of the domain. Net runoff from Greenland, however, comes from a Community Land Model (CLM) hindcast, and only includes the surface surface mass balance term for liquid water runoff (Large & Yeager, 2009 and personal communication).

In the fully coupled R-case, POP receives freshwater from the other model components, i.e. the surface buoyancy terms from WRF and runoff from RVIC. On average across the entire domain, the runoff from RVIC is much higher than COREv2 as is shown by comparing Figures 10 and 11. In the maps of Figure 10, the runoff is plotted after the coupler has remapped the flux from the land grid to the ocean grid. The unsmoothed swaths of colors denote the freshwater flux that the ocean model receives on average from 1980-2009. The R-case has generally larger magnitudes of runoff across the domain than the G-case, particularly around Greenland. In the hydrograph of the net monthly mean runoff (Figure 11) across the entire domain, the R-case produces a factor of two greater flux at its peak than the G-case. In the winter season, RVIC produces slightly less runoff than COREv2, but their values are comparable at ~0.1 Sv. Although the total runoff from the observationally based

Figure 11: The mean annual cycle from 1980-2009 of the total runoff from the entire RASM domain. The R-case produces a May maximum that is about double the magnitude of the G-case runoff peak that also occurs later in June.

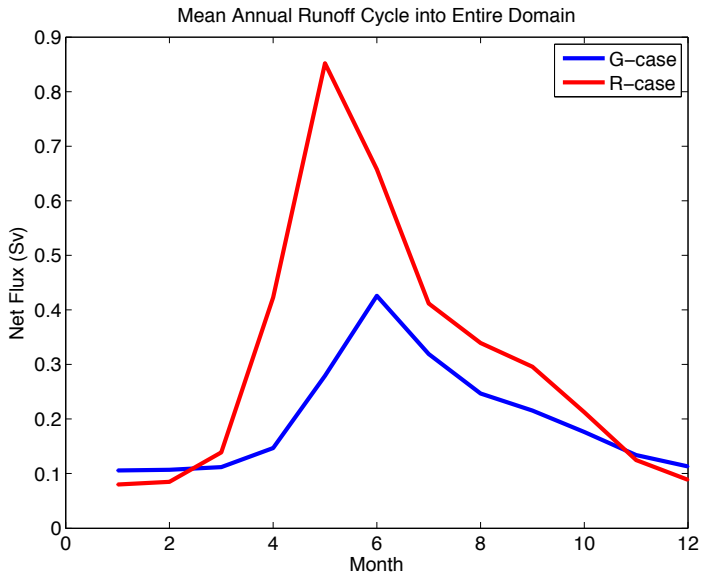


COREv2 and the RASM generated RVIC are comparable, we focus on the runoff from Greenland in the following evaluation.

The mean annual cycle of runoff from Greenland only is given in Figure 12 by the red (R-case) and blue (G-case) curves, depicting RVIC and COREv2 runoffs respectively. RVIC and COREv2 produce similar near zero fluxes during winter. In the summer RVIC produces a maximum flux that is almost an order of magnitude greater than COREv2. Because both sources (COREv2 and RVIC) only account for liquid surface mass balance, there is a near zero winter signal produced for runoff. However, the other main source of freshwater discharge from Greenland comes as solid ice flux,

which accounted for ~40% of the mass loss from 2000-2012 (Enderlin et al., 2014). In Figure 12, we compliment the total runoff mean annual cycle curves from Greenland used in our model simulations with an estimate that includes ice discharge estimates as well as ice sheet and tundra runoff from a regional climate model (Bamber et al., 2012). This freshwater flux estimate is more useful to ocean models because any ice lost from the ice sheet will eventually enter the ocean as freshwater, not only the liquid runoff from the surface. Although our simulations use a mean freshwater flux that does not include ice discharge, the mean surface mass loss due to Greenland produced by RVIC matches the most realistic estimate of the total

Figure 12: Mean annual cycle of the runoff produced by Greenland in the G and R-cases as well as the results from Bamber et al. (2012) which includes both ice discharge and surface melt in their freshwater flux estimate from Greenland. The G-case runoff, determined by CORE2, greatly underestimates Greenland runoff. The R-case, produces reasonable values compared to Bamber et al. (2012).

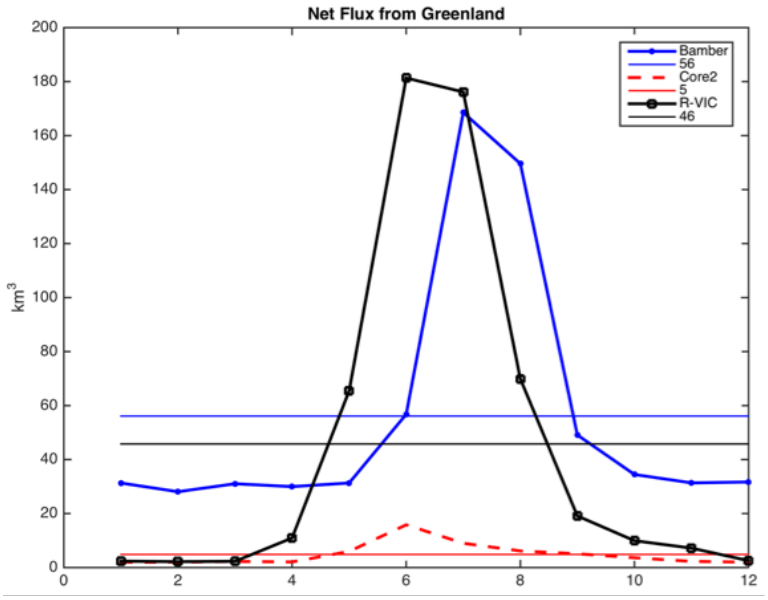

freshwater flux exiting Greenland. This total will enter the ocean and is well represented by the raw RVIC estimation.

The near-zero winter-time flux values seen in both the CORE2 and RVIC hydrograph in Figure 12 differ greatly from the near-constant Bamber et al. (2012) data for this season. This is again due to Bamber et al.'s (2012) inclusion of the ice discharge term in the total mass loss estimation since runoff is near zero during the winter. For ocean modeling purposes, the amount of liquid runoff from Greenland entering the open ocean during winter should be much less than Bamber et al.'s (2012) estimate because much of the newly created icebergs will be locked in fjords that are heavily covered in sea ice, blocking their access to the ocean and producing very little meltwater. Therefore, the near zero flux exhibited by RVIC and COREv2 may be more realistic as the runoff term that enters the open ocean around Greenland.

Although RVIC overestimates the net runoff produced from Greenland and CORE2 underestimates it, we evaluate the interannual variability of Greenland runoff from 1980-2009 produced in our model simulations. This is shown in Figure 13, as a plot of the net annual runoff from Greenland, though the magnitudes of both the G and R-case surface mass balance (SMB) are not in agreement with observations of SMB alone. Observations indicate that the surface runoff and total freshwater flux from Greenland has shown a steady positive trend since the mid 90s (Bamber et al., 2012;

Figure 13: Net annual runoff from Greenland in the G and R-cases. Neither simulation reproduces the observed increase in runoff since the mid 1990s, but they both show a linearly increasing trend of 0.3% per year.

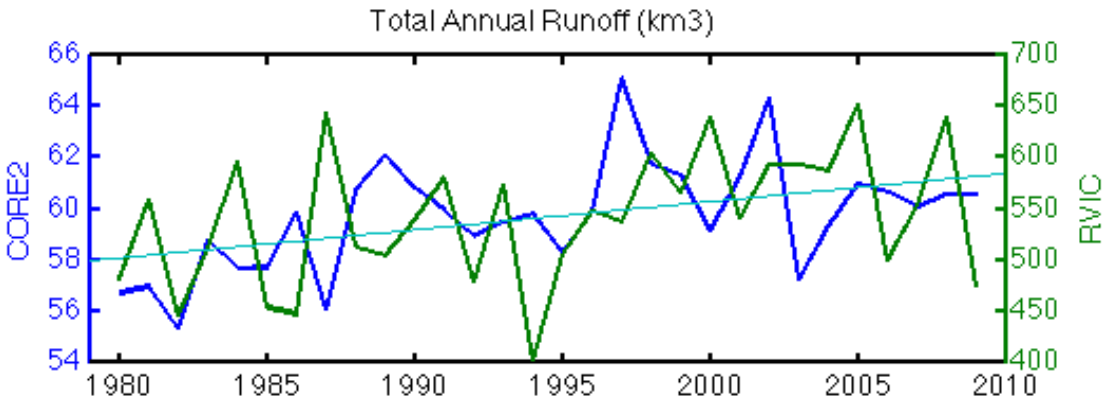


Ettema et al., 2009; Hanna et al., 2011; Howat & Eddy, 2011). A significant trend since the mid-90s is not found in either CORE2 or RVIC's time series. However, they both show the same trend (blue line, Figure 13) of increasing runoff from 1980-2009. The runoff rate is about 0.3% per year, whereas the rate of increase in the surface runoff alone has been ~3% since the mid '90s (Box, 2013; Ettema et al., 2009). This shows that the runoff forcing the ocean in our experiments does not capture the higher frequency variability observed in the climate, though there is a large interannual variability in the SMB trend (Ettema et al., 2009; Hanna et al., 2011). There is only a slight rate of increase in the flux over the 30-year period compared to the much greater observed rate of increase in the final two from 1990-2009. The R-case, with its comparable mean annual cycle to Bamber et al. (2012), forces the ocean model with freshwater fluxes typical of the last two decades throughout the entire run.

Chapter 2: Model Evaluation

## 2.1 Mean Annual Cycle of Near Surface Conditions

### 2.1.1 Comparison of G, H and R-case Salinity, Temperature and Velocity

A first order analysis of how the three different RASM freshwater forcings manifest in the Labrador Sea is highlighted by a comparison of sea surface salinity conditions. The monthly mean surface salinity from 1980-2009 in all three simulations across the Labrador Sea study area (outline by cyan rectangle in Figure 4a) is provided by Figure 14 below. The G, H, and R-cases show a high degree of agreement in July and August before the G-case diverges to a higher salinity state, increasing its salinity difference from the other two simulations during September through February. The H and R-cases are almost equivalent in surface salinity throughout the year, though the R-case is slightly more fresh than the H-case for most of the year. The high salinity of the G-case indicates that insufficient freshwater is brought into the Labrador Sea by ocean currents or runoff compared to the observationally constrained H-case or the

Figure 14: Mean annual cycle of the G, H, and R-case surface salinities averaged across the Labrador Sea study region, indicated by the cyan box above.

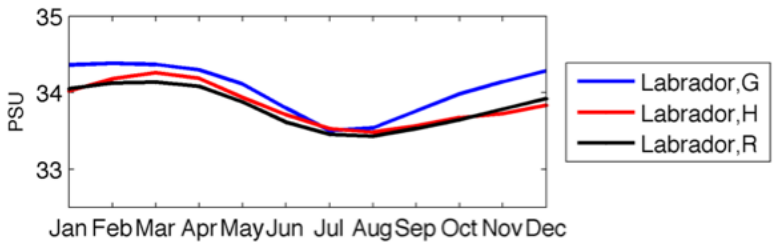

fully coupled R-case. However, the G-case is not uniformly more saline than the R and H-cases in all parts of the study area for the 30-year analysis period. The G-case is more fresh than the H-case along the Labrador shelf in analysis of its mean annual cycle, and the R-case mimics the G-case in this respect but is also more fresh than both the G and H-cases along the west coast of Greenland. This is true all year around, even during the winter months as is shown in Figure 15 below. The R-case also maintains fresher conditions than both the G and H-cases along the coast of Baffin Island.

Figure 15: Mean winter-time 1980-2009 surface salinities for the three cases. Bold velocity vectors show exhibit ranges centered around 40 cm/s while single thickness arrows are less than 20 cm/s.

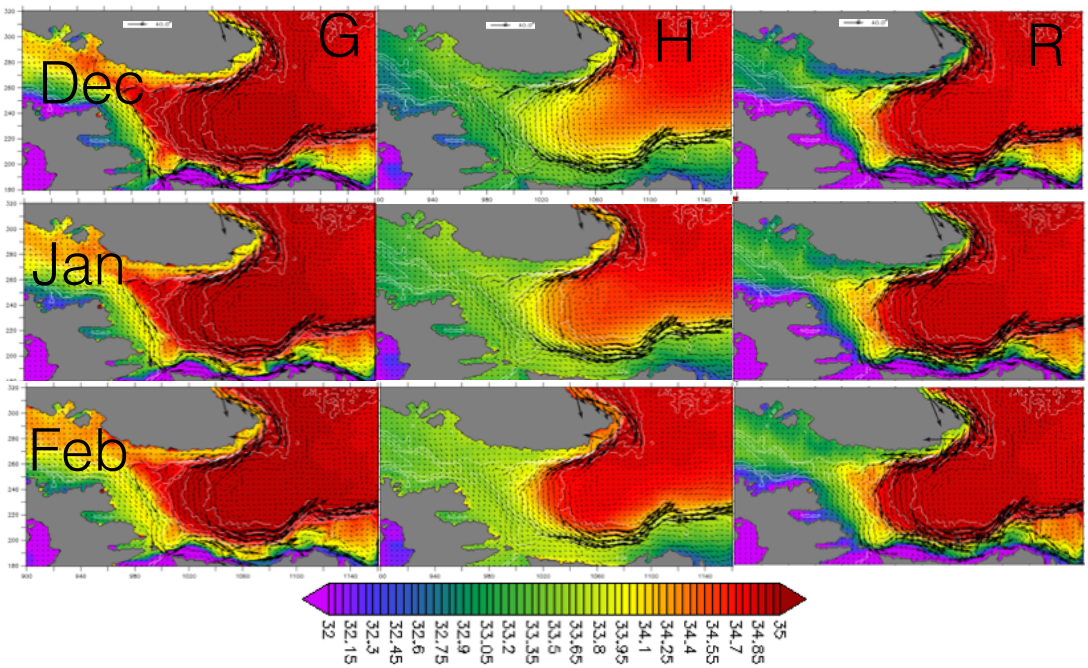

Further offshore from the coasts, the G and R-cases maintain a more saline boundary current flow and recirculation around the Labrador basin throughout the entire mean annual cycle compared to the H-case. The fall period is shown below (Figure 16), where differences in the G and R-cases compared to the H-case are shown for September, October and November in the Labrador Sea study region. The intensity, both magnitude and extent of greater salinity in the G-case, increases in summer through early winter (Figure 16, left side). Especially on the west side of the basin, insufficient mixing of the shelf and interior properties leaves the interior basin too saline. This is similar in the R-case, though the signal is less strong and pervasive. The R-case has an additional distinction of ample freshwater along the Greenland coast on the eastern side of the basin. This subdues the salinity signature in the vicinity and in the northwest of the basin. In fact, featured prominently along the ~1500m isobath (Figure 16, right side), one of the northern most branches of the recirculation currents spreads fresh coastal water towards the interior. This indicates one direct method that freshwater can be mixed into the interior basin. Representation of this freshwater source at the margins of the basin is a critical model feature needed to realistically account for mixing of shelf and interior properties. The R-case uniquely produces such spatial variability, especially on the eastern side of the basin.

There are also spatial patterns in the sea surface temperature difference (G-H and R-H, Figure 17) distributions. Generally, the G and H-cases have comparable

Figure 16: Surface salinity differences between the G and H-cases and the R and H-cases for September, October and November means from 1980-2009. Both the G and R-cases produce more saline cyclonic gyre circulation, and the R-case maintains relatively fresh conditions along the shelf of west Greenland compared to the G and H-cases.

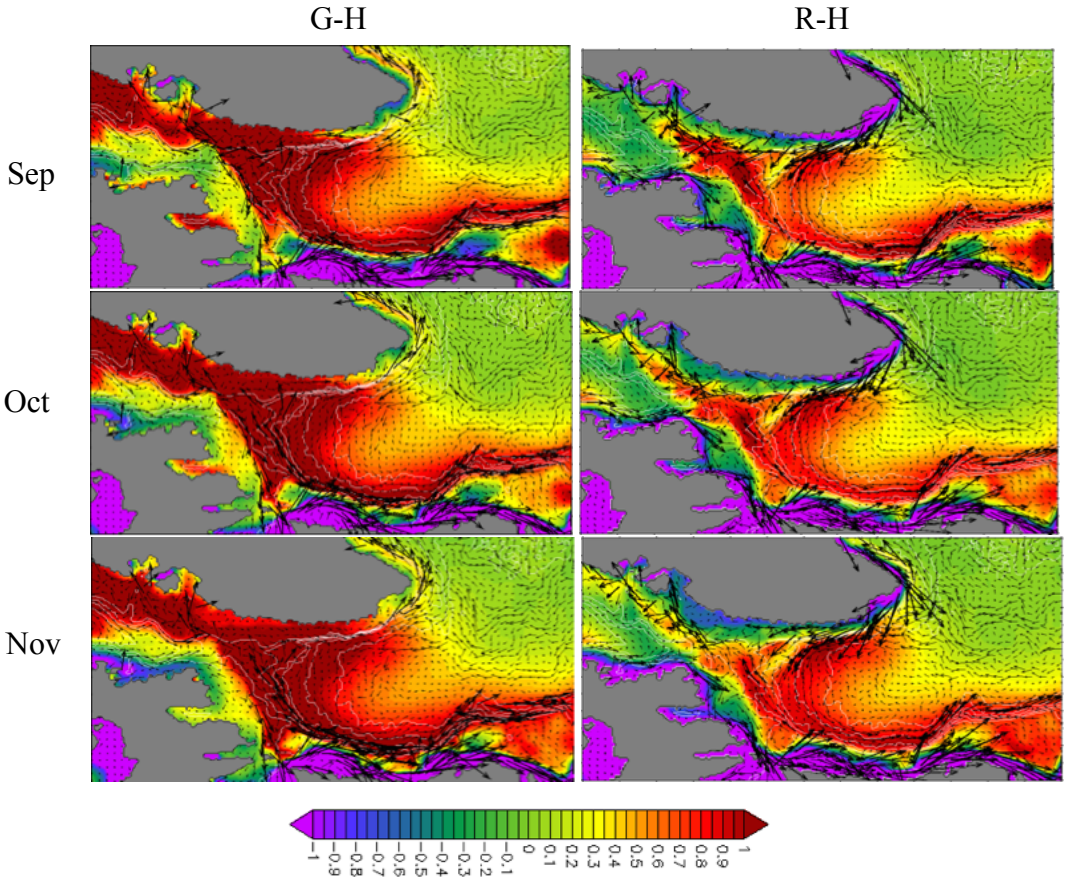


temperatures except along the westward recirculation path of the boundary current where the G-case exhibits its greatest temperature difference (~3ºC higher) from the H-case in late winter. The R-case also exhibits the warm surface temperatures along the cyclonic gyre but becomes 2ºC cooler than the H-case in the interior Labrador Sea during the summer. Unlike the G-case, the R-case shows a slight warming in the Baffin Bay and northern Labrador Sea when compared to the H-case. The shelf off of

Figure 17: (a) Surface temperatures for the June and December 1980-2009 mean and (b) difference plots between the G and H-case and the R and H-case means for the same months. Both the G and R-cases are warmer than the H-case in the westward recirculation flow. The R-case uniquely brings cooler temperatures along west Greenland during the summer. A slight remnant of this signature persists during December.

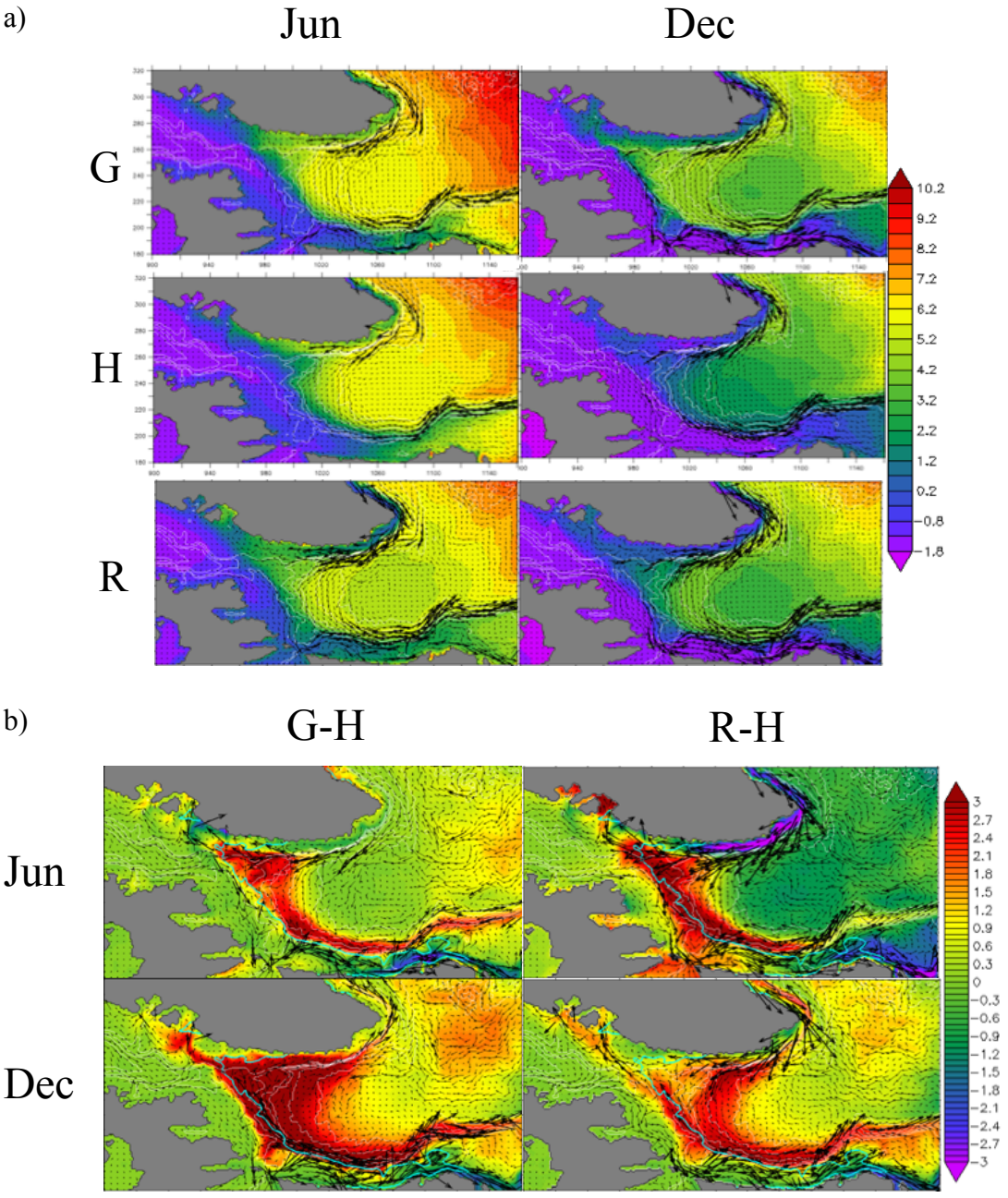

Labrador is cooler in the G and R-cases, especially in late summer. On the eastern side of the Labrador Sea, colder temperatures exist on the shelf only in the northern extent of our study region for the G-case. In the R-case, however, the same characteristic stretches along the entire west Greenland coast from June through August. In the fall through early winter, warm surface waters encroach the shelf of western Greenland in both the R and G-case.

Because the G and H-cases are identical runs except for the treatment of sea surface salinity and the freshwater forcing, any changes in surface ocean conditions can be attributed to ocean dynamics and not atmospheric forcing. Therefore, the saturation of fresh and cool water remaining on the shelf is due to local runoff (i.e. from the Greenland Ice Sheet) and advection of freshwater by the currents upstream (i.e. the East Greenland Current). The saline western boundary current in the G-case implies a lack of mixing between the shelf and interior or insufficient freshwater input along the west Greenland shelf, or both.

The differences in current velocities also reinforce the distribution of surface water properties mentioned above. For example, the warmer surface temperatures hugging the coast of Greenland in the G-case are exacerbated by a stronger H-case current which transports cooler temperatures during the late summer/early winter period only. This results in a greater difference in temperature between the two cases in later

periods. On the other hand, when the G-case produces stronger current speeds along west Greenland in the late winter through early summer, the surface temperature in both cases become more similar, since a greater transport of cooler waters compliments the transport in the H-case, leaving a smaller discrepancy between the two cases. Overall, the strength and longevity of the West Greenland Current in the G-case is greater than the H-case. It advects waters further north through Davis Strait, consistent with observations and not produced in the H-case. Similarly, the R-case has much stronger velocities than even the G-case along the tip of Greenland and northward following the shelf. Thus, the R-case is able to easily communicate water temperatures from east to west Greenland producing a cold water anomaly along the shelf. As the East Greenland Current receives freshwater from the Arctic during the summer melt, the cool temperatures compared to the H-case along the west Greenland shelf in the R-case are likely a result of this main export pathway.

Recirculation flow and the southward Labrador Current reaching Hamilton Bank is greatest in the R-case. The H-case is stronger than G-case throughout most of the year, especially October through January. The current width differs between the three cases. Most of the current path is situated on the continental slope in the H-case which is equal in strength to the R-case throughout part of the year. However, the overall stronger currents in the G and R-case stem from the flow along the shelf that greatly surpass the H-case, as is shown in Figure 16 and 17. The Baffin Island Current

is strongest in the R-case in the late fall, peaking in October. Again, this may be due to the strong freshwater forcing from meltwater exported from the Arctic through the Canadian Arctic Archipelago.

In summary, the representation of the mean annual cycle of surface temperatures, salinities, and velocities in the Labrador Sea by the G, H and R-cases show large differences on seasonal and spatial scales. The G and R-cases both produce warm and saline cyclonic gyre conditions compared to the H-case. The R-case is uniquely cooler in the interior during summer months and has salinity gradients that change from fresh to saline conditions in the offshore direction. This horizontal structure in the upper layers helps to create instabilities in the boundary current, which produces eddies and helps to mix the shelf and interior properties (Spall, 2004; Straneo, 2006; Rykova et al., 2015). The G-case produces realistic seasonal conditions in some areas, but the critical west Greenland shelf region does not produce a sufficient cold or fresh signal. The velocity of the G and H-cases are similar except during the late summer/ fall season where the H-case is usually stronger in producing the southward flowing Baffin Island and Labrador currents. The R-case has stronger current speed than both cases throughout the cyclonic gyre circulation and coastal currents.

### 2.1.2 Comparison of G, H, R-Case to PHC

Figure 18: Surface Salinity Relative to PHC. Here we plot the winter (DJF) and summer (JAS) mean monthly difference plots between the G,H, and R-cases and the PHC data set. As expected, the H-case maintains similar values to the data set it is being restored to. The G and R-cases behave similarly with larger salinities along the cyclonic gyre. The R-case maintains more fresh conditions along the shelf of west Greenland.

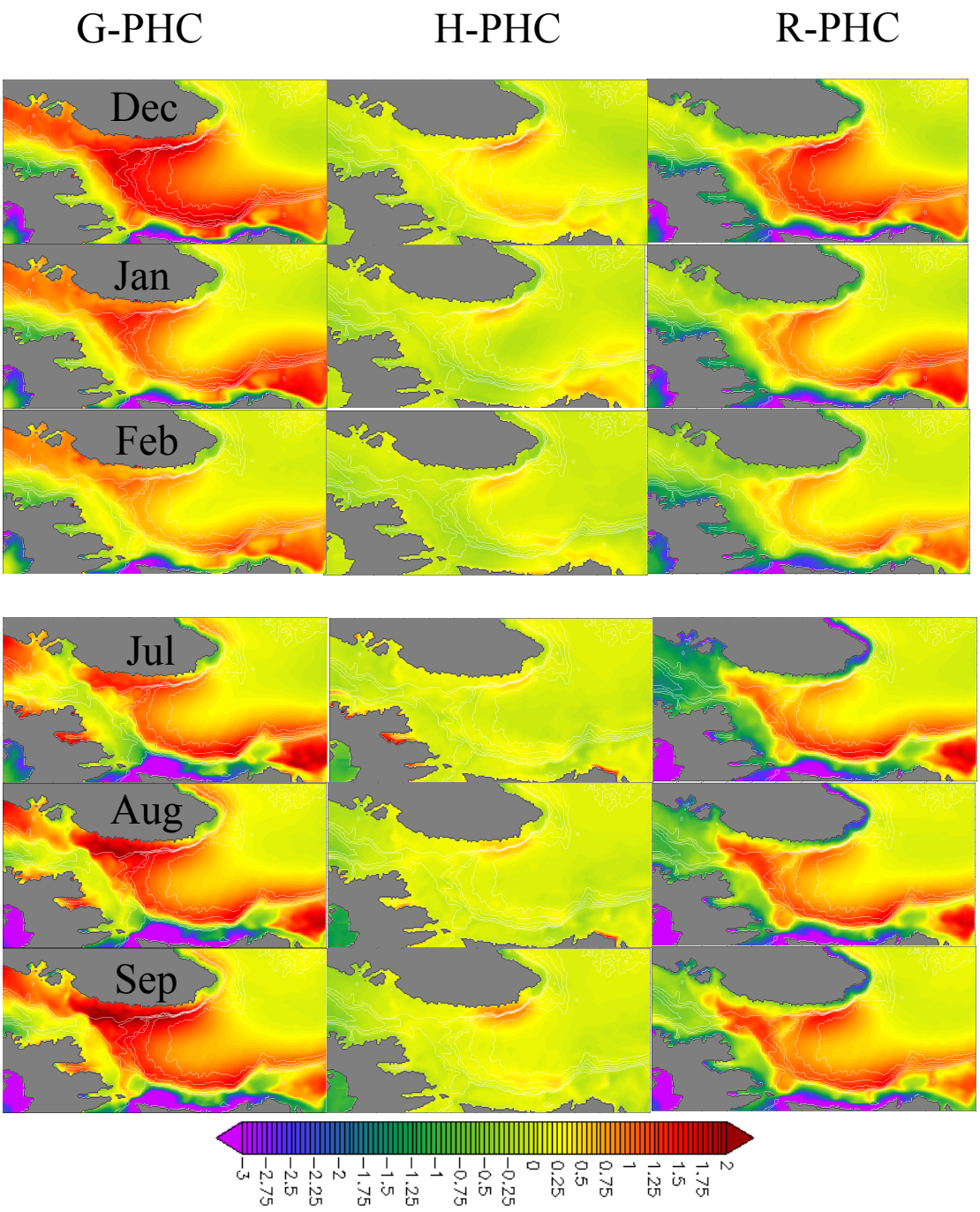

G, H, and R-case surface temperatures and salinities are compared to the PHC data set (Steele et al., 2001). As expected, the surface salinity in the H-case remains very close to PHC values except where the H-case exceeds values of PHC salinity near Cape Desolation. The SSS in the G and R-cases behave similar to each other, but the R-case has a smaller magnitude of difference that is more spatially limited compared to the G-case. Overall, both cases have a more saline westward recirculation flow than the PHC, with the strongest signal appearing in late fall through December. The R-case exhibits a freshwater signal along the coasts of Greenland and Labrador for the entire year, which it consistently shares with the G-case on the Labrador side only. This comparison is highlighted in Figure 18, where difference plots between the PHC and each model simulation are displayed for monthly mean plots of the winter and summer season. The major departure from the PHC in the two cases occurs in the Baffin Bay, however the G-case is more saline, and the R-case is more fresh there. All three cases show the greatest similarity to PHC in February and March.

Also, all three model cases follow similar patterns in surface temperatures compared to the PHC (Figure 19). The G and R-cases, which typically resemble each other in differences compared to the PHC, diverge in the summer months leaving the G and H-cases with similar conditions. The G and H-cases show large warm biases off the Labrador coast, especially near Hamilton Bank. Instead, the R-case continually transports cool Arctic origin waters southward into this region during the summer

Figure 19: Surface Temperature Relative to PHC: The difference plots in the monthly mean G, H, and R-cases relative to the PHC are shown for these two seasonal extreme months. All three models produce similar patterns of biases during February. During September, the R-case has the least bias in surface temperatures relative to PHC than the G and H-cases.

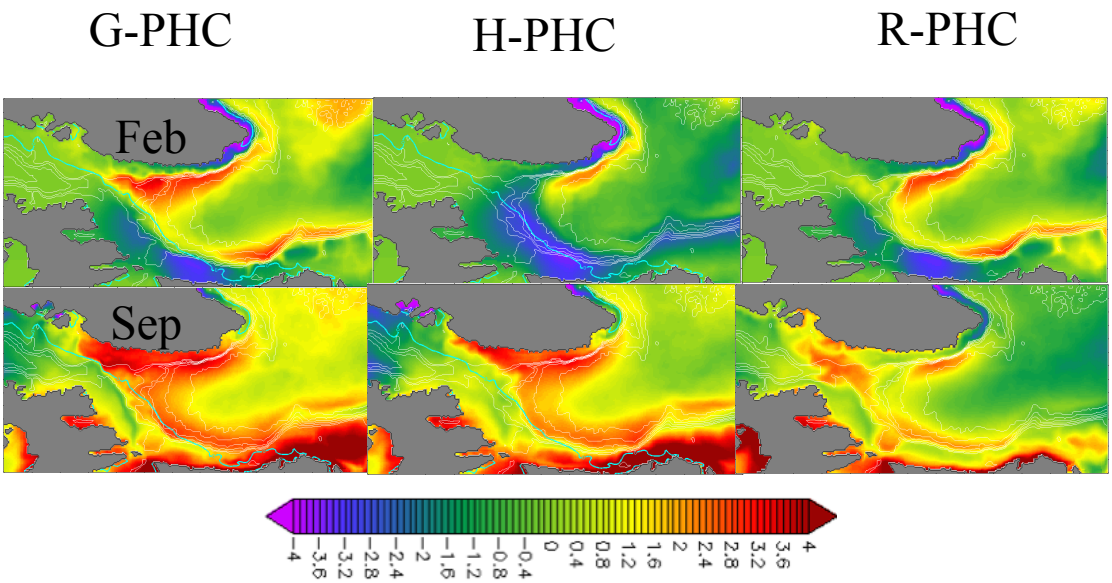


months, keeping the difference relative to the PHC at a minimum. These cooler temperatures exist on the eastern side of the Labrador Sea as well, where the G and H-cases lose this signal in the summer months. Because the G and H-cases are forced with the same atmospheric conditions (reanalysis), the same broad and large scale warm biases are seen in both the G and H-cases.

During the winter, all three cases produce cooler temperatures in the outermost extent of the basin that surrounds an inner ring of warmer temperatures compared to the PHC. This is indicative of the heavy summer-time sampling that the PHC is based on,

which creates a seasonal bias towards warm and fresh conditions (Steele et al., 2001). So the PHC is unable to capture the cool conditions along the shelf, whereas the models are unrestricted in their winter-time temperatures. The ring of warm model temperatures compared to the PHC during winter also has to do with the sampling bias, as the observations are skewed toward cooler interior-basin properties where they spend the most time (Steele et al., 2001). In the central Labrador Sea, the H-case shows more pronounced cooler temperatures compared to the PHC of all three cases. This may be due to its reduced boundary current flux compared to the other cases. The G-case produces a warm bias in the fall through winter that reaches farther north along the west Greenland coast than any other model. The R-case mimics this, with a reduced magnitude and extent of the warm bias. During the summer, the R-case also produces warmer SSTs in Disko Bay which is not seen in the other two models.

The G and R-cases behave similarly in the surface temperature and salinity fields. As expected, the H-case produces the most similar behavior to the PHC fields in salinity, but the G and R-cases also perform well in the temperature in the interior Labrador, where the observations are more reliable in producing seasonal change. Most significantly in terms of the Labrador Sea dynamics, the R-case most extreme shelf-to-interior gradients in temperature and salinity, likely reinforced by the strongest cyclonic circulation produced of all three cases. Unlike the G-case, the R-case is

unique in terms of its maintenance of fresh and cold surface waters in the coastal zones. This makes it the most prone to instabilities and eddy mixing.

## 2.2 Sea Ice Evaluation

The Labrador Sea harbors a marginal ice zone during the months preceding and following the sea ice maximum extent in March (Parkinson et al., 1999). This introduces additional (other than currents, eddies, and runoff forcing) variability to the near surface water properties (McGeehan & Maslowski, 2011). We compare our simulated (1980-2009) mean monthly sea ice extents with the mean monthly observational record during the same period in Figure 20. The modeled (black) and observed (blue) contours of 15% sea ice concentrations, defined as the fractional area of each grid cell covered by sea ice, are plotted over a shading of SSS for the mean annual cycle. The evolution of sea ice in the G-case is slightly more realistic during the winter growth season than in the H-case, which tends to overestimate the sea ice extent. Both cases do not capture the rapid spring-time retreat as observed. These discrepancies between observations and the model simulations may be caused by biases in the air-sea heat flux, ocean currents, or ice thickness. In addition, discrepancies in the annual sea ice advancement and retreat could be in part related to the fact that sea ice melting temperature in the CICE version 4 (used in the G and H-cases) is set to -1.8ºC, regardless of water salinity. Here, we examine the contribution of oceanic advection of heat to sea ice growth and decay.

Figure 20: Monthly mean maps of modeled (black) and observed (blue) contour lines of 15% sea ice concentration are plotted below over the mean SSS for 1980-2009.

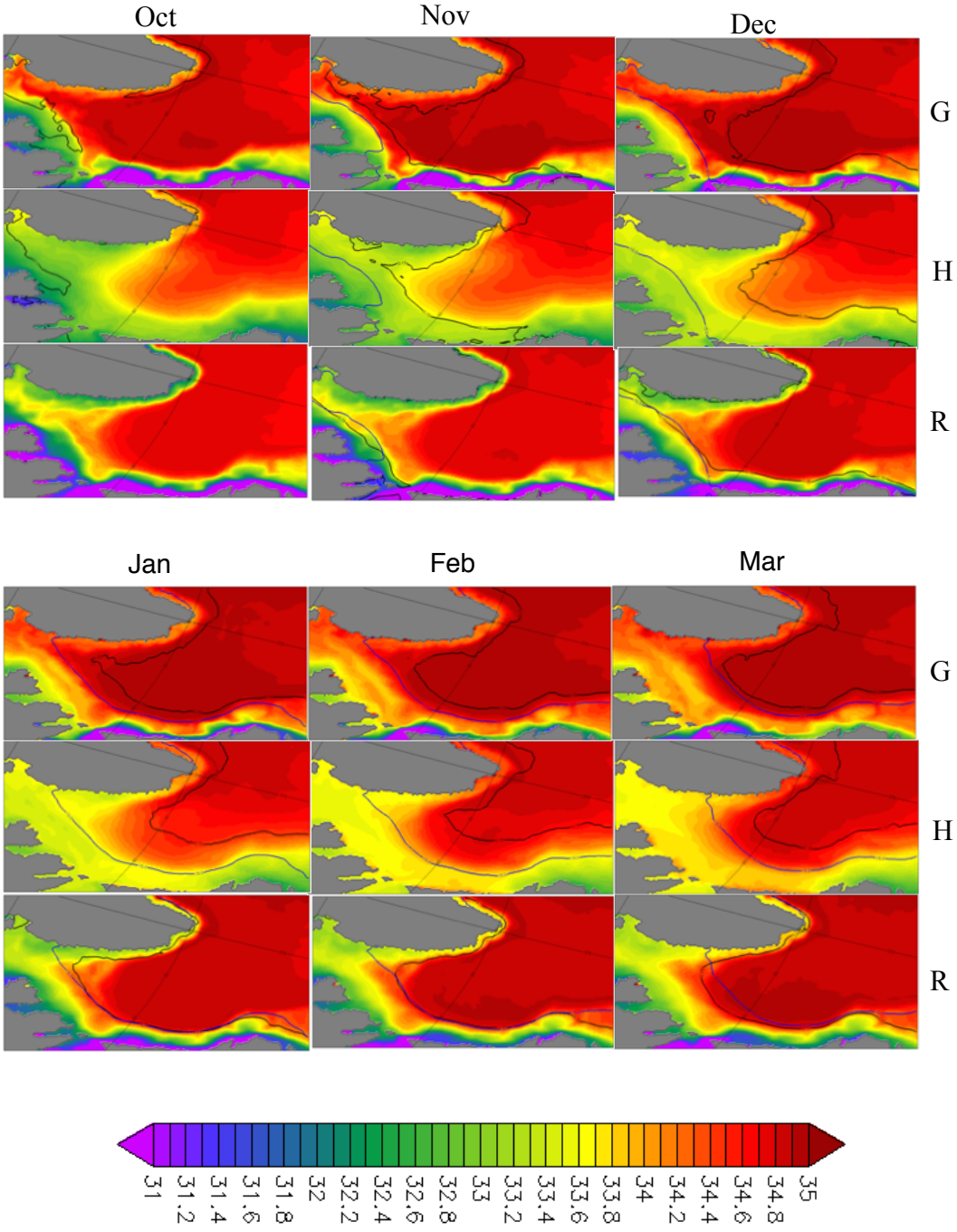

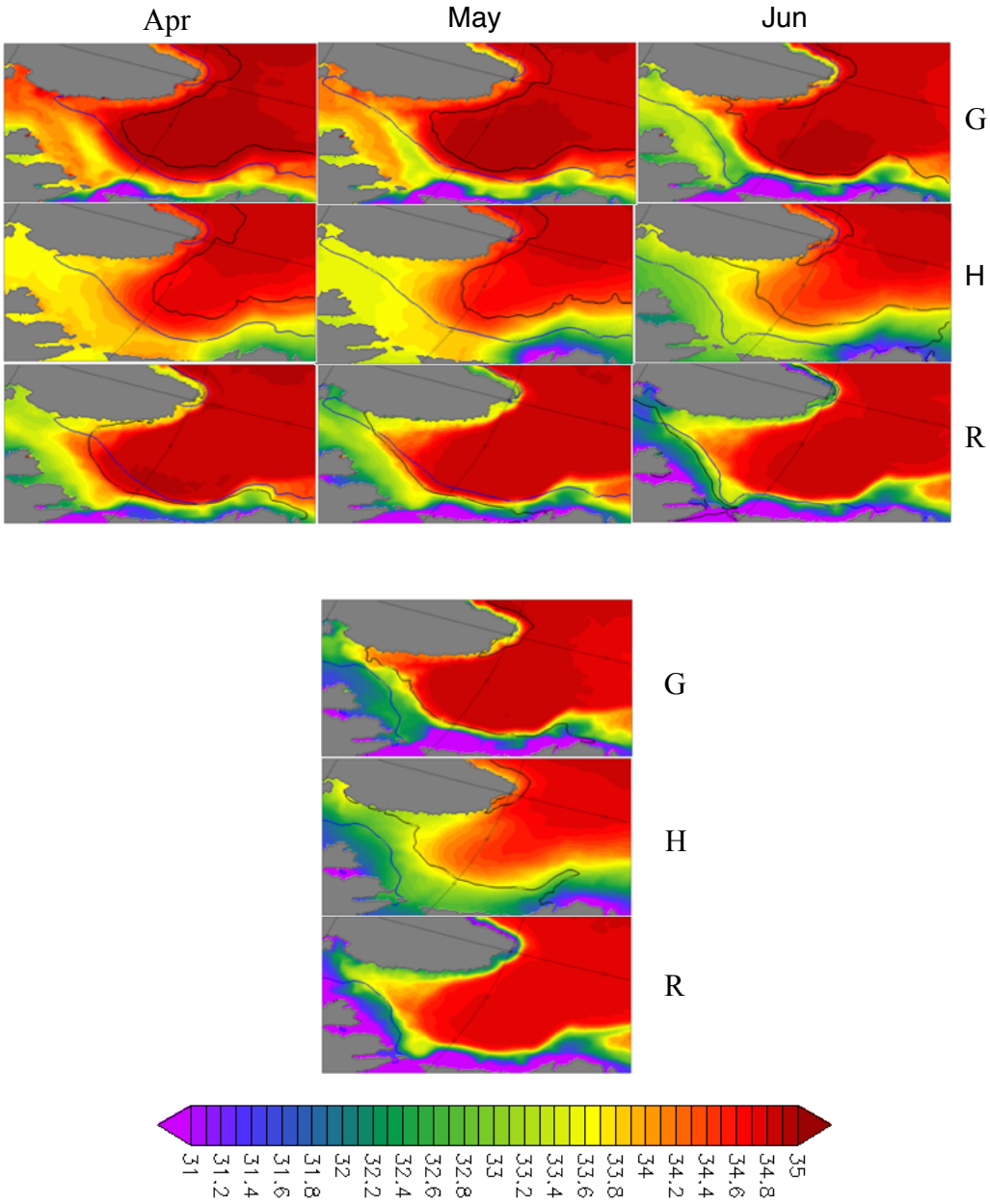


During the early winter season in the G-case, a warm surface water mass protrudes north along the west Greenland shelf which helps to prevent sea ice growth. The warm water penetrating north returns in the spring, but falls short of causing enough melt to match the sea ice decay rate since it does not create the observed ice-free

coastline near west Greenland. This warm water helps maintain an asymmetry in sea ice extent between east and west sides of the Labrador Sea, but in the G-case it is less

Figure 21: This is the mean annual net heat flux (TW) through the top 11 layers (~100m) MGE for each model and the all-time mean. Negative values indicate northward fluxes along Greenland's shelf. The G and R-cases produce a fairly equivalent time series, while the H-case has a much shorter season of northward heat transport.

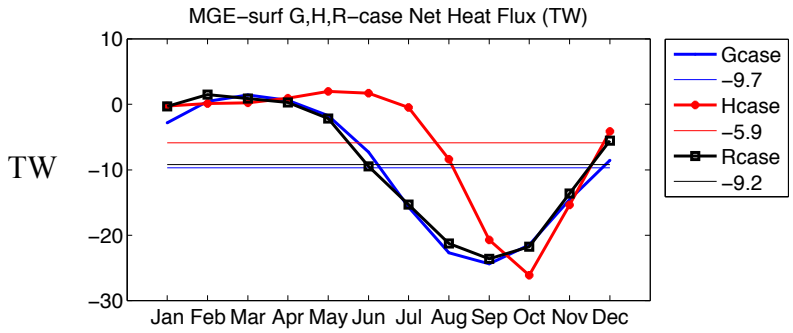


pronounced than the observational record. The mean annual cycle of surface (~100m) oceanic heat transport northward through the MGE transect line (location shown in Figure 4b) given by the plot in Figure 21, indicates that the G-case transports more heat than the H-case with the warm water arriving earlier in the year in the former case. Overall, the evolution of sea ice extent is more realistic in the G-case when the sea surface conditions are allowed to be dynamically influenced by buoyancy fluxes (runoff and E-P).

The mean annual cycle of sea ice extent is similar in the R-case to the G-case. In the growth season, both models overestimate the sea ice extent before matching observations in the northern and western sides of the basins in the peak of winter. They fall slightly short of observations in late winter, especially in the amount of encroachment by sea ice into the central Labrador Sea. The R-case and the G-case, produce too much ice on the west Greenland coast, especially in late winter. The R-case loses this ice faster than the G-case and is able to match observations here in the retreat season. By July, the R-case does not show any significant sea ice, but observations still show the presence of sea ice off the southern and western coasts of Baffin Island. The R-case alone reproduces the encroachment of sea ice from East Greenland around Cape Farewell better than the other two models. Overall, the R-case resembles the G-case in its pattern of too rapid sea ice growth and decay in the shoulder months before and after winter (JFM).

The R and G-cases produce almost identical magnitudes and timing of surface heat flux through the MGE transect line (location shown in Figure 4b). This can be responsible for the improved skill shown in these models in the reduced sea ice growth and enhanced retreat along the Labrador Sea Greenland coast as compared to the H-case. Additional variations in the sea ice cover in the R-case may be due to its use of CICE version 5, which accounts for salinity-dependence of the freezing/ melting temperature of sea ice.

Figure 22: Total kinetic energy of the top 120 meters for the all-time mean in the G,H, and R-cases. The R-case has the greatest rim current presence, as well as coastal buoyancy currents while having the most quiescent interior.

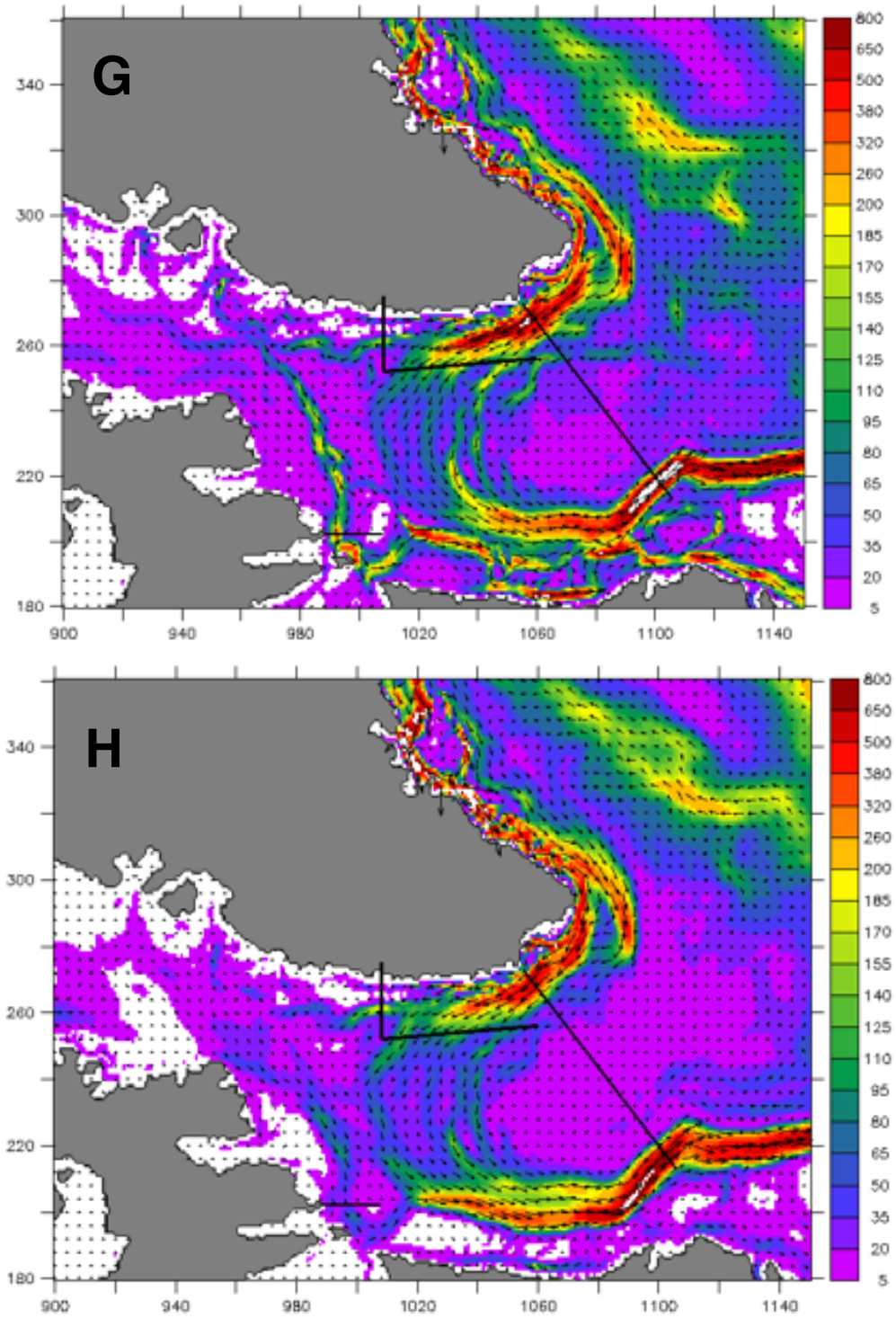

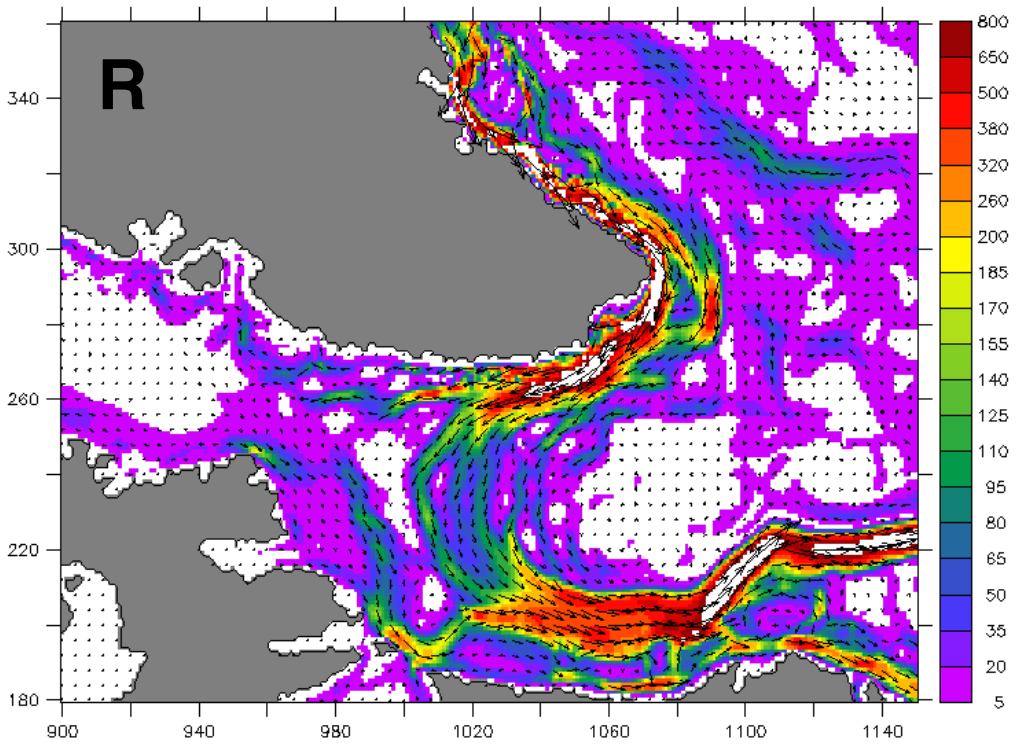


## 2.3 Current Structures

The distributions of surface currents in the three simulations are depicted in Figure 22 together with the 1980-2009 time-mean total kinetic energy (TKE), defined as: $TKE=^1/_2(u^2+v^2)$ over the top ~120 meters. The G-case exhibits the most energetic coastal buoyancy currents over the continental shelves of Baffin Island, Labrador and Greenland. However, the total flux of the R-case rim currents exceed that of the other two cases because heightened current speed extends further and is wider than in the G and H-cases. These currents are more pronounced on the Labrador side, reaching TKE values of 800 $cm^2/s^2$ in the G-case. The R-case almost matches the G-case here but has magnitudes that are slightly below the G-case. The coastal buoyancy currents

Figure 23: The cross section of salinity and velocity for the mean January, May and September Labrador Current transect. Contours of velocity begin at 5 cm/s and increment in 5 cm/s. These months were chosen to display seasonal variations. The R-case has the largest coastal buoyancy current development throughout the year, with velocities surpassing 25cm/s in the winter.

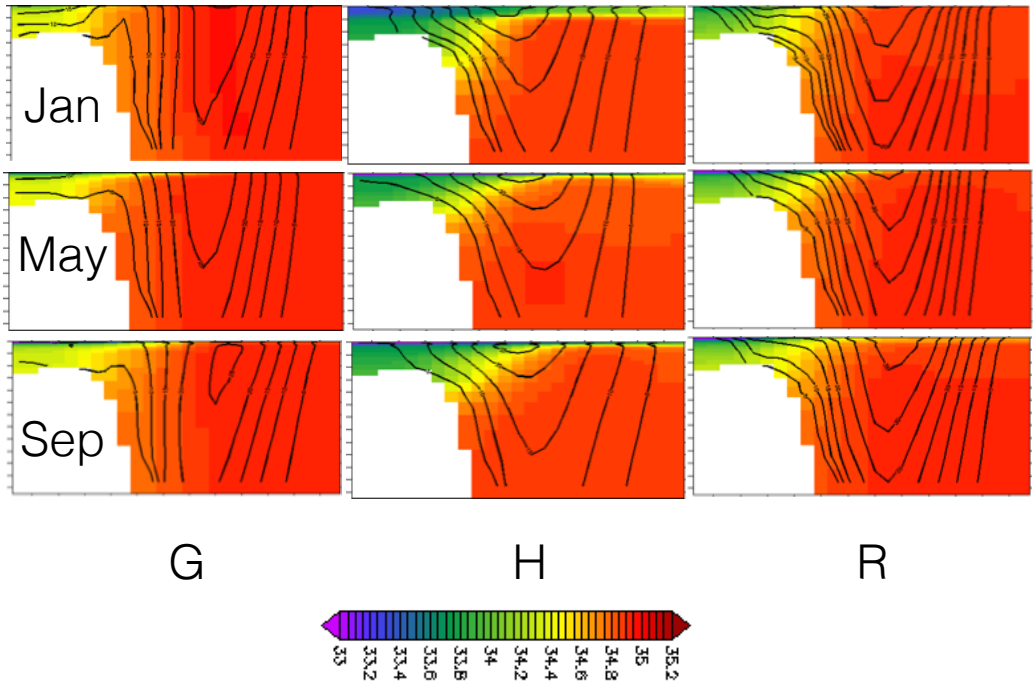


in the H-case in this region show slightly elevated levels, reaching a maximum current of 150 $cm^2/s^2$. This is illustrated in the TKE maps (Figure 22) and in the salinity-velocity cross sections of Figure 23, where the coastal buoyancy currents along the Labrador shelf are most pronounced only in the G and R-cases. The location of the transect line across the Labrador Current is shown in Figure 4b. On the eastern side of the basin, there is also an elevated coastal flow in the G and R-cases. In the R-case, it has a higher magnitude and reaches further north than the G-case, with traces

of it reaching north of Disco Bay. The H-case does not support a coastal current along west Greenland.

The coastal buoyancy currents are distinct from the main cyclonic gyre circulation that follows the continental slopes on either side of the basin. There is a sharp westward veering of the boundary current system from the eastern Labrador Sea to the western side. These pathways follow the 1000-3000m isobaths and their flow conserves basin-scale potential vorticity. These isobaths also bound the Labrador Sea basin to its north. The maps of TKE in Figure 22 show four distinct current paths diverging from the eastern side of the basin in the G and R-cases. In the H-case, there are only three such pathways. The emanation points of the recirculation paths along the continental slopes of Greenland are contained in the northern end of the 'bathymetry gap' and coincides with a maxima of eddy kinetic energy (McGeehan & Maslowski, 2012; Bracco et al., 2008; Brandt et al., 2004). One branch of the WGCS continues to flow northward along the 500m isobath. This is captured by the G and R-cases only, where the northward flow reaches Davis Strait throughout the year. In the H-case, some months exhibit an unrealistic southward flow along this current path, even as far south as the MGE transect line (location shown in Figure 4b).

On the southward flowing leg of the boundary current system along the Labrador coast, the R-case produces the widest swath of dynamic flow. It peaks in the same

Figure 24: The mean annual cycles of volume and freshwater through the surface layers of the Cape Farewell transect line, restricted to the shelf region only. The R-case surpasses both the G and H-cases in volume and freshwater flux. The H and R-case have a more defined seasonal cycle than the G-case.

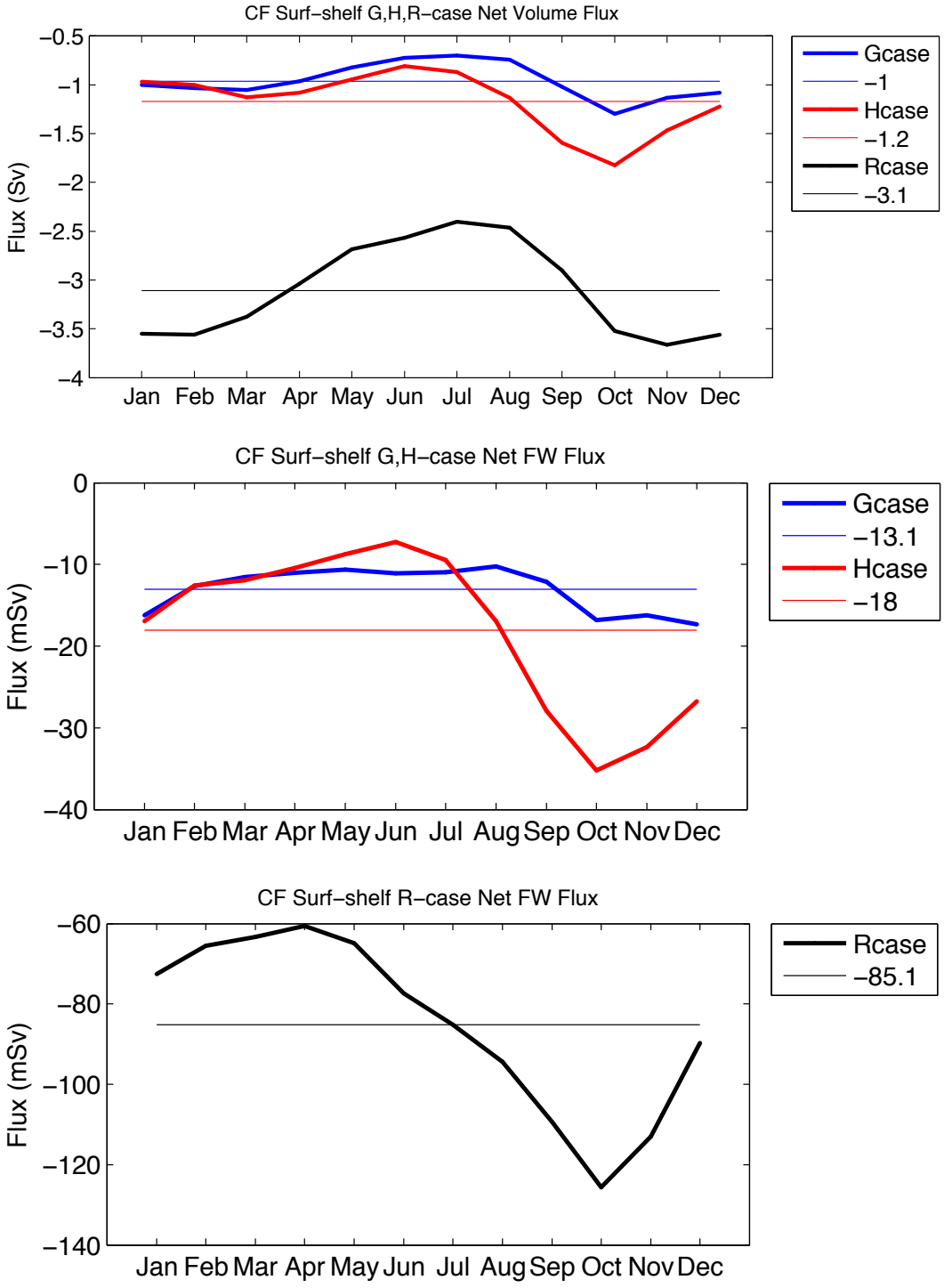

region as the G and H- cases, seaward of Hamilton Bank. The G-case has the most defined current structure, with one current hugging the 500m isobath along the northern boundary of the Labrador Sea and remaining separate until Hamilton Bank when the flow is diverted along the edge of the coast. The G-case produces more defined and narrow currents along the 500m isobath emanating from Davis Strait compared to the H and R-cases. The final difference between the all-time mean surface kinetic energy plots is that the R-case has the most quiescent interior compared to the G and H-cases.

The annual seasonal cycle of the surface currents in the Labrador Sea, as indicated by TKE, differ between all three cases. From late summer through mid-winter (August-January), the representation of the East Greenland Current as it wraps around Cape Farewell and enters the Labrador Sea is slightly more dynamic in the H-case than the G-case. The mean annual cycle of the net volume flux through the surface layer of Cape Farewell (CF) restricted to the shelf (0-578m) is shown in Figure 24 (location of transect line is in Figure 4b). The H-case shows slightly greater flux throughout the year passing through the CF transect than the G-case, but the R-case surpasses their volume transport by a factor of 3 (~3Sv vs. ~1Sv). From the net surface freshwater flux through the CF transect (Figure 24), we find that the H-case flow carries ~50% more freshwater (referenced to salinity of 34.8) during the peak advection month in October than the transport within the G-case. In the R-case, this coastal current

Figure 25: The volume and freshwater flux through the MGE transect line. The R-case exhibits most realistic flow with consistent and powerful northward flow, but the H-case shows a net southward flux.

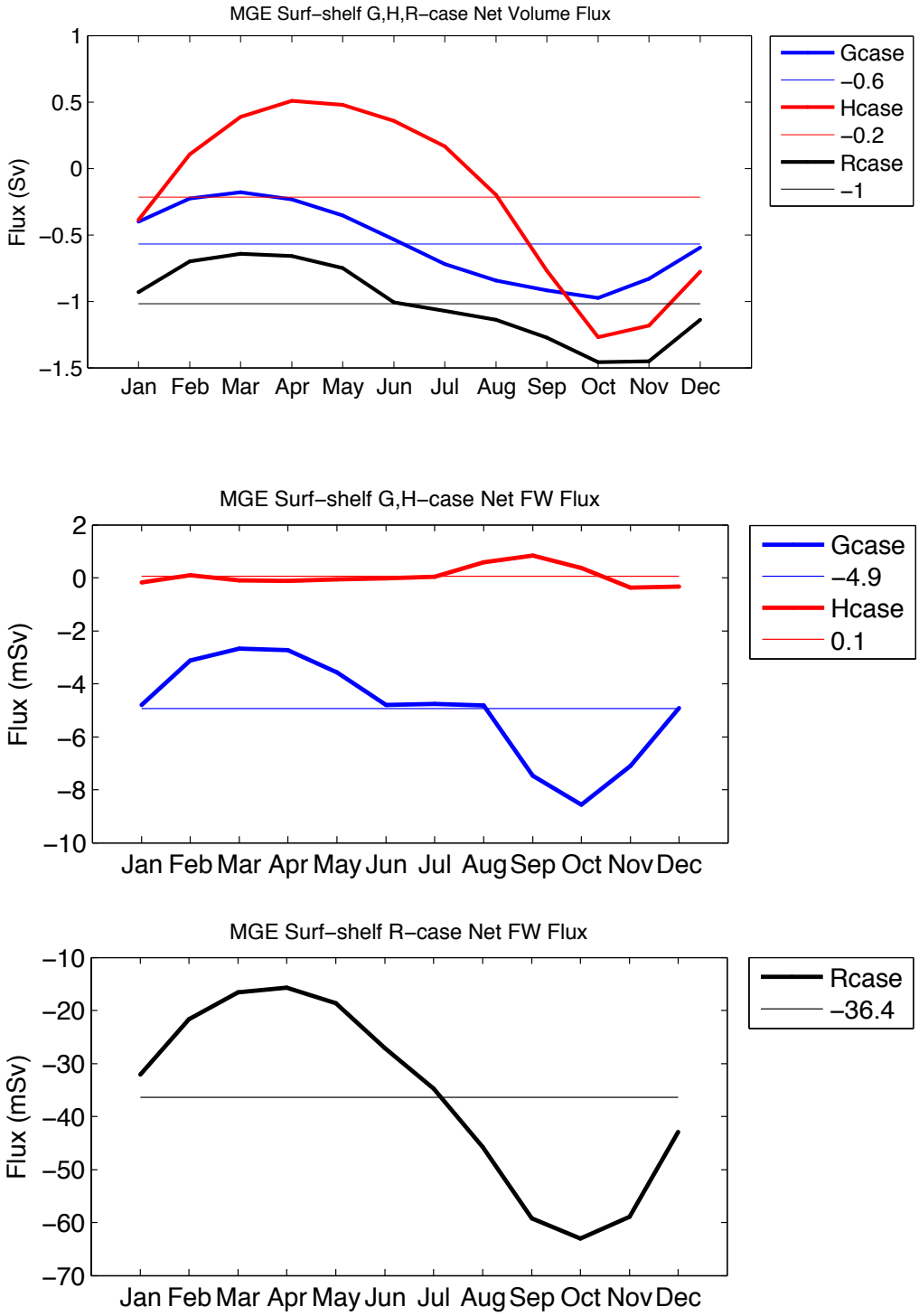

transports 6 times the volume of freshwater (85 mSv) than the G-case (13mSv) on average. The timing of the peak in freshwater transport at Cape Farewell suggests that it is linked to the seasonal summer freshwater pulse due to melting sea ice, glacial runoff and other upstream freshwater sources of the East Greenland Current (Sutherland & Pickart, 2008). As it wraps around the southern tip of Greenland with its surface component of Arctic-origin fresh water, the shelf-interior salinity gradient of the West Greenland Current is also enhanced.

Beginning at Cape Desolation and continuing northward amid the bathymetry gap region, the G-case has a stronger current than the H-case throughout most of the year, and the R-case surpasses them both. This is shown in the mean annual cycle plot of Figure 25 of the volume transport in the surface layers through MGE, which marks the northern extent of the 'bathymetry gap' (location shown in Figure 4b). The G and R-cases have northward flow throughout the year (indicated by negative values in Figure 25), including during winter, whereas the H-case has an unrealistic southward flow (positive values) during winter time. The R-case maintains strongest northward flow throughout the year with a mean flux of 1Sv. Recent observations from the Greenland side of the AR7W line (within 100km) of the WGCS determine a climatological mean transport of 1.8+-0.15 Sv (Rykova et al., 2015). In SON, the G and R-cases display a peak season for freshwater flux through the surface layer of MGE, reaching values of ~36 mSv in the R-case and ~5 mSv in the G-case

Figure 26: The mean January, May and September vertical cross sections of the MGE transect lines for all three model simulations. The color scale denotes salinity, the contours denote velocity with solid lines indicating in the northward direction through MGE. The vertical scale is in meters. The velocity contours begin at 5 cm/s and increment by 5 cm/s. The R-case has a sharp shelf-to-interior salinity gradient as well as the greatest magnitude of surface current speeds. The H-case current reduces throughout winter and is prone to a negative (southward flowing) current in May.

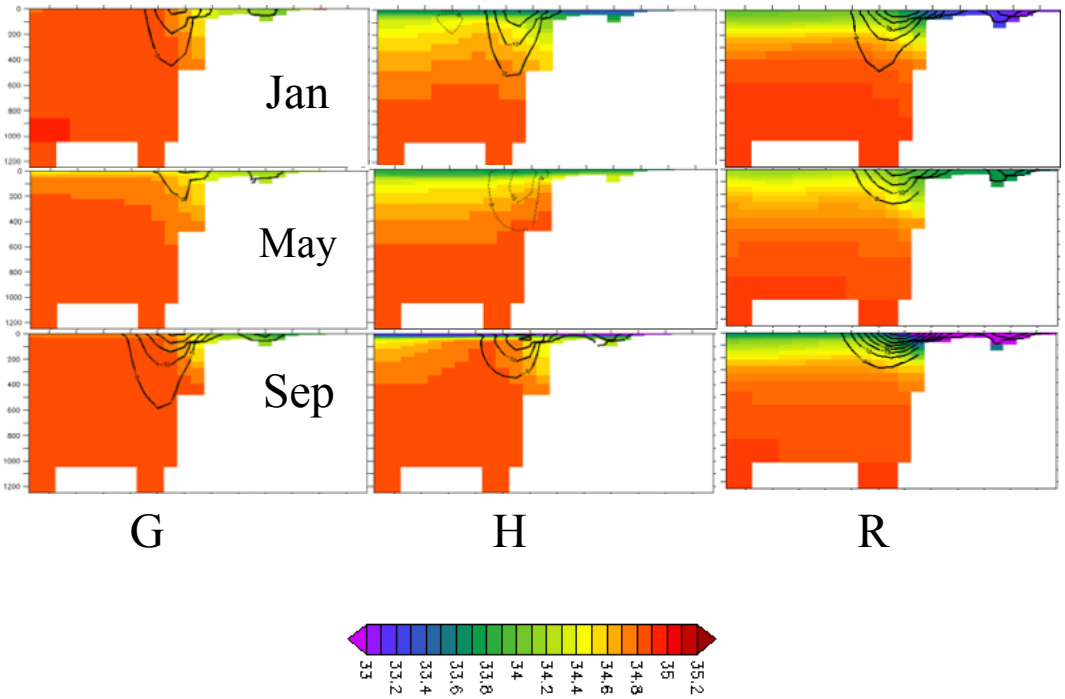


(referenced to salinity of 34.8). The G-case also mimics this realistic seasonal signal, though at a much smaller scale. The SON maximum in surface flow in all three cases has the correct timing for a fall maximum in transport observed along the WGCS (Rykova et al., 2015; Straneo, 2006).

The vertical distribution of freshwater along the transect line provides further information about the distribution of the flow. The mean January, May and September

cross sections of salinity and velocity along the MGE transect line are shown in Figure 26. The R-case is the only model simulation to produce two well developed currents throughout the year - the boundary current along the continental slope and the coastal buoyancy flow along the shelf. More discussion on whether this flow is a true coastal current is given in section 4.2. The magnitude of the main boundary current flow matches observations of ~35 cm/s from Cuny et al. (2002), whereas the G-case produces slower currents, and H-case has a fully reversed flow around May. The shelf-basin gradient in salinity is most distinct in the R-case where no doubt the strong coastal buoyancy flow reinforces the fresh conditions.

The total westward recirculation paths linking the eastern rim currents of the Labrador Sea to the southward flowing western currents are evaluated through the MGM transect line located in Figure 4b. All three cases have the strongest surface flux in the winter (JFM), though the R-case transports 0.5-0.6 Sv (or 17-21%) more than the H and G-cases, respectively, in March. The mean volume flux in the surface layer hovers around 2.5Sv for both the G and H-cases, and increases to ~3.2Sv for the R-case. The maximum surface freshwater flux (referenced to salinity of 34.8) along the recirculation paths is produced in the H-case during the late fall, early winter period. This is due to the relatively fresh surface conditions that the H-case is restored to, as seen in the previous plots (such as Figures 16 and 18) examining the surface salinity difference between the models and the PHC.

Figure 27: The mean annual cycle of the net volume flux for the G, H and R-cases through the Labrador Current at the location shown in Figure 4b (labeled 'LabCur').

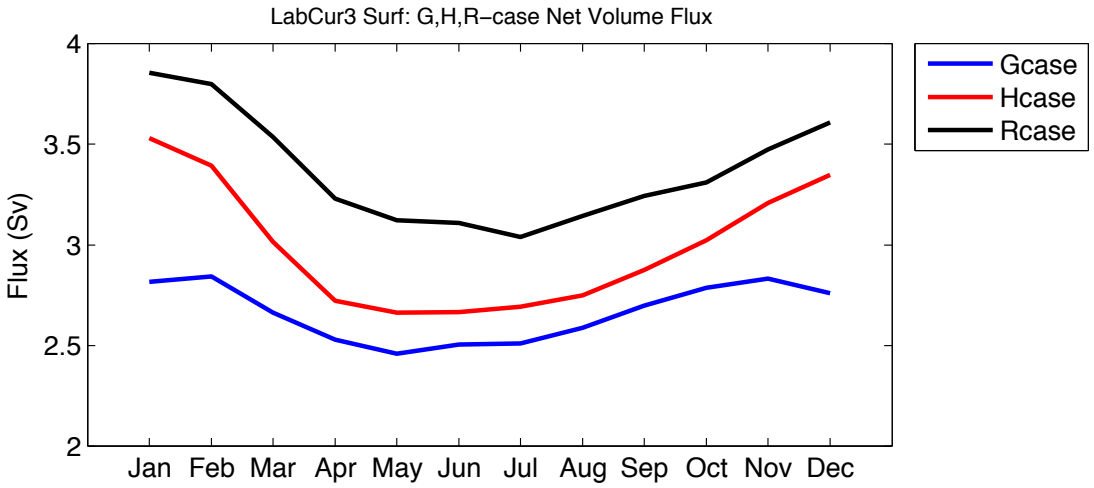


The southward transport through the Labrador Sea begins with the Baffin Island Current flowing through Davis Strait before merging with the Labrador Current, as shown in the TKE plots of Figure 22. The Labrador Current exhibits a limited seasonal variation in flow, with the G-case continuously producing a strong coastal buoyancy current along Labrador and a constant current following the 500m isobath from the Davis Strait. This is shown in the vertical transect plot of Figure 23. Accordingly, we produce the mean annual cycle of net surface volume flux through the Labrador Current transect line (location labeled 'LabCur' in Figure 4b) in Figure 27 to assess the slight seasonal variation. There is an increase in southward flow from Davis Strait during June through January in the H and R-cases. The G-case produces

a similar but shortened signal where the enhanced flow from the north occurs from July through November. We attribute the enhanced flow during this season to the decaying sea ice extent and the runoff maximum during the summer in the Baffin Bay and Canadian Archipelago. This results in a delayed downstream increased freshwater flux in the central Labrador Sea during the summer through late fall season.

# Chapter 3: Evaluation of Mixed Layer Depth

## 3.1 Background

The oceanic and atmospheric conditions of the Labrador Sea allow for deep convection to take place. One of the main objectives of this study is to further diagnose the controlling influences from freshwater on the quantity of LSW production. Freshwater can disrupt or inhibit deep convection by entering the Labrador Sea basin primarily through eddy mixing. The vertical extent of deep convection can be used as a measure of the quantity of LSW production and is also measured by the mixed layer depth (MLD). The MLD is generally considered a zone in the surface layer of the ocean where ocean tracers, such as temperature and salinity, are homogenous, but in deep convection regions of the open ocean, the MLD extends to intermediate and deep layers of the ocean. Thus, in our study, we seek to measure MLD in the model experiments as a way to represent the impact of freshwater in the central Labrador Sea in terms of the production of LSW, which impacts global climate through the AMOC.

In practice, a MLD is difficult to determine. A given MLD is associated with a particular time scale since the process of mixing and overturning is a continuous part of ocean dynamics (Montegut et al., 2004). For example, MLDs associated with the diurnal cycle will be more shallow than a multi-day or monthly MLD that has taken

into account repeated cycles of mixing by converting available potential energy into turbulent kinetic energy. Ideally, below this vertically homogenous surface zone, the density profile will abruptly change in the vertical direction to form the pycnocline. However, there may be multiple fossil layers, or weak pycnoclines, in the upper water column, but the MLD may still be defined below these at the top of a main pycnocline that reflects strong stratification (Kara et al., 2003). In addition, both models and observations have limited resolution of seawater properties which further obscures the ability to discern an exact MLD.

The vertical variability in the water column properties makes a single definition of MLD difficult, and thus there is no agreed upon way to compute the mixed layer depth from measured profiles or ocean model outputs (Luo et al., 2014). The most common method, a threshold method, defines the MLD as the depth at which an offset in surface temperature or density occurs (Monterey & Levitus, 1997; Lorbacher et al., 2006). The gradient method uses a critical gradient threshold to define the MLD, though it has been brandished as less stable than the regular threshold method (Brainerd & Gregg, 1995). Some techniques employ curve-fitting methods, where at least two line segments are fitted to the profile and their intersection point determines the MLD (Thomson & Fine, 2003). Finally, integral methods have been used as well as the development of customized methods (Freeland et al., 1997; Lorbacher et al., 2006). The integral method calculates the depth at which the integral of the entire

potential density curve is equal to the area of a rectangle determined by the difference in surface and bottom potential densities and an arbitrary depth (Thomson & Fine, 2003).

Within the threshold method, a plethora of critical values are used throughout the literature. Temperature is used as the controlling variable to determine MLD in most global studies, however it is acknowledged that density should be used in high latitude studies where salinity strongly impacts the density structure (Montegut et al., 2004). Some studies following Monterey and Levitus (1997) use a critical value of 0.125 $kg/m^3$ from surface potential density to determine a longer-term MLD such as multi-day or climatological studies (Montegut et al., 2004). Diurnal MLD assessments conventionally use a much smaller value of 0.01 $kg/m^3$ (Thomson & Fine, 2009). Moreover, the threshold method uses one standard critical value even though every density profile depends on the local dynamics and buoyancy forcings. A spread of critical values used in the literature range two orders of magnitude, from 0.005 $kg/m^3$ to 0.5 $kg/m^3$, for a variety of MLD timescales, as shown in Table 1 in Kara et al. (2003).

On the fundamental level, MLD depends heavily on the ability for mixing or turbulence to develop, but most of these methods, especially the threshold method, neglects taking into account the curvature of the density profile. In fact, MLD can be

defined as the depth at which the stabilizing effect of buoyancy matches the destabilizing effect of mixing and where turbulent vertical mixing would stop. The MLD method developed by Large et al. (1997) computes a MLD within the vertical mixing parameterization in the ocean model, called K-Profile Parameterization (KPP) (Large et al., 1994). In this method, the buoyancy gradient from the surface value to a depth at every vertical layer is calculated. Then, the maximum value in this large-scale, global density profile gradient is matched to an equivalent value of a local density gradient (computed between adjacent levels on an interpolated profile). The depth at which the gradients are equivalent is the MLD. This is computed at every grid cell so that the unique curvature of each density profile is taken into account.

## 3.2 Methods of Current Study

In our study, a variety of methods have been used to calculate the mixed layer depth (MLD) from the ocean model output. These methods were applied to both monthly mean and daily-averaged potential density profiles (though the latter was used in the R-case only) in order to determine a robust method that accurately portrays the evolving MLD. The first method, commonly used in modeling studies of deep convection in the Labrador Sea, uses a threshold value, or critical value, of potential density change from the surface value. We refer to this method as the CV method. We used threshold values between 0.001 kg/m$^3$ and 0.005 kg/m$^3$ in the monthly-mean profiles and between 0.025 and 0.005 kg/m$^3$ in the daily-averaged output to determine

Figure 28: The monthly mean winter MLDs (m) from 1980-2009 for all three simulations. In addition to the CV and MDG methods below, the POP method results are also displayed for only the R-case.

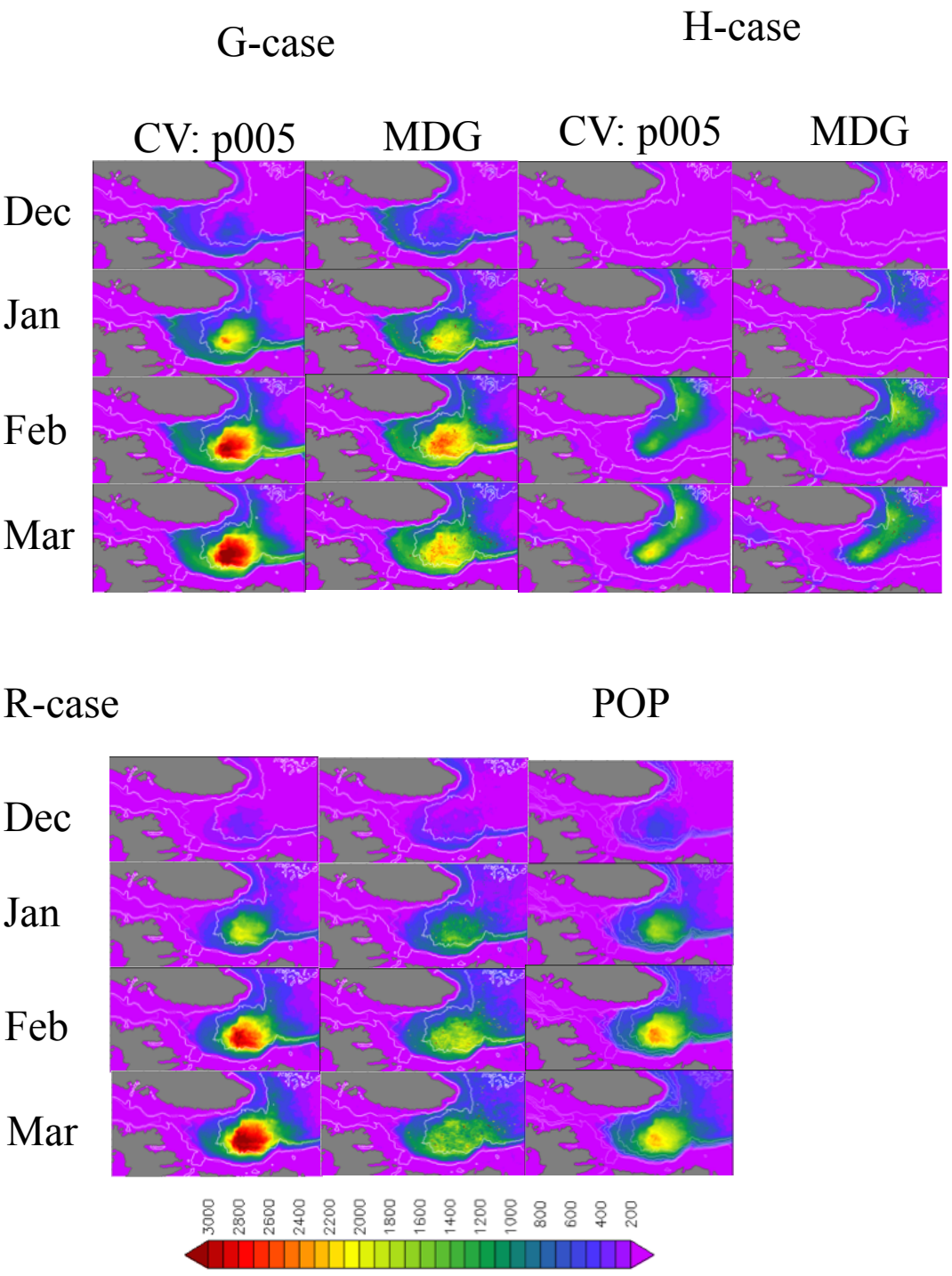

the value that best represents the MLD. Ultimately, we chose critical values of 0.005 and 0.02 kg/m$^3$ as the best representations of the monthly and daily MLD evaluation, respectively. The smaller threshold value of 0.005kg/m$^3$ proved too sensitive for daily fluctuations of temperature and salinity, yielding large swaths of near-surface MLD estimations that appeared on a high frequency basis. The second MLD method defines its value as the maximum (positive) gradient in potential density, and is referred to as MDG in the following text. The final method is calculated in the source code of POP in the KPP vertical mixing scheme, is explained above and by Large et al. (1997), and will be labeled as POP in subsequent analyses. The R-case is the only simulation with POP MLD output. Results of these methods are shown in Figure 28 for the 1980-2009 monthly means during the winter.

Across all methods, the G-case exhibits the strongest deep convection signature in the entire interior basin of the Labrador Sea, as shown in the winter-time monthly mean plots of the entire model simulation (1980-2009). The G-case begins this vigorous cycle in December as the central and southwest Labrador Sea reach a mixed layer depth greater than 3000m by February, though observations suggest that such extreme MLDs should only occur at the end of winter (Clarke & Gascard, 1983). There is resistance toward developing deep MLDs in the north and northeast Labrador Sea, as can be seen in the relatively shallow MLD in that region compared to the western side of the basin. This is due to the influence of the boundary current system and eddy

production, particularly Irminger Rings, that help maintain a local buoyancy source for the water column (Pickart et al., 2002; Lilly et al., 2003). However, along the northern most edge of the Labrador basin along the 1000m isobath, deep MLDs (more than 1000m) emerge late in the winter during the mean annual cycle.

The H-case has the most limited spatial extent of a deep convection signal in the Labrador Sea out of all the simulations. The main deep convection signal appears in February, much later than all other cases. It shares its deepest MLD location in the southwestern Labrador Sea with the G and R-cases, which is consistent with the position of the observed deep water formation sites in the region (Pickart et al., 2002; Lilly et al., 2003). The H-case, however, is the only simulation that creates a diffuse region of a deep water formation site south of Greenland. This has been identified as a possible deep convection site (Lavender et al., 2002) but further study of this region is needed to elucidate its role as a major North Atlantic deep water formation site (Vage et al., 2011). In addition, the H-case shows no sign of deep convection in the south-central basin until February and March, when the average MLDs for these months reach more than 1200m. This indicates a vigorous winter-time convection process seen in all simulations, where large MLD values develop rapidly.

The R-case behaves similarly to the G-case in magnitude and spatial distribution, however it produces marked improvements. First, the onset of the deepening MLDs is

delayed by approximately one month and begins in January in the mean annual cycle. This is closer to the behavior seen in the H-case, and in better agreement with observations that record deepest MLDs in March (Lavender et al., 2002; Lilly et al., 2003). Second, the R-case has a more confined distribution of deep MLDs. The north/ northeast region of the Labrador Sea shows reduced MLDs compared to the western side, and this area shows an even more curtailed signature of deep convection compared to the G-case. Even the deepest MLDs in the southwestern Labrador Sea are confined to a smaller region, reflecting its more realistic deep water formation signal.

Deep convection occurs intermittently and at a highly localized horizontal resolution (200-1000m) (Lilly et al., 1999; Lavender et al., 2002). There is strong interannual variability in the strength of deep convection associated with NAO phases, so that any regular strong deep MLDs implies a vigorous convection signal that may be too strong to be supported by observations (Lilly et al., 1999; Pickart et al., 2002). This strong convection signal is seen in all three model results. The vigorous nature of the convection signal in particularly the G-case is due to the low freshwater forcing the ocean receives, allowing its stratification to be weak. Thus, the atmospheric forcing can quickly and regularly destabilize the density structure. The H and R-cases, on the other hand, receive local freshwater sources all year around. This helps to maintain a

layer of stratification to buffer the ocean from the intense atmospheric forcing, which the G-case struggles to produce.

On the other hand, the H-case allows for vigorous convection south of Cape Farewell, Greenland, despite its regular restoring to the PHC SSS climatology. This covers a more widespread region of deep convection than produced in the G and R-cases. The spatial pattern of the PHC SSS (Figure 9) provides some insight into why this occurs. The most saline surface properties exist south of Greenland and spread into the central Labrador basin throughout the year. This shows that wherever the SSS restoring value is greater than ~34.5, the water column structure allows deep MLDs to exist. The high salinity values are more conducive for deep water formation as they can more easily mix downward. The G and R-case surface salinities, however, are the result of model dynamics and where distinct subsurface water masses are brought to this region. This could create a water structure that is more stratified than in the H-case, which could have a smoothly varying subsurface salinity due to the constant surface forcing of saline water.

In summary, the MLD in the G, H and R-cases tends to be too deep and vigorous, especially if this variable is to represent deep water formation of the Labrador Sea. However, the R-case improves upon the other simulations by limiting the extent and depth of the MLD cycle. The resistance for deep MLDs to occur in the north/

northeast Labrador Sea in the G and R-cases indicates the realistic interaction of the boundary currents with the density structure of the water column. The H-case MLD pattern tracks the advance of high salinity surface restoring into the central basin and produces a diffuse area of deep convection.

### 3.2.1 MLD Assessment

Each MLD method shows similar characteristics across all model simulations in the monthly mean plots for the winters of 1980-2009 (Figure 28). First, the CV method produces the deepest MLDs of all methods. In the G and R-cases, this means near-bottom MLDs are reached, whereas in the H-case, there is a concentrated region in the south-central Labrador Sea with 2000m MLDs for the mean February and March. The MDG method produces the lowest MLD values in general, and for the R-case,

Figure 29: The bathymetry map (m) of the Labrador Sea study region with the 6 individual points where vertical profiles are evaluated. Also labeled are the three transect lines, MGE, MGM and AR7W Line, where vertical cross sections of model properties are analyzed.

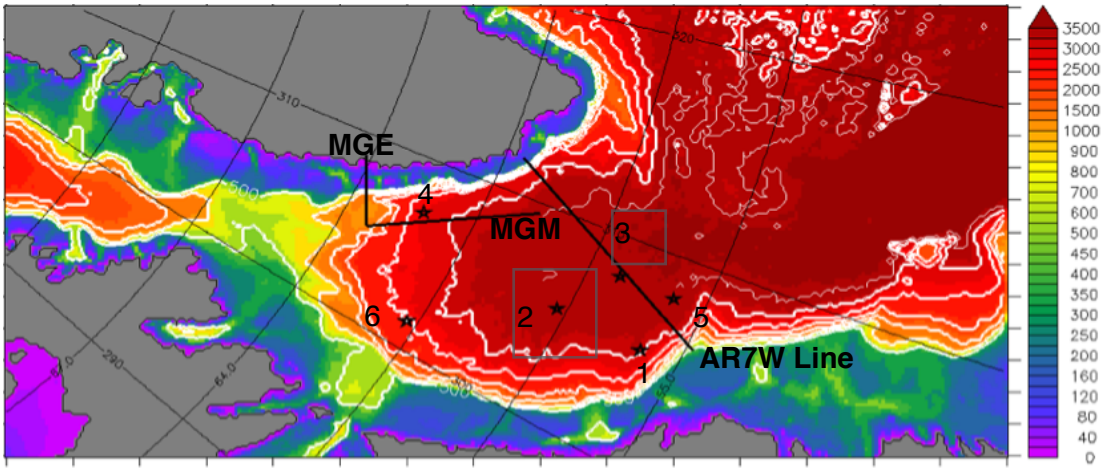

the MDG method reaches 1500-2000m depth, which is a more realistic range than the CV method (Lavender et al., 2002; Yashayaev & Loder 2009). Finally, POP begins to produce large MLDs early in the season, unlike the other methods for the R-case. Its maximum depth in February-March, although not as high as the CV method, still surpasses ~2400m.

Table 1: The all-time mean winter R-case MLD (m) determined by each explored method for each of the 6 points labeled in Figure 29.

| | Pt1 | Pt2 | Pt3 | Pt4 | Pt5 | Pt6 |
|---|---|---|---|---|---|---|
| MDG | 1935 | 1639 | 1438 | 554 | 1368 | 916 |
| POP | 1362 | 2091 | 1638 | 470 | 1138 | 736 |
| CVI-P005 | 1784 | 2696 | 2151 | 362 | 1598 | 750 |

To further evaluate the strengths and weaknesses of the different MLD estimates, we investigate MLD values on six vertical profiles of potential density in the R-case. Using the equation of state for seawater by McDougall et al. (2003), we calculate potential density everywhere in the domain based on the monthly mean potential temperature and salinity profiles. We specifically analyze the MLDs during three winters, 1983,1986, and 1991, where the map-views of the MLDs show extreme spread in results between the three methods. The six locations are indicated in the map of Figure 29, and the MLD maps for these years are shown in Figure 30. In Figure 31 we display the vertical profiles for the winter season (January, February, and March) for points 2 and 3. These points show the greatest dispersion in MLD values between each of the MLD methods throughout the entire simulation. In

Figure 30: Below are the maps of the R-case February MLD (m) for each of the three methods during 1983,1986, and 1991. These years exemplify greatest differences between the MLD estimates.

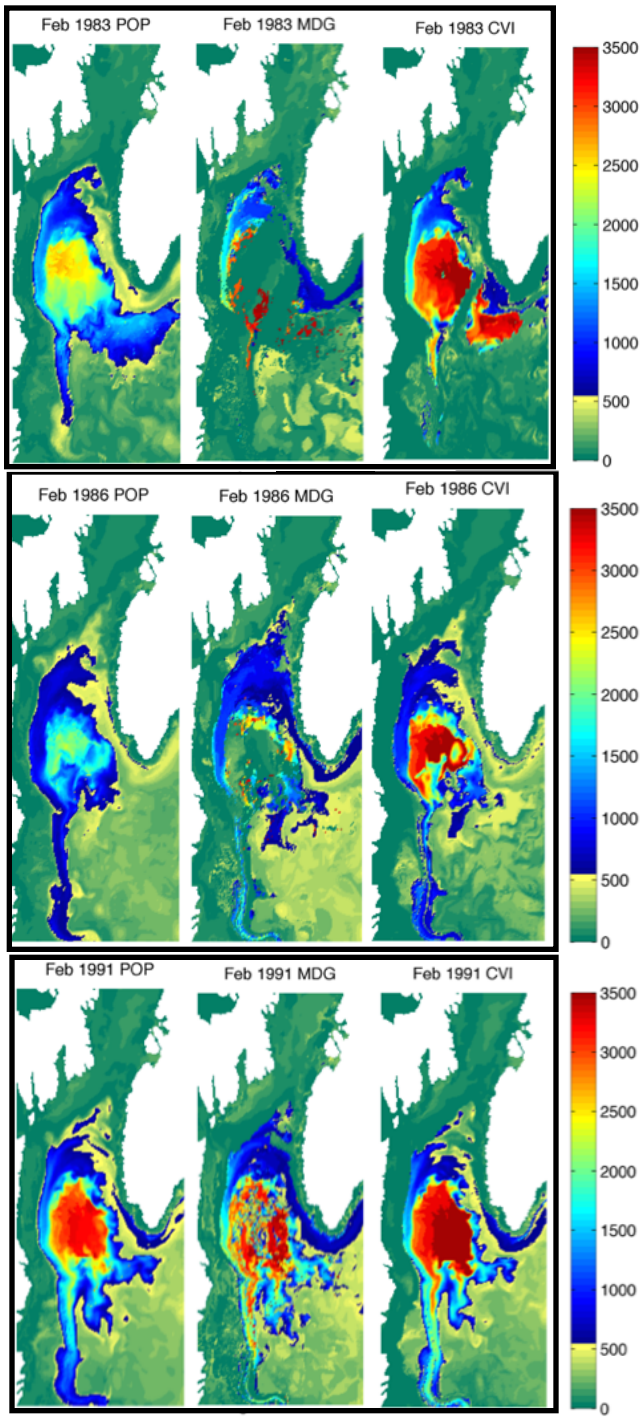

Figure 31: Here we display the vertical density profiles at points 2 and 3 in the R-case and the MLD based on several threshold methods, the MDG method, and the POP method during 1983, 1986 and 1991. These points represent places where on average there is the greatest discrepancy in MLD between the methods.

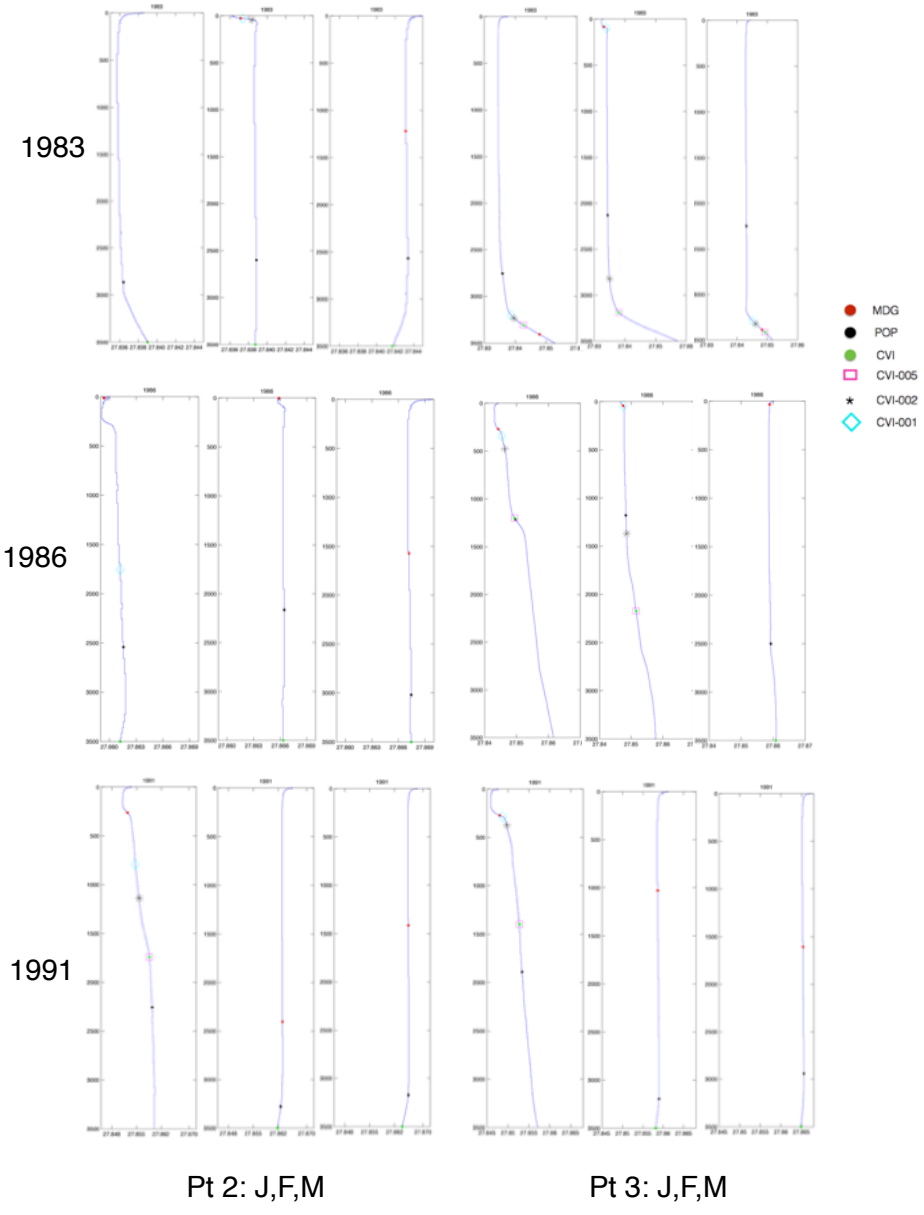

Figure 32: Vertical potential density profiles and MLD for all the methods for points 4 and 6 during the winter months for 1991,1986, and 1983 - the years that the spatial distribution of MLD in the Labrador Sea showed significant dispersion between the MLD methods.

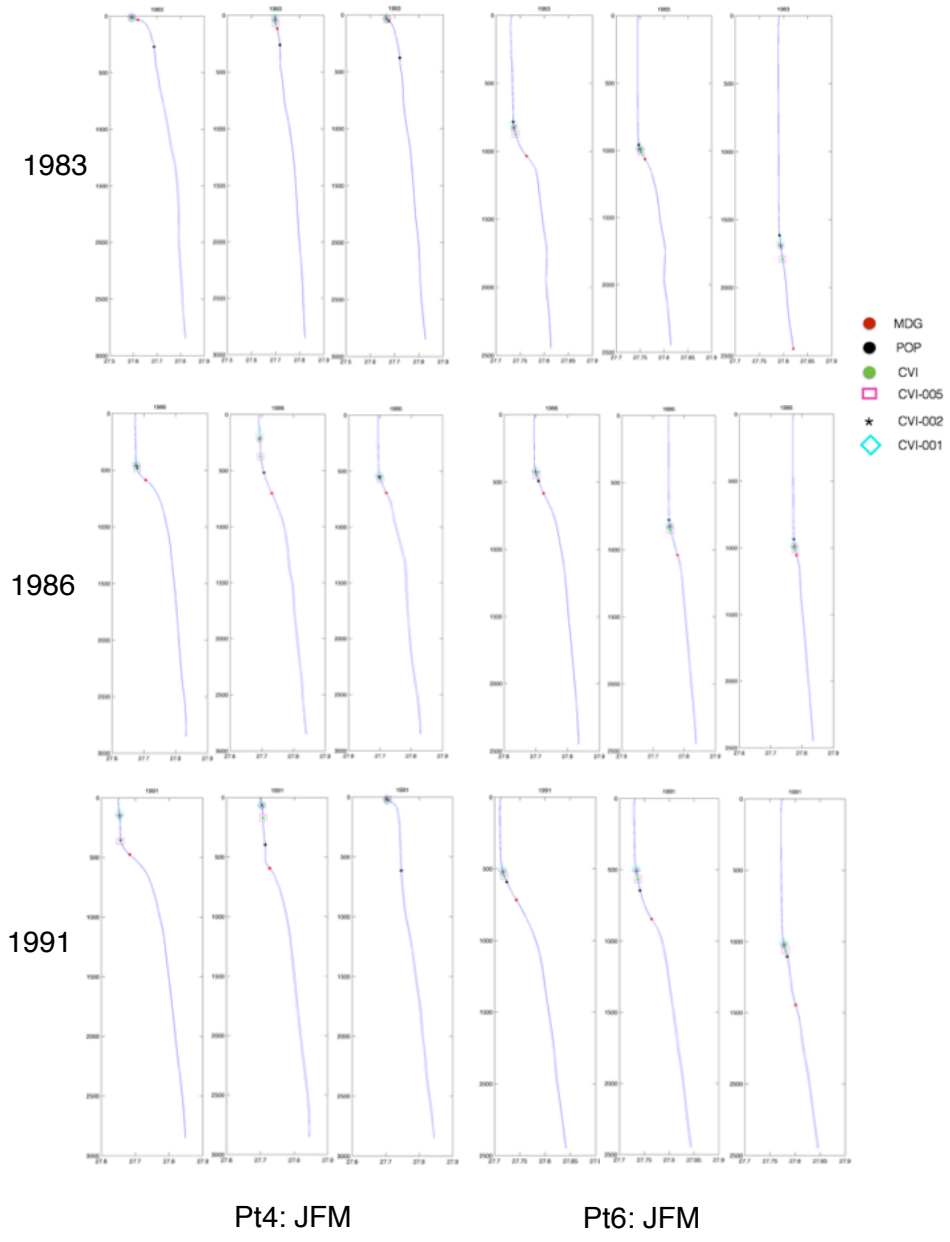

comparison, we also show profiles of points 4 and 6 in Figure 32, where MLD estimates by the different methods are more in agreement. The MLD values for each method are indicated on the profiles by the solid circles and labeled by the legends in Figures 31 and 32. The diamond, asterisk, and square markers indicate the MLD for critical values of 0.001, 0.002 and 0.005 kg/m$^3$, respectively. These markers also follow a different algorithm where no MLD is found if the critical value is not reached. The dispersion in mean winter-time MLD for the six points is given in Table 1. Points 4 and 6 agree between the three MLD methods to within 200 meters of each other whereas points 2 and 3 have a 700-1000 meter spread between the methods.

Of the 6 points visually inspected, those that show greatest differences between the methods and those that have more uniform results tend to derive from distinct potential density profile curvatures. For instance, profiles for points 2 and 3 undergo very small changes from the surface to bottom - on the order of 0.01 kg/m$^3$ or less. In addition, these monthly mean profiles commonly show a surface layer that is denser than the underlying waters due to continual surface buoyancy loss. In contrast, the other class of profiles that produce more uniform MLDs between the methods exhibit larger vertical changes in potential density - on the order 0.3 kg/m$^3$ or greater. These profiles also have a more standard curvature of a two-layer structure with constant density regions separated by a highly stratified pycnocline. The robustness of a MLD method is affected by these two classes of potential density profiles.

Figure 33: Left: The mean winter-time (JFM) MLD (m) for the MDG method highlighting the anomalously deep MLD in the central basin. Right: A detailed view of the MLD of the box in the regional image on the right. Here, isolated one-dimensional deep cavities exist where high density water builds up but is not able to mix or advect out.

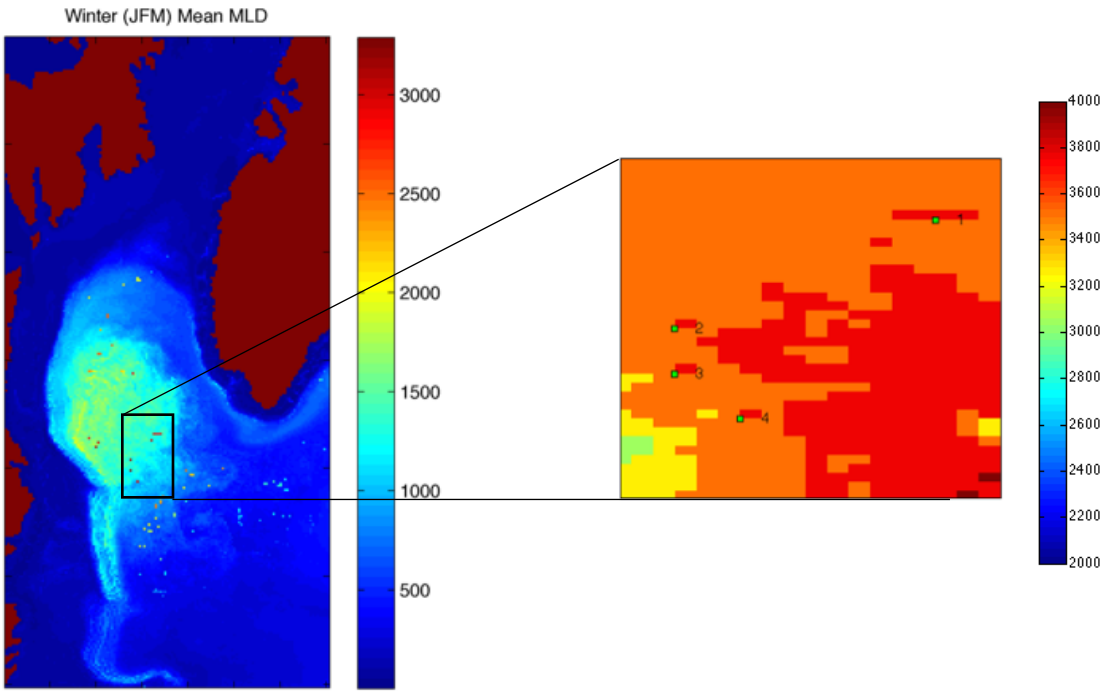


Across all profile types, the MDG method often exhibits deeper MLD estimates than what seems visually appropriate. Typically, the MDG method will locate the MLD in the middle of the pycnocline, rather than at the base of the MLD or at the top of the pycnocline. This is exemplified in Figure 32 with points 4 and 6, where pycnoclines are present. In Figure 31, the slight departures from uniform density throughout the water column leaves an absent pycnocline in most profiles, and the MDG method may locate a MLD in the middle of an essentially homogenous layer. Also, the MDG

method may pick out a MLD in the middle of the top layer or bottom layer where the most significant density change occurs in these irregular types of profiles. The MLD in the surface layer underlies the MDG method's tendency to be sensitive to surface buoyancy fluxes, since any addition of buoyancy will create a sharp stratification that the MDG is sensitive to in all profile types. This analysis is for the years where the MLD methods greatly diverge. On average, the MDG method produces MLDs that are less than the other two methods.

Another feature of the MDG method is that certain points produce anomalously deep MLDs with respect to the point's surrounding region at all times. This is shown in Figure 33, where these points are clearly visible in the winter-time mean MLD map. This seems unphysical, and upon further investigation we have determined the cause for such MLD estimates. They are co-located with points where the bathymetry opens up into a deeper single grid cell or single row (or column along the model coordinate system) of deeper grid cells. Due to the model numerical formulation, horizontal divergence of velocity is restricted in the numerics at these locations. So, dense water builds up in these cavities because they are unable to mix, advect or otherwise freshen their salinity signature. The salinity at these cavity grid cells can only increase due to vertical mixing, and thus the tendency of a sharp gradient exists between it and the cells above it. These anomalously deep MLD can be explained by the unsmooth bathymetry, and thus they do not lessen the accuracy of the MDG method.

The MLD determined by POP and evaluated at the 6 points are produced by averaging the daily POP MLD and plotting them on the monthly mean potential density profiles, shown in Figures 31 and 32. Thus the monthly mean MLDs may not correspond with the visually realistic result in the figures. Compared to the other MLD methods, the POP MLD tends to be much more shallow in the irregular profiles. With the more standard two-layer profiles, the POP method may overestimate the MLD compared to the other methods, but these MLD assessments are still within a reasonable range. Moreover, the POP MLDs tend to be deeper than the CV method but more shallow than the MDG method.

The CV method also shows a variety of strengths and weaknesses as exemplified in the four points shown in Figures 31 and 32. In the standard profiles (points 4 and 6), the MLDs are intuitively positioned, though they may be too shallow where a profile undergoes a uniform slope or a large swing in the surface buoyancy. In the irregular profiles of Figure 31, the CV method has a tendency to locate MLDs that are the entire depth of the water column or close to it. This is because in these profiles, the water column is essentially homogenous.

Sometimes, the density profiles do not span a range that exceeds the threshold value, meaning that the vertical density change in the water column is less than 0.005kg/m3.

In the original CV method, the algorithm assumes the full water column depth as the MLD if the threshold value is not reached, even though observations of deep convection never include full water column overturning and maximum MLD observed in the Labrador Sea reach 2000m (Lavender et al., 2002; Pickart et al., 2002). An additional algorithm is constructed to allow a MLD to not be defined if the threshold value is not reached. The results of this latter option is given by the maroon squares in Figures 31 and 32. However, this method is not preferred because a significant percentage of the MLDs become undefined. Of the 6 points that we evaluate, point 2 is undefined 49% of the time during the winter months of 1980-2009. Since one of the main objectives of this study is to analyze the effects of eddy production and freshwater transport on deep convection in the Labrador Sea, a consistent and definite measure of MLD is necessary. Another argument used against this algorithm producing undefined MLDs is that the threshold value implies that any density variation less than the critical value is a mixed layer. So including the entire water column as a mixed layer is consistent with the underlying assumptions of the threshold method. Thus, we choose to keep the original CV method results in subsequent analyses. The unrealistic fully convected water column may be a result of the model capabilities, with its low, 250m, vertical resolution in the 1050-3750m depth range and its reliance on sub-grid scale parameterizations, not the CV method itself.

A final independent criterion was used to determine the optimal MLD method, i.e. being physically realistic in time and across all regions of the study area. Since convection is highly sensitive to the surface buoyancy flux, we calculate the Pearson's correlation (Correlation Coefficient, n.d.) between each component of the surface buoyancy flux and the MLD determined by all three methods for the winter-

Figure 34: The mean winter-time correlation coefficients between MLD and SFWF (top row) and between MLD and SHF (bottom row) for each of the three MLD methods for the R-case.

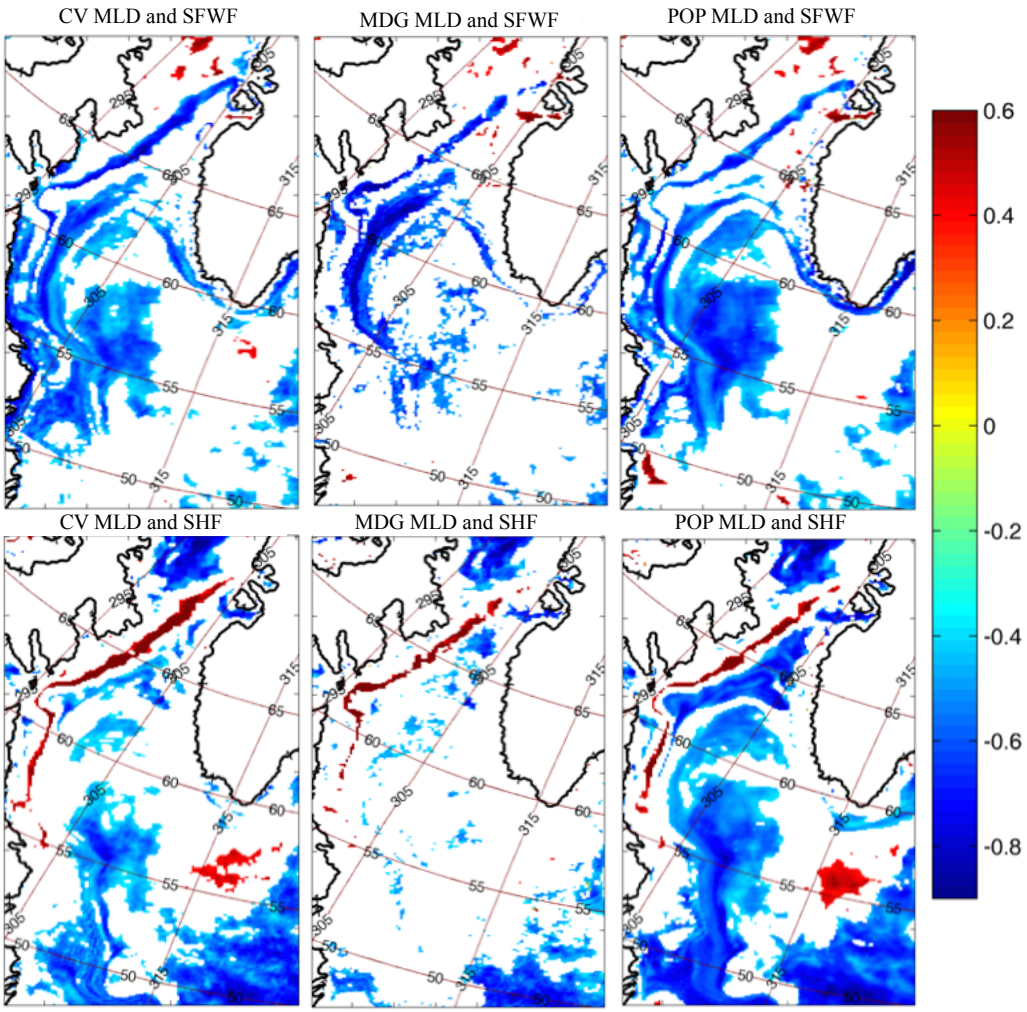

time everywhere in the Labrador Sea and at a 95% confidence level. The two components of surface buoyancy flux are the surface freshwater flux (SFWF) and surface heat flux (SHF). Increasing positive values of these variables indicate that more heat and freshwater is transferred to the ocean by the atmosphere and/or land models, whereas negative values imply that oceanic heat or freshwater is transferred out of the surface ocean to the atmosphere. Our basic assumption for this analysis is that positive buoyancy fluxes (to the ocean) should exhibit negative correlation with MLD, since a buoyancy flux should cause the MLD to reduce or become more shallow. Similarly, negative buoyancy fluxes should cause MLD to become deeper, again exhibiting a negative correlation.

Figure 34 shows the correlation coefficients between the MLD and the two components of surface buoyancy for the R-case, the only simulation where all three MLD methods are available. The correlations are calculated between the winter (JFM) average of MLD and the corresponding time series of either SFWF and SHF (top and bottom rows of Figure 34, respectively). The POP and CV MLD methods produce large swaths of negative correlation between MLD and both components of buoyancy, though the POP method shows a slightly larger area of negative correlations, especially for the MLD correlations with the SHF. Negative correlations imply a physically realistic relationship because as the buoyancy flux increases, the MLD should become more shallow (decrease). The MDG method, however, produces

spatially limited areas of negative correlation compared to the POP and CV methods. In the MLD and SFWF correlation plot, the MDG method produces a concentrated region of strong negative correlations along the cyclonic gyre circulation path, and the MDG/SHF relationship is basically non existent in the Labrador Sea. These correlation maps indicate that the MDG MLD method shows little sensitivity with the surface buoyancy fluxes, especially compared to the other two MLD methods, even though the surface heat loss to the atmosphere is a critical component of the process to deepen the MLD (Clarke & Gascard, 1983; Moore et al., 2014).

The area that often shows strongest negative correlation to surface freshwater fluxes in all three methods is around the Labrador basin in the current pathways where freshwater from the WGCS is transported. This shows that the transport of freshwater in the surface layer impacts MLD in the physically realistic, expected way, and that this relationship is robust between all the methods. Our method of assessing the sensitivity of MLD to surface buoyancy forcing shows competency for this signal.

The other ubiquitous signal seen in all three MLD methods is the narrow strip of positive correlations with surface heat flux, which descends from Davis Strait to the Labrador Current region. This coincides with a strong negative correlation in the MLD sensitivity to the surface freshwater forcing. Both of these signals likely involves the formation of sea ice over the entire Baffin Bay and as well as this area

during the winter months. When the surface water freezes, the surface freshwater receives a negative SFWF through the brine rejection process of the sea ice. This flux deepens the MLD, creating the negative correlation seen in Figure 34. Also, on the heat budget aspect, when sea ice forms, the release of latent heat provides a small positive flux to the ocean. Since temperature does not have a controlling impact on the density structure of the water and therefore the MLD, the MLD follows the forcing made by the salinity/freshwater forcing. So, the positive heat flux to the ocean still corresponds to an increasing MLD, and exhibits a positive correlation. The correlation plots accurately reflect the dominant surface processes occurring upstream of the Baffin Island Current and directly in this region.

As mentioned above, the most widespread signal in Figure 34 is the negative correlations of each of the MLD methods with surface buoyancy, especially for the CV and POP methods compared to the MDG method. The MLD is not only affected by the surface forcing, though. The subsurface component flux of heat, especially from the Irminger derived waters of the WGCS, is considered a crucial component of the Labrador Sea heat budget (Straneo, 2006; Chanut et al., 2008). Although the strong buoyancy loss to the atmosphere is considered the final trigger for deep convection events, the atmospheric forcing throughout the winter months may have intermittent periods of intense heat loss. So we don't expect the relationship to be perfect since the surface buoyancy flux is only one component affecting the MLD.

Figure 35: The percentage of the interior Labrador Sea January, February and March MLD that surpasses five thresholds: 1000, 2000 and 3000m. The region is bounded by the rectangle in Figure 2 and all two methods for each simulation is shown. We also include the POP MLD for the R-case.

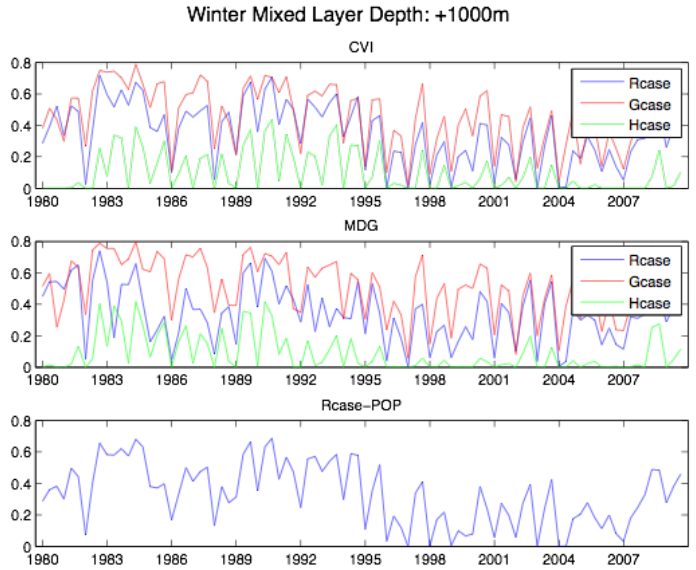


Winter Mixed Layer Depth: +2000m

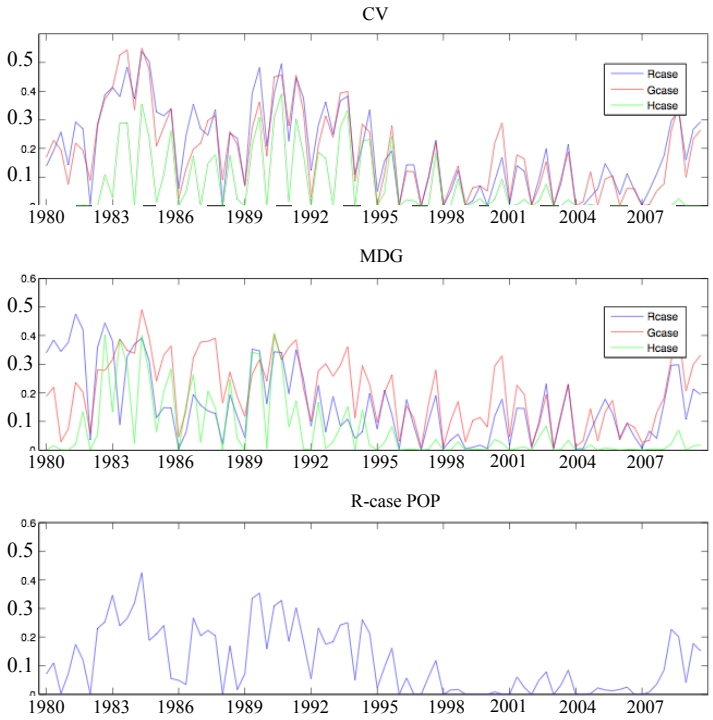

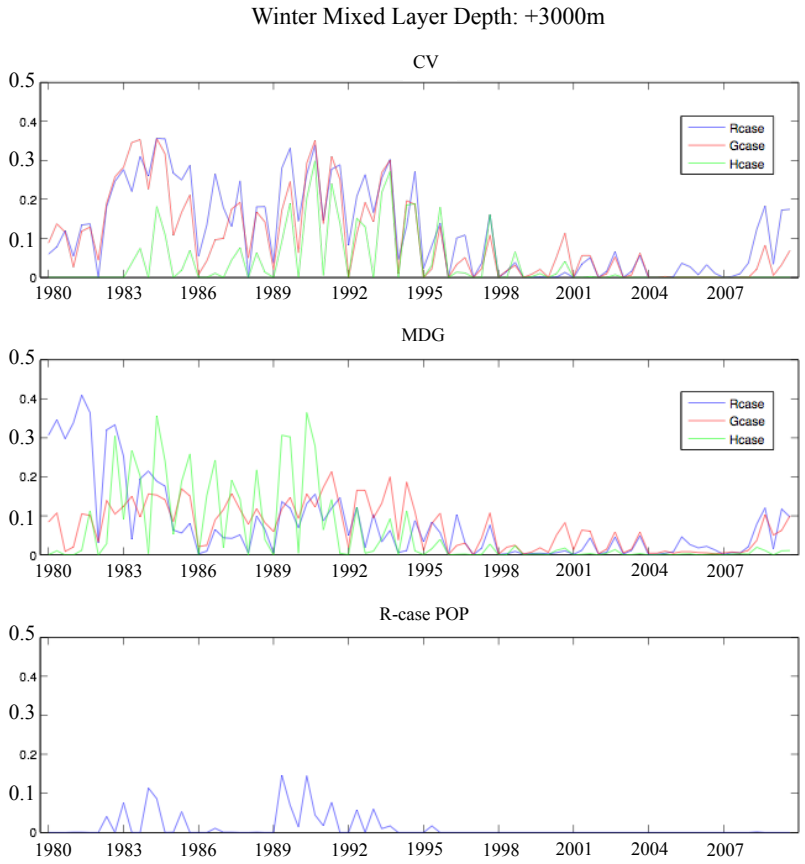


Also, the averaging of the variables reduces the resolution, which also impairs the ability of this technique to capture the entire process. This technique provides a general measure of the each MLD method's sensitivity to the two components of surface buoyancy forcing.

## 3.3 Spatial and Temporal MLD Evolution in the G, H and R-cases

Deep MLDs, almost reaching the full water column depth, occur on a regular basis such that more than 3000m MLD values appear in the monthly mean MLD maps shown previously (Figure 28). The observations of deep water formation paint an

intermittent deep convection signal with interannual variability that is linked to a coupled response between NAO phases and ocean dynamics (Lilly et al., 1999; Lavender et al., 2002). This complicated MLD signal can result in multi-year periods when the Labrador Sea deep convection only reaches down to 500-1300m (such as 1994-2007), before the climatic and oceanic forcings invoke a strong deep convection signal such as the 1600m MLDs determined by Yashayaev and Loder (2009) in the winter of 2007-2008. The model simulations, especially the G and R-cases, by exhibiting an annual cycle of MLDs more than 1800m indicate a higher frequency of deep water formation compared to observations.

To measure the interannual variability of deep MLDs occurring in the Labrador Sea, we investigate MLDs within the black rectangle surrounding the deep basin in Figure 4. The percentage of MLDs in this region that exceed a 1000m, 2000m, or 3000m threshold are given in Figure 35 for each of the three MLD methods. The G and R-cases tend to show more than 40% of the region with MLDs exceeding 1000m for all three MLD methods. The H-case produces lower coverage rates of the 1000m MLD threshold than the other two cases. We attribute this to the spatially uniform buoyancy that the H-case is given by its SSS forcing all across the Labrador basin that provides a buffer to deep mixing of the water column. Across all three methods and cases, there is a reduction in the percentage of MLDs that surpass the 1000m threshold since the mid ’90s. Exhibiting interannual variability like this agrees with observations that

document a weakened deep convection signal during this period (Lilly et al., 2003; Yashayaev & Loder, 2009). The post mid-90s period coincided with a weakly positive or negative NAO, which can be invoked to partly explain the cause for diminished convective activity in the Labrador Sea during this time (Yashayaev, 2007).

In the next range of deeper MLD thresholds, the 2000m values, all three cases have similar levels of MLD values in the region. The closer agreement, especially with the time series of the H-case with the other two cases, may be due to all simulations having similar stratification at depths greater than 2000m. This may be related to the lower vertical resolution that begins at this depth. The H-case even surpasses those of the G and R-cases for brief periods during the MDG method time series. This may be due to the SSS forcing conditions the H-case is given. Once the oceanic and atmospheric contributions create conducive conditions for a deep convection, mixing and homogenization of the water column can occur across a larger area due to the gradual spatial changing surface salinity forcing. Comparison between the CV and MDG methods does not show systematic differences in the tendency for each simulation to produce deep MLDs. The POP method, however, produces both a lower coverage area and more variability in deep MLDs.

The three cases follow the same pattern for the CV case of the 3000m threshold as in the 1000m threshold level. The G and R-case are in closer agreement than the H-case,

Figure 36: The MLD (m) for March 31, 1997 is displayed for the MDG, CV and POP methods in the R-case. A shallowing of the MLDs in the northeast Labrador Sea is observed most prominently in the POP and CV MLD methods. A limited area of deep convection conditions is best created by the POP and MDG methods.

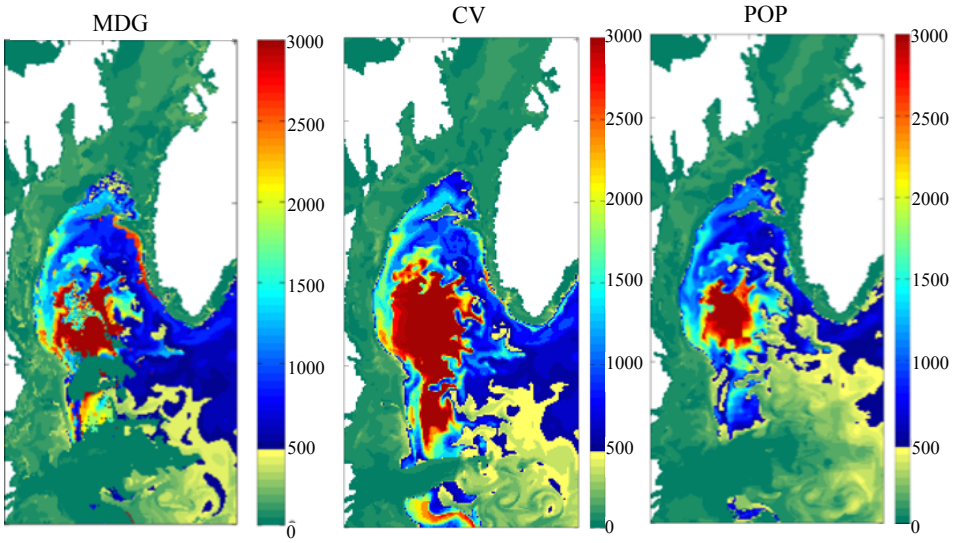


which produces slightly smaller areas of 3000m or greater MLD. For the MDG method, the H-case exceeds the G and R-case for a large part of the 1980s. The same reasoning as before is applied to explain these patterns. In addition, the H-case Finally, the R-case POP method shows a much lower rate of MLDs surpassing 3000m than the other two methods. Since no observations that the author is aware of has recorded such deep MLDs in the Labrador Sea, the POP method performs the best out of all the others to provide an upper limit to the deep convection signal.

The H-case MLD time series in both methods exhibit the most interdecadal variability. It responds to a repeating mean climatological forcing of sea surface salinity restoring that provides an immediate flux of buoyancy across the entire

Labrador Sea. This has previously been attributed to both inhibiting deep convection, but also allowing it to occur across a larger area once enough buoyancy loss is able to penetrate through the water column. The H-case manifests these competing forces by showing several year long periods of reduced convection scattered throughout the 30-year analysis period, especially in the early 1980s and in the post mid-90s period mentioned earlier. Despite this, the H-case on an average annual basis (Figure 28) still produces a significant area of MLD in excess of 2000m within the two-month winter period (February - March) which implies a vigorous onset of MLDs that are some of the deepest observed (Pickart et al., 2002). Also, the H-case often has similar percentages of areas to the G and R-cases that exceed 1000, 2000 and 3000m depth thresholds. Although the H-case produces many apparent merits in its deep convection signal, it has the most constrained and artificially forced model set-up. The G and R-cases, on the other hand, produce MLD evolutions that result purely from internal model dynamics and are able to capture the dampened deep convection signal of the post mid ‘90s.

As a final measure to understand differences between the three MLD methods, we turn to daily output of the R-case. The northeast Labrador Sea is thought to resist deep convection because of its proximity to the buoyant forcing of the West Greenland Current System and the eddy formation region (Lilly et al., 2003; Pickart et al., 2002). However, in the prior study using an earlier version of the ice-ocean

model (McGeehan & Maslowski, 2011), deep convection conditions with MLDs up to 2000m were present in the northeast. This shortcoming was attributed to the treatment of freshwater forcing in the model: a lack of Greenland runoff, or the SSS restoring method. We have analyzed model results for the same date as in McGeehan and Maslowski (2011), i.e. March 31, 1997, as shown in Figure 36. Our current R-case simulation produces on average MLDs that are shallower, between 500 and 1000m. In all three methods, there exists significantly deeper MLDs along the continental slope of the northern boundary of the basin in a very limited region. These are most pronounced in the MDG method with MLDs reaching more than 2500m. The POP MLD method incorporates shallow, 500m MLDs into this region which corroborates the physical conditions of the area. All three methods show minimum MLDs in the westward recirculation path, which carries a significant source of freshwater. In the Labrador Sea region as a whole, the POP and MDG methods have a limited extent of deep convection in the proper location of southwest Labrador Sea, whereas the CV method creates widespread MLDs that reach 3000m for this single day. As the maps in Figure 34 display, the POP and CV methods show the best improvement in the northeastern Labrador Sea compared to prior results. The limited deep convection conditions in the southwest of the basin in the POP MLD further promote that method as most reliable in this assessment.

The direct relation between the northeast Labrador Sea's MLD and its proximity to a freshwater source in the WGCS is explored further in the three experiments. The G-case consistently produces deeper MLDs, reaching ~1200m, in this region than the H and R-cases, as is shown in the mean annual cycle of Figure 28. The curtailed (up to 400m, but often less than 200m ) MLD signal for the H and R-cases indicates that these simulations are able to draw from a nearby buoyancy source. For the R-case, the WGCS transports 84% more freshwater than the G and H-cases to this northeastern region through the MGE transect line. It also maintains a northward flow all year. The realistic properties of the ocean currents in the R-case help maintain lower MLD values in this region, as has been documented by observational evidence (Pickart et al., 2002; Lilly et al., 2003). For the H-case, it relies on sea surface salinity restoring as well as freshwater from the WGCS. Its representation of the WGCS, however, is less realistic as it reverses direction during the late summer to fall.

The flux through the MGM transect line provides an estimate of the exchange between the boundary current and the interior Labrador Sea. The total westward volume transport is 35, 29 and 39 Sv in the G, H and R-cases, respectively. The H and R-cases have a net transport of 29 and 20 mSv of freshwater through MGM, relative to 34.8 (the freshwater content is described more thoroughly in 4.4). The G-case, however, has much less freshwater flux (~1.4mSv) implying that its flow contains mostly water with salinity greater than 34.8. Significantly in the surface layer (top

~120m), the H-case has the highest percentage (76%) of freshwater passing westward through MGM, likely due to the surface salinity restoring. The percentage of freshwater flux in the surface layer of the R-case is next highest, at 71%, and the lowest level of concentration of freshwater (relative to 34.8) in the upper 120m is produced in the G-case at 64%. These differences indicate that the H and R-cases are able to provide a slightly more concentrated source of freshwater to this northeastern Labrador Sea region. Also, with a greater proportion of freshwater in the surface layer, the R-case more closely resembles the H-case's stratification which helps to inhibit the formation of a deep MLD.

In all three model experiments, instabilities may develop along the WGCS, allowing mesoscale eddies to transport and mix freshwater from the coast to the immediate northeastern region or to the interior of the Labrador Sea. The vertical hydrographic structure of the boundary current is an important control on the current speed and stability (Rykova et al., 2015). Fresh coastal waters sharpen the frontal structure over the shelf break, specifically due to Greenland mass loss (Myers et al., 2009). This increasing the current speed (Myers et al., 2009), which can promote eddy activity to inhibit deep water formation. In the G-case, there is very little freshwater in the system (recall that the total terrestrial freshwater flux is low there), and it has the lowest concentration in the upper layer compared to the other two cases. In the H-case, the freshwater is reinforced everywhere due to the surface salinity restoring, so

the sharp spatial gradients in salinity do not exist. The R-case contains a large surface freshwater component along the WGCS and as it veers westward, with a significant proportion of the freshwater in the upper layer. This creates the necessary and realistic conditions for the freshwater to mix via eddy activity in the region, reducing the MLD in the northeast Labrador Sea.

## 3.4 AR7W Vertical Transect Lines

### 3.4.1 Active Deep Convection

The AR7W line was sampled twice during the 1996-97 winter season in October and March. These measurements provide snapshots of vertical stratification across the Labrador Sea that are indicative of our model's deep convection capabilities as well as the veracity of the MLD diagnosis. The March measurements are particularly valuable since they were taken during an active convection period instead of after convection in May, as is usually done as part of the Bedford Institute of Oceanography annual survey (Pickart et al., 2002; Physical Oceanographic Monitoring of the Labrador Sea, 2015). As is shown in Figure 8 in Pickart et al. (2002) and reproduced in Figures 38 below, there is a buoyant surface layer stretching across the entire basin in October. On the edges of the AR7W Line, temperatures and salinities exhibit properties of the boundary current. The WGCS entering the Labrador Sea brings a water mass confined to the shelf and slope that is clearly distinguishable from the interior properties. On the eastern side of the transect line,

Figure 37: (a) The October and March G, H and R-case cross sections of potential density through the AR7W line. (b) The Pickart et al. (2002) observational record of the same variable for comparison.

a)

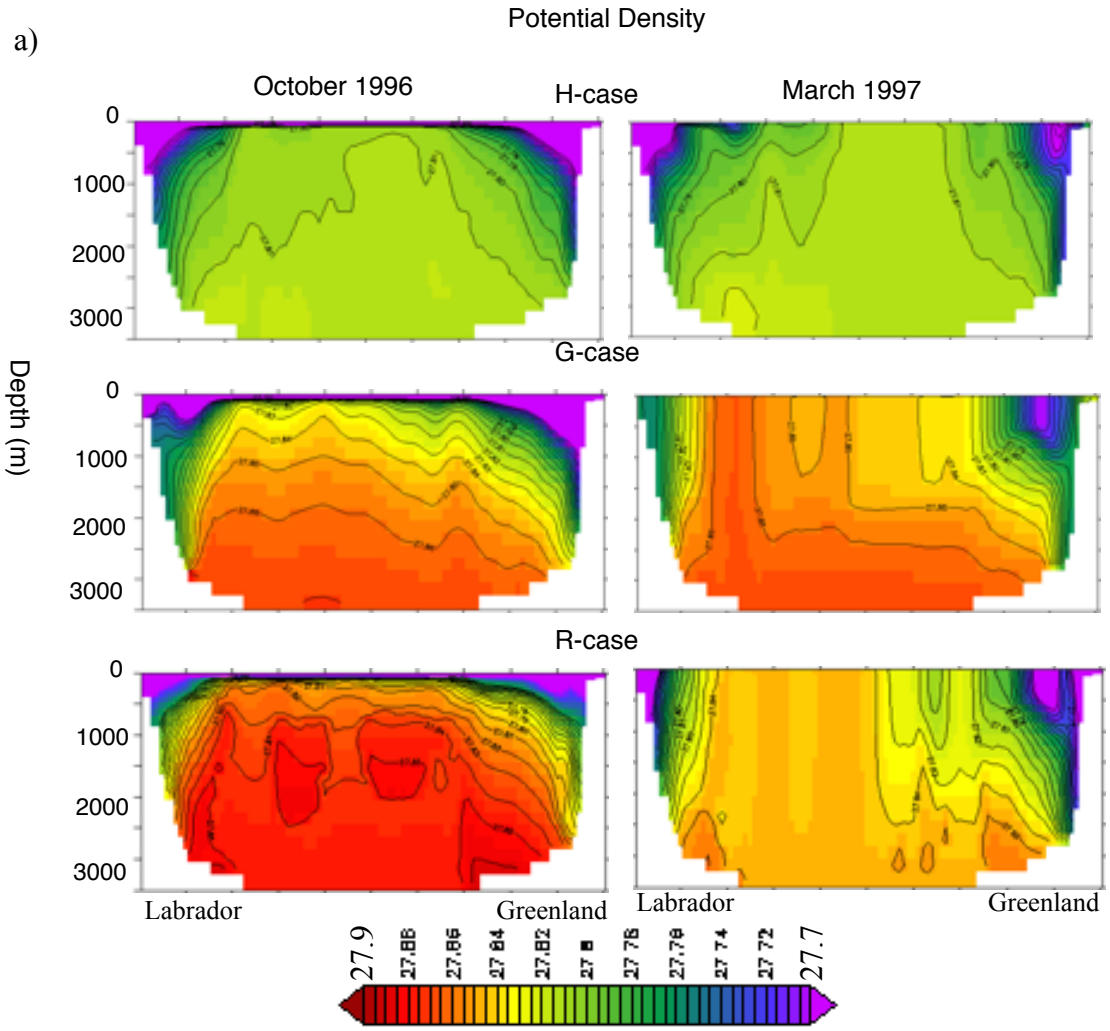


b)

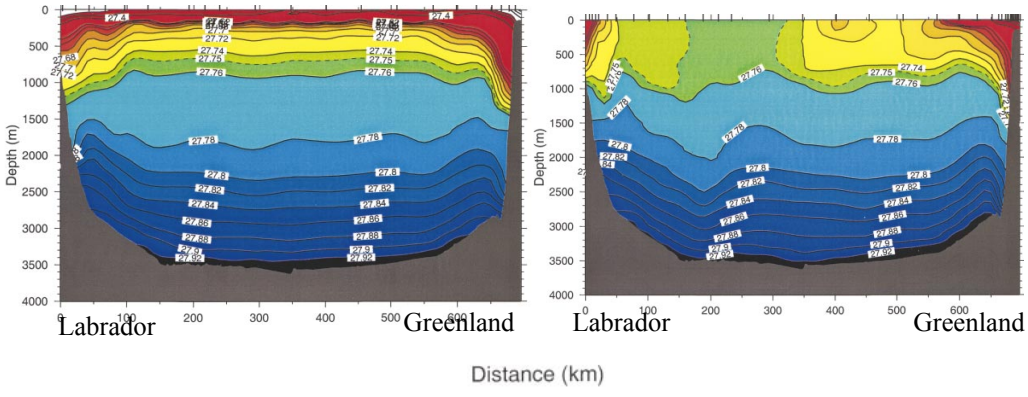

Figure 38: (a) The G, H and R-case cross sections of salinity through the AR7W line. The bottom row depicts the observations from Pickart et al. (2002). (b) The same for potential temperature conditions. The high salinity and high temperature of the IW core at intermediate depth is most distinguishable in the H-case.

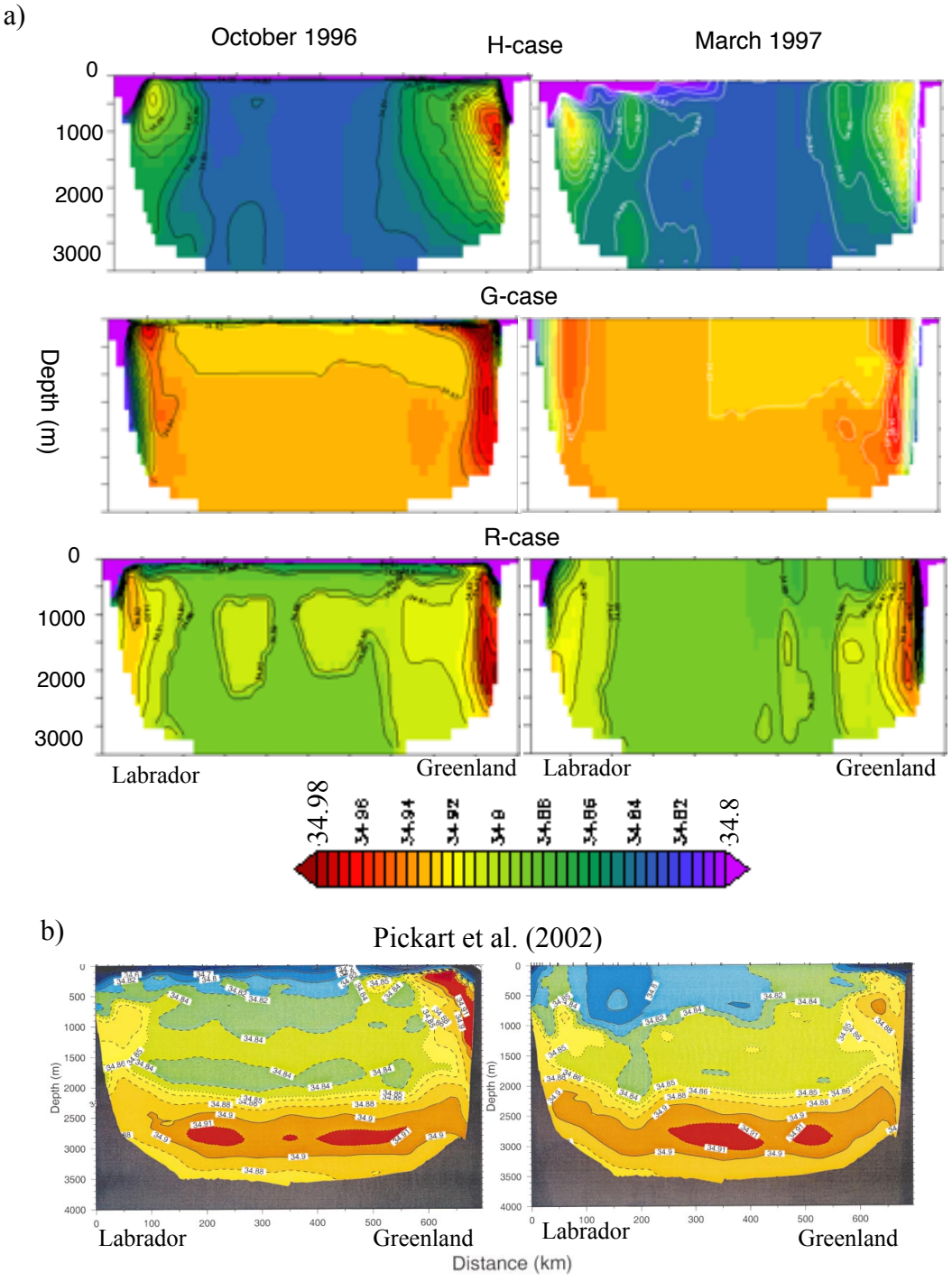

b)

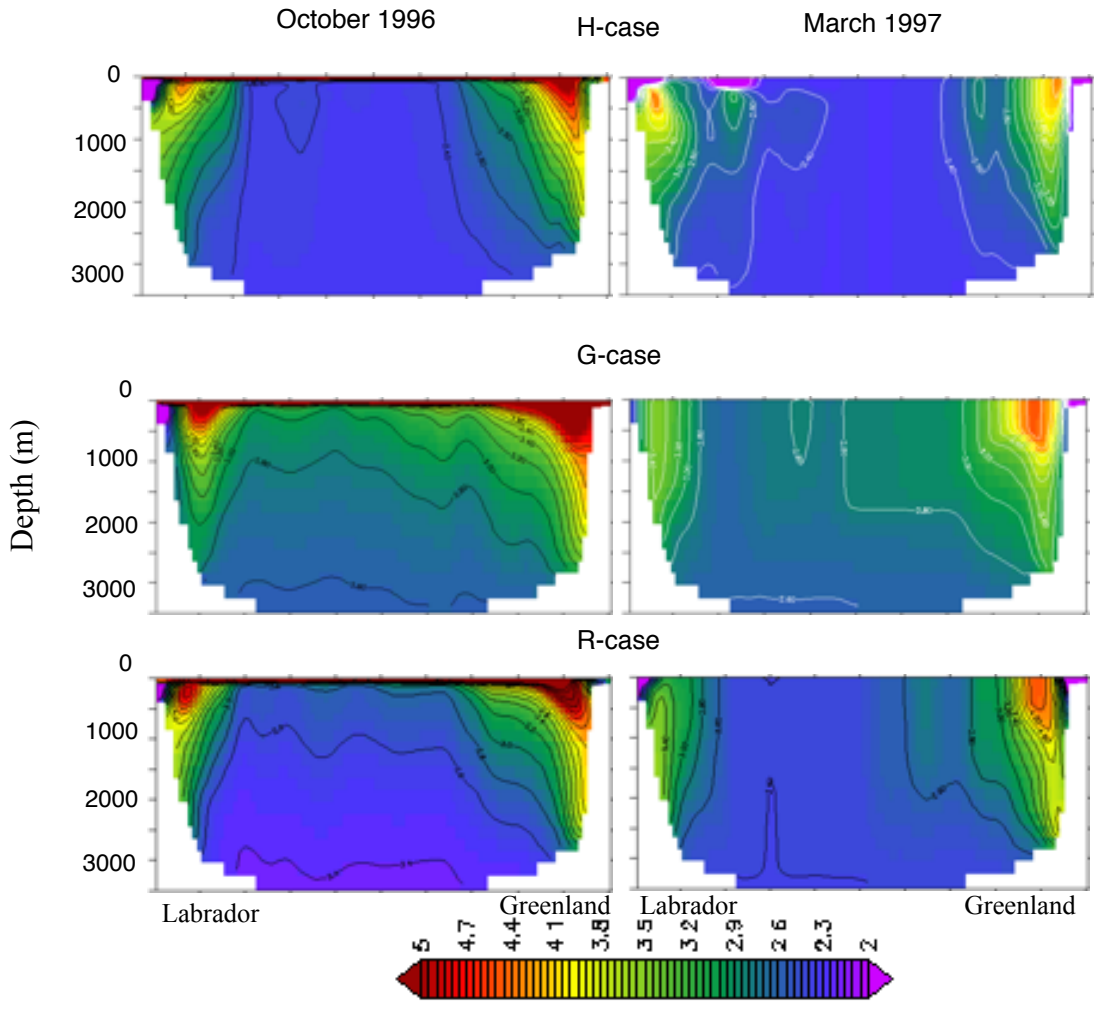


Pickart et al. (2002)

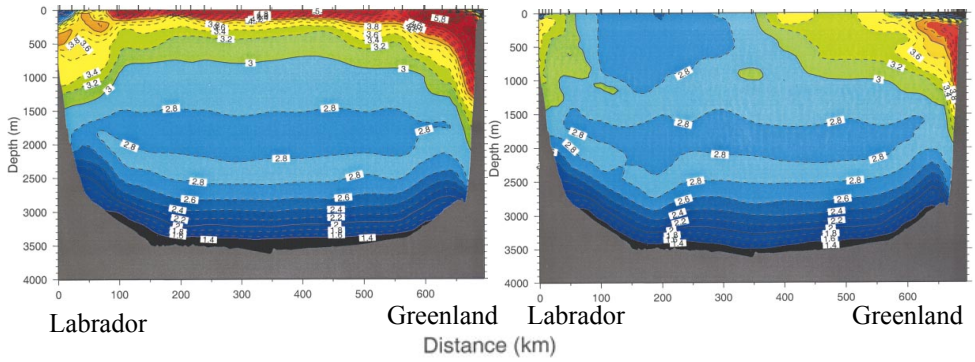

the Irminger core is visible by its anomalously high salinity values. The western side of the transect line still shows the remnants of this water mass, but since the water mass has circulated around the basin, the defined salinity and temperature signal is less strong as the water mass has mixed throughout during its circulation. In the March 1997 survey of the AR7W line, much of the buoyant surface layer has disappeared leaving a homogenous layer of water. On the western side, the properties of this newly convected water mass fit those typically designated as Labrador Sea Water (LSW). Interestingly, on the Greenland side of the basin, there is still a pronounced freshwater cap that spans across the continental slope, though it is less extensive than in October 1996.

We can try to identify the boundary current structure, especially the Irminger water mass, in the model output by using the same patterns of temperature and salinity characteristics used in past studies, such as Pickart et al. (2002) and Rykova et al. (2015). The model simulations produce a similar vertical structure and temporal pattern to the observations. Below, we analyze the hydrographic conditions in our model through the AR7W line, depicted in Figure 29, and compare them to observations. Beginning with the potential density plots for the G and H-cases in Figure 37, the G-case shows strong stratification in the fall period throughout the top 2km of the basin, whereas the H-case has more uniform interior density conditions,

though a freshwater cap exists throughout the transect line. In the G-case, the winter transect of March 1997 exhibits a stark contrast whereby the density structure erodes to a vertically well-mixed upper water column, especially in the southwest corner of the basin. Contrary to observations, more stratification is introduced in the winter-time H-case interior, but the freshwater cap has disappeared, showing some degree of realism.

In Figure 38a, the salinity across the AR7W Line is depicted, corresponding to the active convection captured by Pickart et al. (2002). The H-case more closely matches the observed salinity values and water mass structure at the edges of the basin. During the same season, the G-case better reproduces the vertical salinity stratification pattern across the transect line despite greater than observed salinities throughout the water column. The observations show a salinity less than 34.7 in the top 50-100m (Pickart et al., 2002). The H-case produces slightly higher values in this surface layer (less than 34.8) but the G-case maintains even higher values, around 34.9. We attribute the closer correspondence of the H-case to observations due to its SSS restoring forcing. The intermediate-depth Irminger Water-derived current (IW) on the Greenland side of the AR7W line is more clearly defined in the H-case than in the G-case in both March and October of Figure 36b. The H-case maintains this confined water mass on the Labrador side of the basin but with eroded values due to the mixing that has occurred during the transport around the gyre. The G-case produces the

diffused warm and salty IW characteristics on the Labrador side as well, but the water mass is spread throughout the entire depth range.

The R-case reproduces the observed cycle of strong stratification in the upper water column at the end of summer turning to well-mixed convected water masses in the late winter, as is also depicted in Figure 37. On both sides of the basin, the entire water column shows a uniformly changing stratification that is bent upward, a result of the cyclonic circulation of the Labrador Sea and its susceptibility for deep convection. The salinity distribution in the R-case displays an isolated buoyant layer (less than 34.8) in the top 100m of the water column, which is lacking in the G-case and matches the depth and salinity of the corresponding layer in the H-case. The dominant water mass beneath this surface freshwater layer has a higher salinity of ~34.87 in the R-case than the H-case (~34.83). This creates a stronger halocline in the R-case than the H-case. Observations during October 1996 show a freshwater cap of less than 34.7 in the top 100m overlying an intermediate water mass with salinities averaging 34.83. Although the raw salinity values in the 100-2000m depth range are most similar between the H-case and the observations, the vertical salinity structure, with a sharp gradient separating the very fresh buoyant layer from the waters beneath it, in the R-case shows greatest similarity to the observations. Beneath the halocline, on either side of the basin, the R-case has cores of high salinity IW which decrease radially. There are also patches of anomalously high salinities at depth in the central

basin, which agree with the October 1996 AR7W line observations, though they are at greater depth and higher magnitude. By March, the model shows the upper layer stratification has been completely eroded away, consistent with observations. In the interior of the basin, the salinities span a limited range of 0.03. Where there is a larger variability of stratification along the continental slope, it is structured in a similar way to the October transect with high salinity cores that decrease radially and isopycnals that are bent downward.

The boundary current structure can be identified in the R-case model output, though it tends to be less distinct than in observations based on this particular set of snapshots. On the Greenland side of the basin, the IW is correctly positioned above the continental slope but appears at all depths, unlike in observations where the water mass is restricted to the intermediate depth range. In the R-case, the core of the highest salinity water extends to a depth greater than 2000m, whereas IW should be contained within the 200-1000m depth range. As demonstrated by measurements, the fresh cold Arctic origin waters exist shoreward and above the IW layer, and the R-case is able to reproduce this. Residual signals of this structure appear on the western side of the AR7W line where IW is very diffuse, spanning the entire depth of the water column similar to the G-case. In the winter transect, this signal is further reduced and shows signs of convection. The corresponding March observations from Pickart et al. (2002) still show remnants of the IW, although some mixing and/or

convection seems to have occurred since the elevated temperature and salinity signal is less coherent than in the fall.

### 3.4.2 Restratification and LSW Production

Comparison between the observed water properties along the AR7W line in May 2007 and 2008 reveals that a large mass of Labrador Sea Water (LSW) was produced in 2008 (Yashayaev & Loder, 2009). These measurements, taken in the typical month (May) when the Bedford Institute of Oceanography (BIO) occupies the AR7W transect line, provide information on how the Labrador Sea conditions respond to a deep convection event and how amenable our model is at reproducing these water mass movements. In the west-central sector of the basin, a homogenous water mass of well-mixed waters down to ~1500m appears in the measurements made only in May 2008, though lighter waters had already encroached the top ~400m by the time the data was gathered in May. Because a similar large patch of homogenous waters was not observed in 2007, this indicates that vigorous convection occurred during the 2007-2008 winter. Also, the rapid nature of restratification in the upper layers of the basin is highlighted by the May transect line, since already in May, merely two months after the peak winter conditions, a flooding of buoyancy all across the basin is observed. These observations are compared to the G, H and R-case results below.

Figure 39: (a) The potential densities in May for 2007 and 2008 in the simulations. Stratification throughout the interior Labrador Sea is limited in the G and R-cases, but most developed in the H-case. (b) The potential density given by Yashayaev and Loder (2009) for comparison.

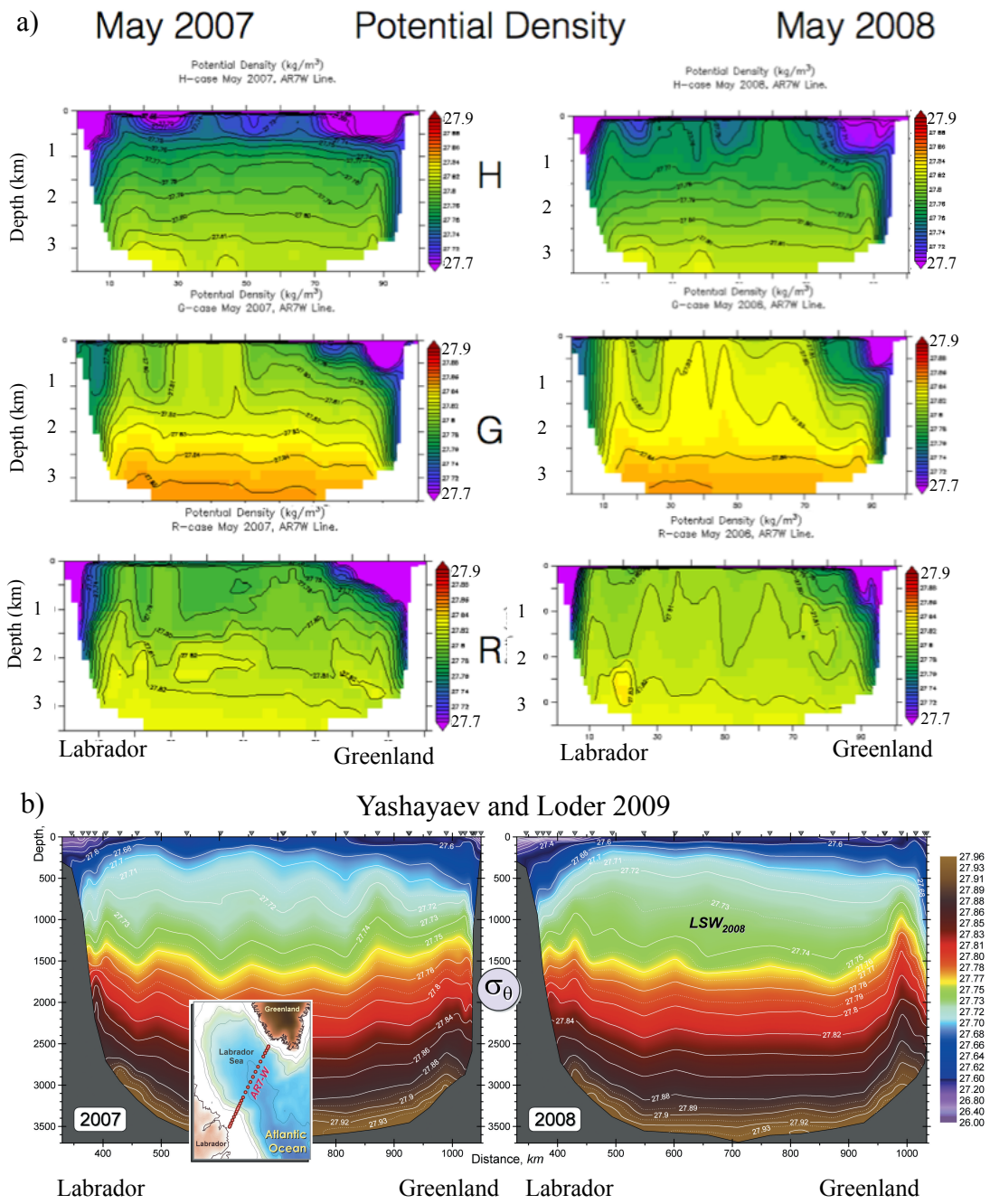

Figure 40: (a) The vertical cross section of salinity during May 2007 and 2008 along the AR7W Line for the G, H, and R-cases. The freshwater cap is most prevalent in the H-case. There are intermediate levels of stratification in the R-case, but the G-case shows little vertical salinity stratification. (b) For comparison we provide the corresponding observations from Yashayaev and Loder (2009).

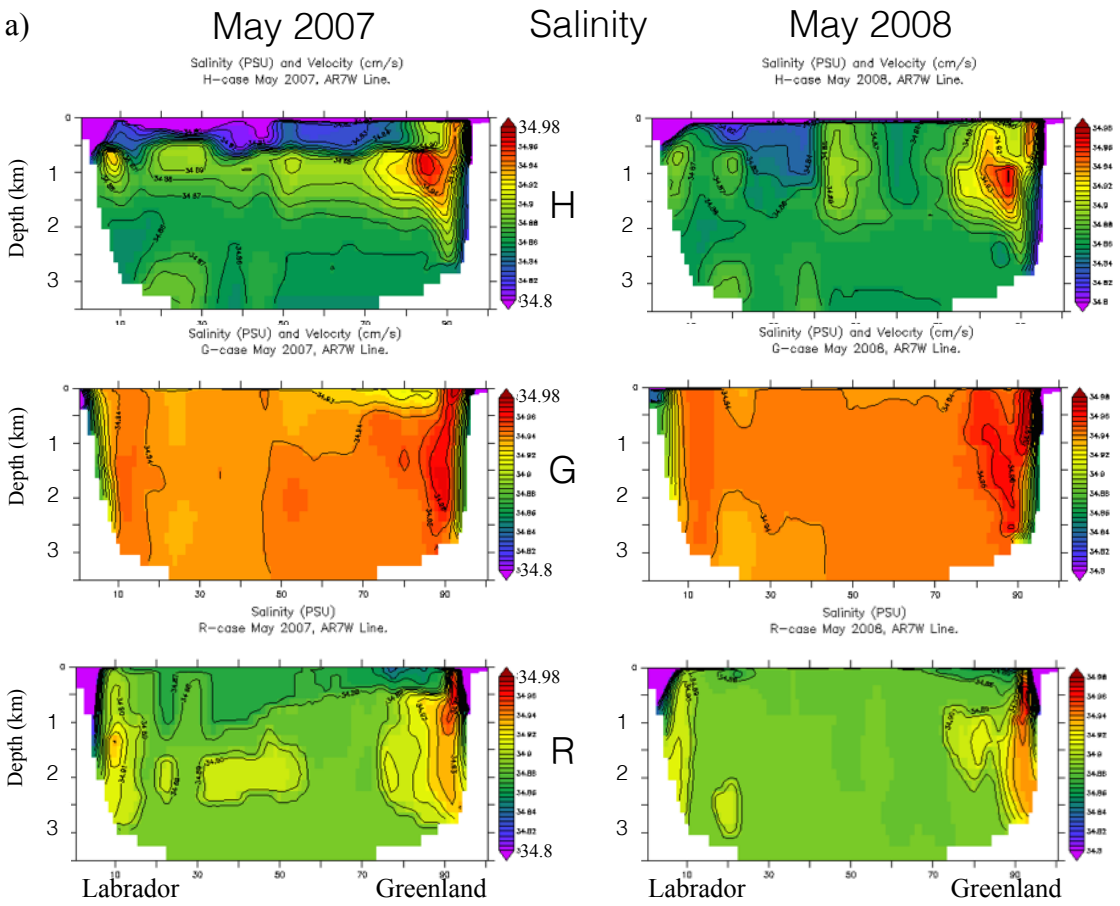

Figure 41: (a) The potential temperatures through the AR7W Line in May 2007, 2008. G and R-cases show similar levels of stratification, though the R-case has lower temperatures. The H-case shows the most realistic levels of stratification. (b) The corresponding observations from Yashayaev and Loder (2009).

a)

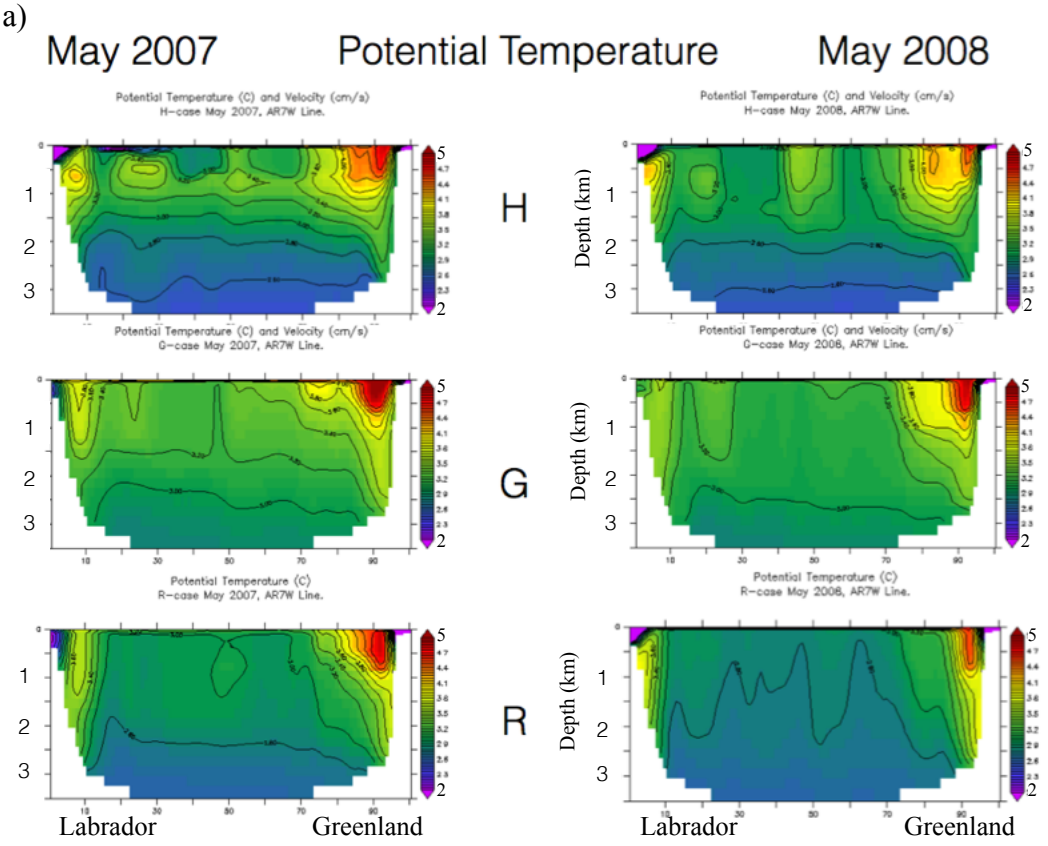


b) Yashayaev and Loder (2009)

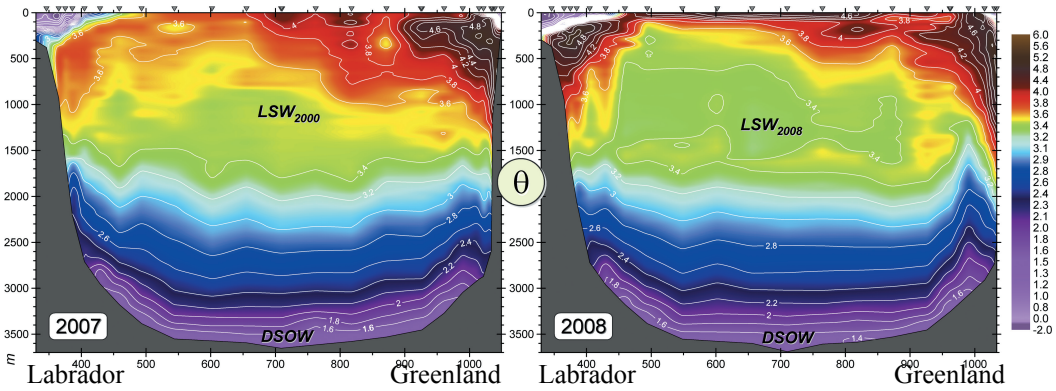

The H-case more closely resembles these AR7W observations in both spatial pattern and absolute magnitude in the surface layers. In 2008, a thicker homogenous near surface water mass was produced as compared to the prior year. This is shown in Figures 39, 40, and 41 where vertical cross sections of potential density, salinity and temperatures are given. Observations show similar salinities of 34.85 and slightly warmer temperatures (by ~0.2 ºC) in the convected zone. Temperatures are cooler than observed in the deepest ~1500m of the basin, except for the bottom 500m, where they are warmer. Salinities are fresher in that depth range compared to observations, but the H-case is able to capture a slight reduction in salinity in the bottom couple hundreds of meters of the basin. Finally, the H-case has a less vigorous thermocline and halocline than the observations.

The G-case shows even weaker stratification than the H-case. The entire basin is filled with salinities that range from 34.93-34.94 which are much higher than observed, while the temperature varies between 3.0 and 3.4 ºC, slightly cooler than observed in intermediate depths but warmer than the bottom kilometer. There is no discernible well-mixed water mass of LSW characteristics anywhere in the cross section of the AR7W Line. The vertical temperature structure still reveals stratification throughout the center of the basin. The salinity in the G-case exhibits a couple of pockets of fresher water in the upper 500m. The potential density along the AR7W Line, however, does indicate a homogenous water mass along in the south-

central part of the basin, though it appears in both years and is less widespread than indicated by observations.

The R-case output is similar to the G-case in that overall there is very little vertical stratification resulting in salinities and temperatures in the top half of the basin that are higher and lower than observed, respectively. The salinity varies from 34.88 at the surface to a maximum value of ~34.90 for both 2007 and 2008. Across most of the interior basin, the salinity of the entire water column hovers around 34.89. The R-case temperature within the basin varies from about 3 ºC at the surface to less than 2.6 ºC. Overall these are smaller surface to bottom changes in water properties than the observations, which is conducive towards more regular intervals of deep convection due to the smaller gradient in water properties. Although both years show regions of homogenous water masses in the upper 1500m, a further reduction in stratification is visible in 2008, which agrees with observations. Overall, the R-case shows cooler and fresher interior water properties compared to the G-case, but the H-case shows the most realistic vertical stratification and raw temperature and salinity values compared to the Yashayaev and Loder (2009) transect lines. In this way, the R-case model performance is an improvement compared to the more constrained G and H-cases.

The freshwater cap differs between the cases, and only the H-case shows realistic thicknesses of low salinity water across the basin like in the cross sections shown in

Yashayaev and Loder (2009), which is typical of the rapid spring restratification process. The freshwater lenses in each of the cases are shown more clearly in Figure 42, where the top ~1400m of salinity across the AR7W line is displayed in each of the cases for both May 2007 and 2008. The H-case has at least a 50-100m thick freshwater lens during both years whereas there is only a very slight reduction in

Figure 42: The upper 1400m of the salinity through the AR7W Line for May 2007 and 2008 for the three model simulations. The ability for the model to quickly restratify across the entire Labrador basin is assessed through this plot, with the H-case producing the most developed freshwater lens.

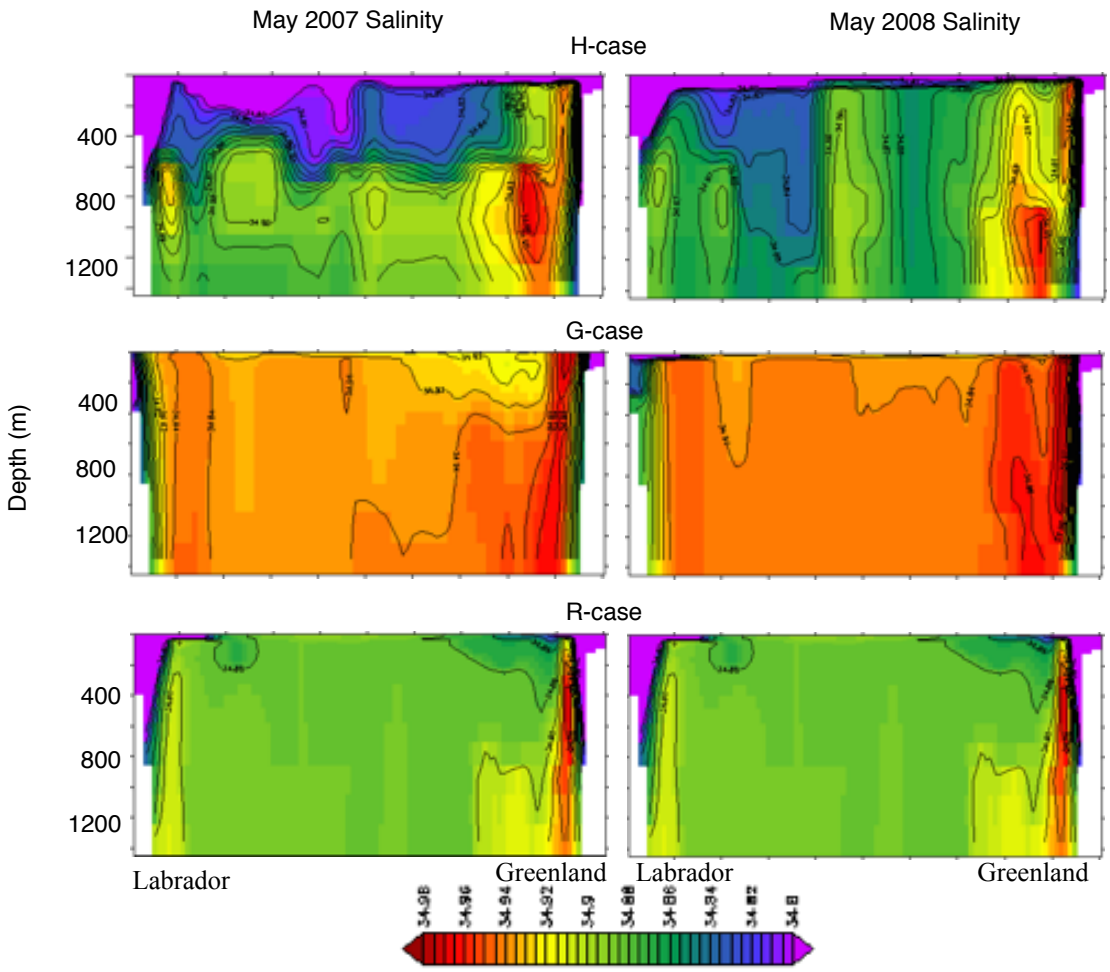

salinity across the entire basin in the G and R-cases. The R-case has a significant source of low salinity water on the shelf and slope, especially on the Labrador side.

The H-case undergoes sea surface salinity restoring on a monthly basis, and this is the source of the rich 'freshwater' cap that is able to spread across the entire basin. Based on the flux estimates through MGM (section 3.3), the H-case has the largest freshwater flux that veers westward towards the interior Labrador Sea, and this is attributed to the SSS restoring. This ample freshwater artificially provided to the H-case maintains the realistic-looking characteristics of the Labrador Sea. The G and R-cases, however, which rely on model physics to redistribute the freshwater from the boundary to the interior, show small signs of freshening across the basin even at this early stage of the melt season in May. The G and R-cases must improve and produce a more significant freshwater lens by May as observations show that typically the restratification of the Labrador Sea has been fully developed by this point of the season (Katsman & Spall, 2004; Straneo, 2006; Yashayaev & Loder, 2009).

# Chapter 4: Mesoscale Eddies and Their Role in the Redistribution of Freshwater

## 4.1 Eddy Kinetic Energy

The Labrador Sea eddy field serves as a critical mechanism for mixing shelf and interior properties. The eddies provide the buoyancy needed to restratify the central basin after severe winters. Mesoscale eddies are primarily produced in the boundary current along west Greenland (e.g. Cuny et al., 2002; Maslowski et al., 2008). They enter the interior Labrador Sea by two main trajectories: along the faster route across the basin following the westward recirculation pathways (McGeehan & Maslowski, 2012) or, for the larger and more persistent eddies, by separating and drifting southwest (Rykova et al., 2009). Surface drifter observations from 1993-1997 show that two regions of heightened eddy kinetic energy (EKE) occur within and near the Labrador Sea. The maximum region of EKE occurs just to the southeast of the Labrador Sea in a northwest extension of the North Atlantic Current, while the secondary maximum occurs in the eastern Labrador Sea near the 'bathymetry gap' region (Cuny et al., 2002). The same results were also shown by TOPEX/Poseidon and ERS satellite altimeter measurements during 1997-2001 (Brandt et al., 2004).

As discussed previously, all three models adequately simulate the location and magnitude of the first maximum in EKE near the North Atlantic Current, but all underestimate the secondary maximum EKE region, shown in Figure 43, when EKE

Figure 43: Eddy kinetic energy ($cm^2/s^2$) is calculated from monthly mean velocities and the all-time mean for the 1993-1997 time period. The average of the surface layer is shown below. EKE in the Labrador Sea region represents the first maximum at the northwest extension of the North Atlantic Current well, but falls short of reaching ~400 $cm^2/s^2$ in the secondary maximum near the west Greenland shelf.

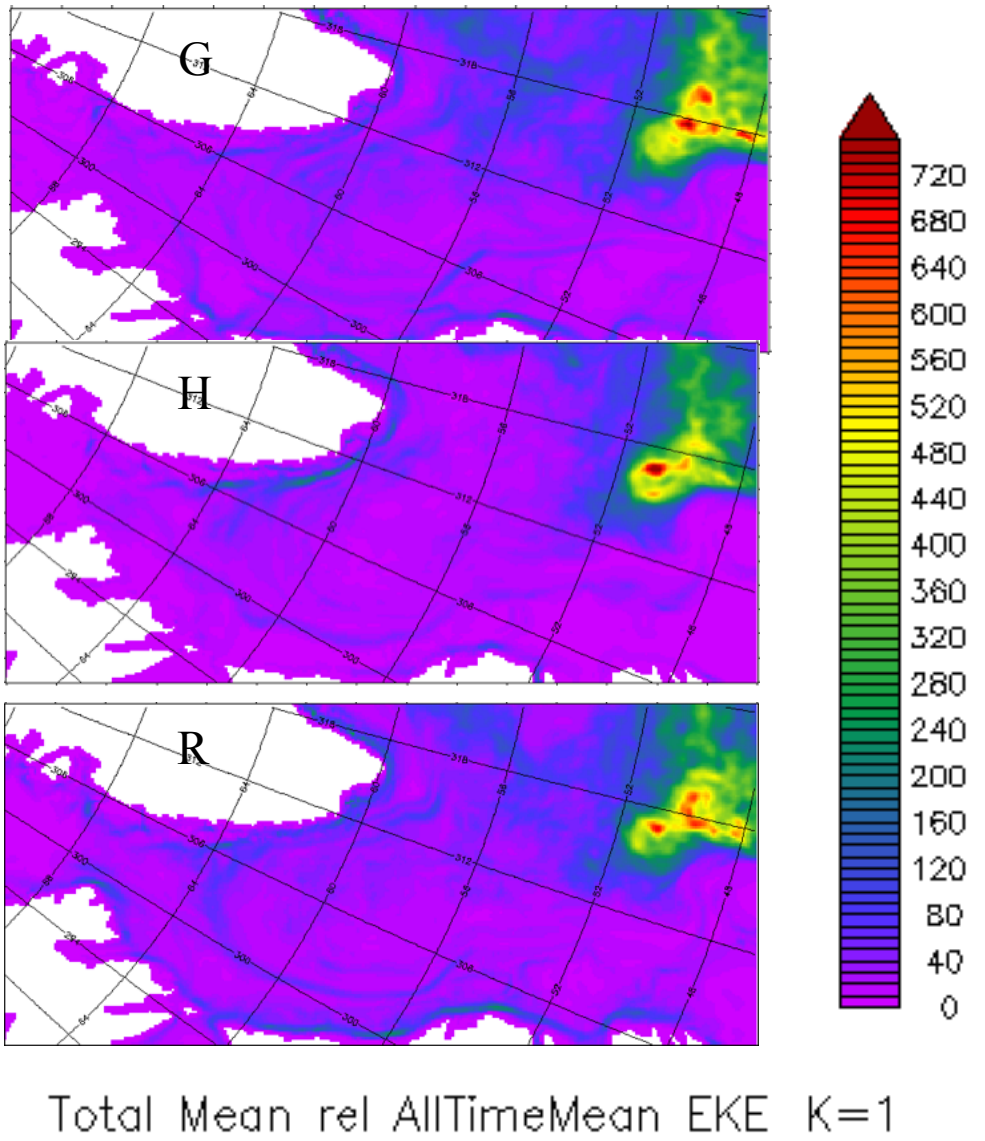


is derived from the mean monthly model output of velocities. This shortcoming in producing the secondary maximum EKE along the 'bathymetry gap' is attributed to

Figure 44: (a) The mean surface EKE ($cm^2/s^2$) for 1993-1997 derived from surface velocity deviations from the all-time mean velocity is shown below for the surface layer for the R-case. The first maxima is more widespread and reaches higher values. The secondary maxima shows great improvement with a more realistic spatial structure and magnitudes. (b) The observed EKE ($cm^2/s^2$) derived from surface drifter data for the same time period from Cuny et al (2002).

a)

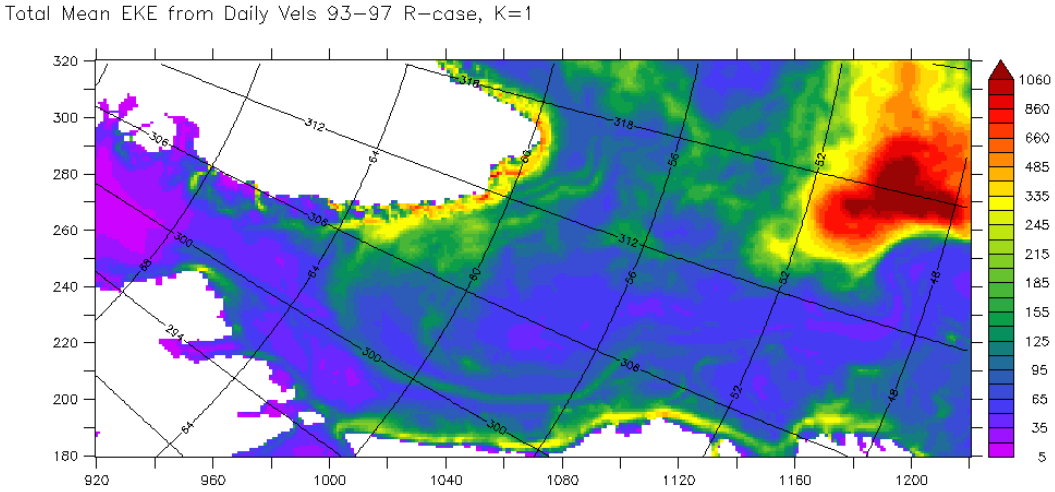


b)

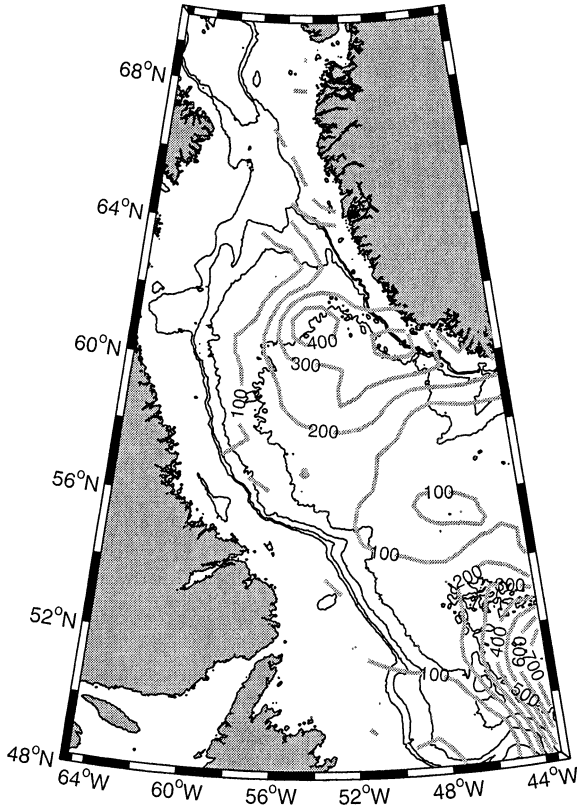

the method of calculation of EKE from the monthly averaged model output, which already smooths the velocity field. To verify that, we also estimate EKE based on the daily averaged R-case output of surface velocities, and demonstrate (Figure 44) that this captures more of the velocity variability and can directly compare with observations.

### 4.1.1 EKE from Model Monthly Mean Velocities

In our first estimation of EKE for the G, H and R-case experiments, velocity deviations from the 1993-1997 mean are calculated from mean monthly velocity outputs (Figure 43), as $EKE=1/2(u'^2+v'^2)$, where u' and v' are the horizontal and vertical differences between the monthly averaged output and the all-time mean (for this study period 1993-1997). This five year time series of EKE was averaged to produce an all time mean of EKE as well as the mean annual cycle during this time. Here, like in the observations (Cuny et al., 2002; Brandt et al., 2004), we investigate the all-time mean EKE in the secondary maxima region based on mean monthly output where all three cases fall short compared to EKE magnitudes derived from observations.

All three models produce similar EKE values that are elevated beyond the background along the narrow and steep slope along south-western Greenland. Near Cape Desolation and further north, ~64ºN where the WGCS splits to the north and

west, the H and R-cases reach even higher values than the G-case. The H-case produces the most continuous high EKE signal between Cape Desolation and ~64ºN, reaching almost 200 $cm^2/s^2$ in several spots following the shelf break in this region. All simulations tend to produce elevated EKE that align parallel to the coast of Greenland in a N-S orientation, whereas the observations show a pattern that infiltrates into the central Labrador Sea, towards the southwest from the Greenland shelf. The G and R-cases more closely resemble the observations in this way, with elevated EKE patches extending further into the interior Labrador Sea than in the H-case. However, these patches are still oriented in N-S strips and the magnitudes of the high patches hover at no more than ~100 $cm^2/s^2$, significantly less than observations (Cuny et al., 2002).

The lower EKE values calculated here are expected because of the temporal smoothing applied in the mean monthly output. According to Maslowski et al. (2008), EKE derived from model monthly averaged velocity fields represents ~15% of that estimated from daily velocity output. If one would account for that, this would bring the maximum EKE values in the H and R-cases to ~440 $cm^2/s^2$, which would be comparable to the observed peak in EKE near Cape Desolation (Cuny et al., 2002). For the G-case, this would amount only to about half of that value.

### 4.1.2 EKE from Model Daily Mean Velocities

In order to verify the limitations of the EKE estimation from model monthly mean fields, we also calculate EKE from the R-case daily velocity output. Here, daily velocity deviations are calculated from the 1993-1997 daily mean output, and the mean EKE for this period is shown in Figure 44. Using the high frequency daily mean velocities instead of the monthly mean velocities brings the EKE distribution closer to the observational estimates. The results by Maslowski et al. (2008) utilized in the previous section are corroborated by these results since the R-case EKE based on daily velocity fluctuations increased by at least 85% compared to the EKE based on monthly mean velocities. In the all-time mean map of EKE, two maxima are present and they both exhibit higher magnitudes compared to the EKE estimates derived from monthly mean model output, and significantly, the secondary maximum shows much better agreement with observations. In the northwest extension of the North Atlantic Current, there is a much larger region of 600 to 1000 $cm^2/s^2$ values between 48ºN and 52ºN, which agrees with existing observations (Brandt et al., 2004; Cuny et al., 2002). The secondary maxima along west Greenland has increased by almost a factor of two in most of the region. The spatial extent of the enhanced EKE region is also more realistic, with a high energy area extending into the interior Labrador Sea from the 'bathymetric gap', instead of the banded features produced based on monthly model output.

Figure 45: Winter and summer surface EKE ($cm^2/s^2$) for the R-case during 1993-1997. The winter displays greater EKE, especially near the west Greenland slope. This corroborates observations of maximum WGCS instability during this season.

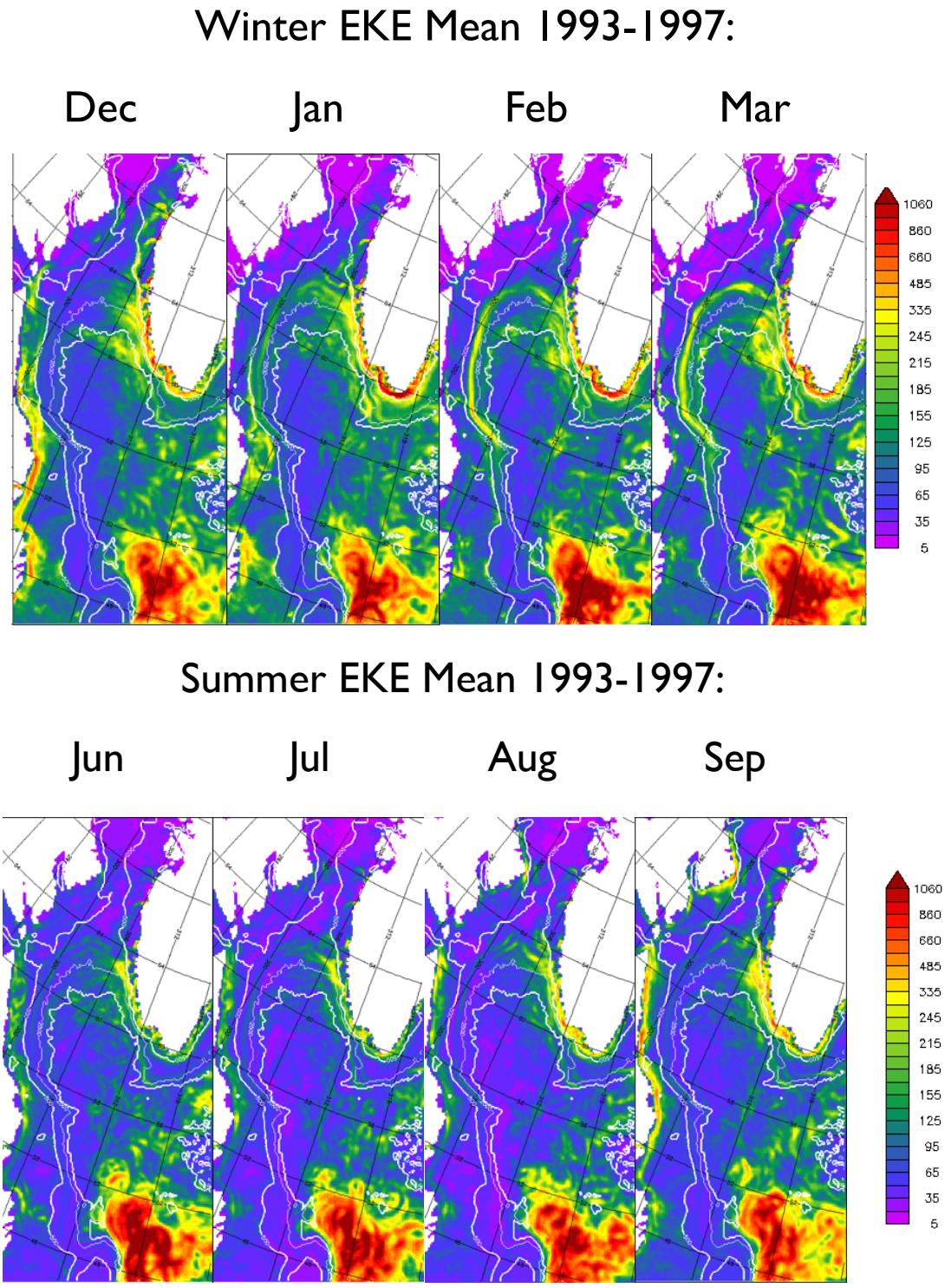

The observations also show a pronounced seasonal cycle whereby a maximum EKE occurs in winter and a minimum in summer (Cuny et al., 2002; Brandt et al., 2004). In Figure 45, the modeled seasonal variations of EKE are presented by calculating mean monthly averages of the daily EKE during the period of 1993-1997. The winter-time maximum is clearly shown by comparing the December-March maps to the June-September maps. In December-March, a more active EKE field surpassing $400cm^2/s^2$ extends into the interior Labrador Sea, past the 3000m isobath, whereas in the summer, such values only occur along the shelf of Greenland.

This demonstrates that the R-case exhibits realistic EKE distribution and seasonal variability compared to observations, when EKE is calculated from daily velocity outputs. This also corroborates the 85% correction (Maslowski et al., 2008) to estimate EKE derived from monthly mean velocities for comparison with the more realistic daily velocity-derived values. We can therefore use this approach in the G and H-cases, where daily velocity output was not available, to estimate more realistic EKE fields for comparison with observations.

## 4.2 Coastal Gradients of Sea Surface Height

The dynamical topography of the ocean surface, or sea surface height (SSH), relative to the geoid is determined primarily as a result of tides and ocean currents due to geostrophic and wind forcing, and to small degree, changes in the density structure of

Figure 46: (a) This map of the bathymetry (m) of the study region displays the outline of the region following the west Greenland coast where subsequent analyses on the SSH is performed. (b) The mean SSH (cm) for March (top row) and September (bottom row) for the G, H and R-cases centered around the region outlined in black. White contours indicate the 3000,2000, 1000 and 500m isobaths.

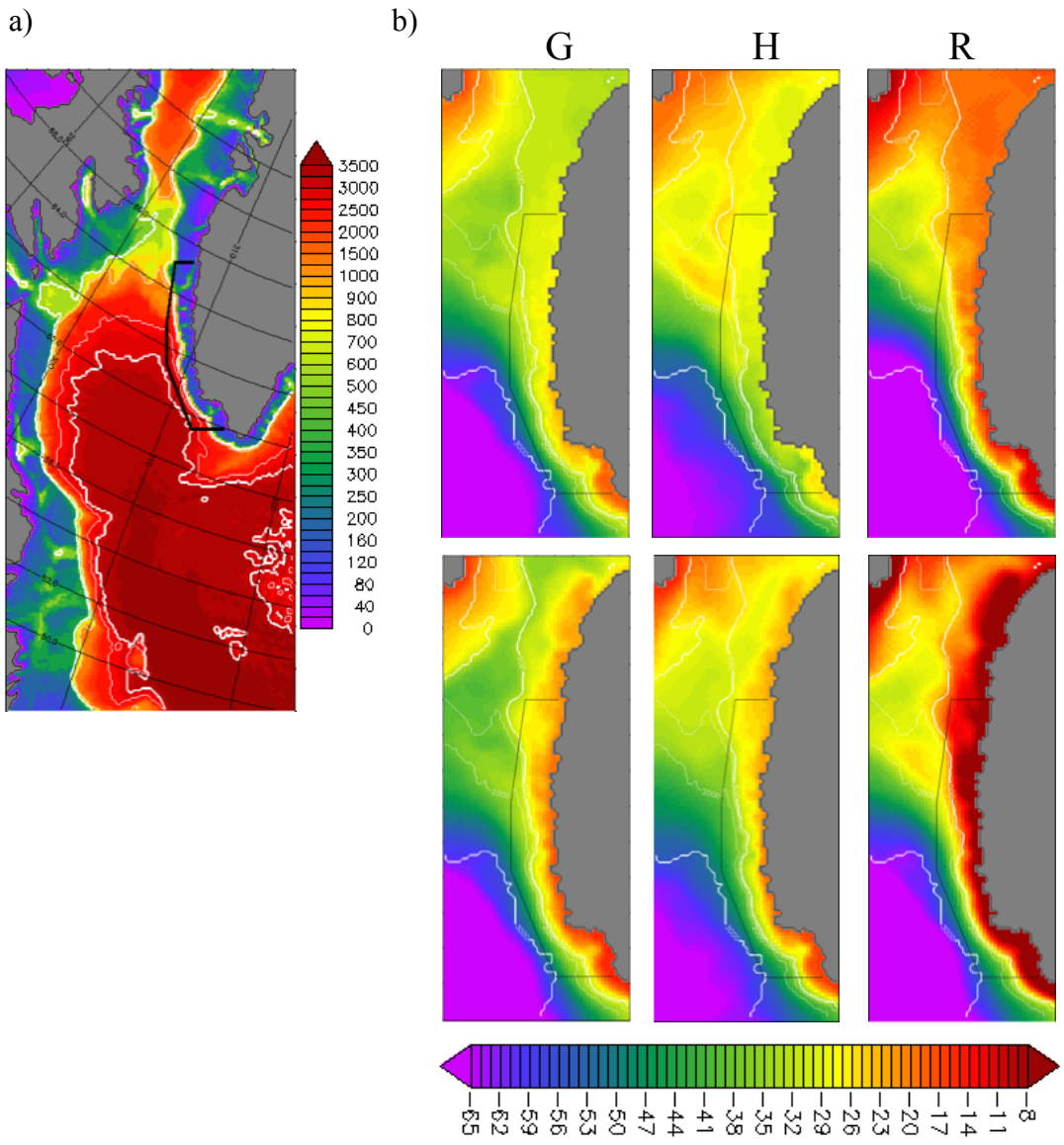


the water column (Stewart, 2009). In the G and H-cases, identical atmospheric forcing is provided so that the differences in SSH between the two cases are caused

by ocean dynamics, ultimately arising from the representation of freshwater forcing. In contrast, the variation in the R-case SSH compared to the G and H-cases may be caused by atmospheric forcing and coupling with the ocean and/or any of the oceanographic causes.

The ample buoyancy along the west coast of Greenland creates a buoyancy driven flow of the boundary current system (Wolfe & Cenedese, 2006; Rykova et al., 2015). Further inshore of the main WGCS, the presence of a buoyancy-driven coastal current has not been observed. However, its existence has not been ruled out because there have been no observations within the ~10km lengthscale, the Rossby radius of deformation, that would carry such a flow (Bacon et al., 2008). Our models show a partial representation of a coastal current from two sources, however our model lacks the resolution to fully resolve such a feature. First, there is a current along the coast in the vertical cross section plots of the MGE transect line (section 2.3). However, this current is not geographically or dynamically distinct from the main boundary current along the slope, as a coastal current should be (Sutherland & Pickart, 2008; Bacon et al., 2008). Our second evidence of the generation of a coastal current is through the elevated SSH along the west coast of Greenland. The buoyant coastal waters accumulate along the coast creating a topographical bulge in the ocean surface. The coast-to-interior pressure gradient is in geostrophic balance with the Coriolis force, producing an along-coast northward current. In our model results, this gradient due to

the buoyant waters accumulating along the coast affects the main WGCS along the coast, too. It is not limited to the 10km wide region along the coast. Thus, the buoyancy variations along the west Greenland shelf impacts not only the coastal current representation but also the WGCS.

In this section, we further analyze the SSH and its gradient to understand how the buoyancy fluxes impact the stability of the WGCS. The WGCS exhibits seasonal variations in speed and hydrographic properties due to the buoyancy fluxes (Rykova et al., 2015). In winter, the eddy production is maximum because of the greatest shelf to interior density gradient (Prater, 2002; Lilly et al., 2003; Eden & Boning, 2002; Katsman et al., 2004; Rykova et al., 2015). This enhances the current baroclinically and is thought to be the dominant cause of the instability (Rykova et al., 2015; Saenko et al., 2014; Katsman et al., 2004). However, some authors point to a barotropic instability as the cause of the eddies (Chanut et al., 2008; Eden & Boning, 2002; Brandt et al., 2004). The ultimate cause of the eddies may be difficult to parse, but an increased WGCS speed as it flows over steep bathymetry results in the hydrodynamical effect of the current being more prone to instabilities (Eden & Boning, 2002, Katsman et al., 2004; Wolfe & Cenedese, 2006, Rykova et al., 2015). The SSH gradient in the model simulations and the ocean's response to geostrophically balance this forcing provides a measure of one mechanism that results in an enhanced current speed for the WGCS.

As is shown in Figure 46, the three cases recreate the bulge in SSH along the west coast to differing degrees, subject to the realism of representation of freshwater runoff from Greenland and the upstream East Greenland Current. The mean September and March SSH from 1980-2009 for each simulation are displayed to show the importance of the seasonal freshwater signal. When the freshwater flux through the system is high at the end of summer, the SSH gradient from coast to interior is greater than during March, when the SSH along the Greenland coast is reduced. The R-case exhibits the strongest gradients.

To further quantify the SSH variability between the simulations, we assess the SSH and SSH gradient within the region indicated by the black irregular shape outlined in Figure 46. This region starts 1-2 grid cells from the coast and extends out 10 or 11 grid cells, or ~100km, across the shelf, extending out to nearly the 3000m isobath at the deepest area. It includes the bathymetry gap, up to ~65ºN, where most of eddies in our simulations are shed (i.e. the area where the 1000m and 1500m isobaths diverge from the coast). The mean annual cycle of SSH and the coast to interior SSH gradient is calculated for this region and shown for all three cases in Figure 46.

In the mean annual cycle of SSH (Figure 47a), the G and H-cases have a similar temporal pattern of minimum SSH in the early summer and maximum in the late fall

Figure 47: The mean annual cycle of the average (a) SSH and (b) SSH gradient within the study region outlined in the prior plot.

a)

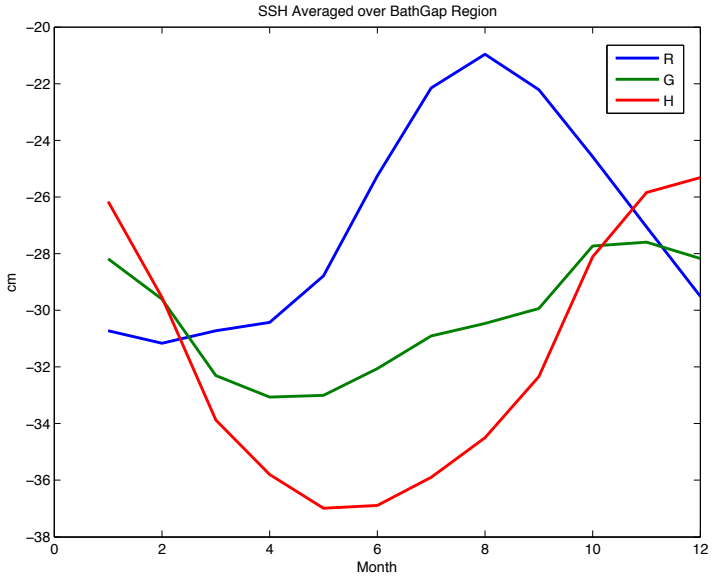


b)

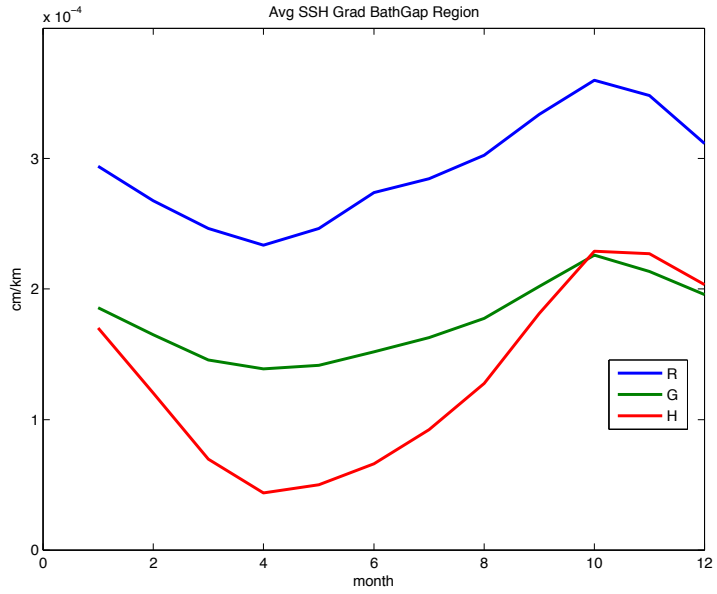


and early winter. The R-case, however, is dominated by a summer-time surge in SSH which peaks in August. The G-case, with a ~4cm total change, undergoes the smallest

annual variation between the cases. The maximum in all three cases that spans summer (R-case) through early fall is indicative of seasonal freshwater input. The R-case, which receives the highest flux of local terrestrial runoff from Greenland, produces the corresponding rise in SSH signal in late summer, earlier than the G and H-cases. Those two cases exhibit their rise in SSH all throughout the melt season, but reach their maximum in late fall/early winter. This could imply their main coastal freshwater source emanating from further upstream, rather than local runoff.

The mean annual cycle in across-shelf SSH gradient (Figure 47b) shows the same pattern in the G, H, and R-cases, with a minimum in April and a peak in October. The R-case shows a consistently stronger gradient than the G-case and H-cases. The G and H-cases produce identical values at their maximum (October), though this is still 2/3 as strong as the R-case gradient at this time. The G-case upholds SSH gradients that are 2/3 as strong as the R-case for the entire year, and the H-case shows the most shallow SSH gradient for most of the year (January through September). The steeper across-shelf gradients in the G and R-cases may be the result of local sources of freshwater that are able to accumulate in the region, whereas in the H-case, the buoyancy signal is dominated by the broad-scale SSS restoring which lacks resolution at the coastal shelves. The dominant behavior in all three cases of the SSH gradient maximum October implies an enhanced boundary current during this time. This agrees with observations showing that the maximum width and speed of the WGCS

Figure 48: The SSH gradient in the across-shelf direction averaged latitudinally for the marked region. The top panel shows the mean January, February and March values while the bottom panel is the same for July, August and September.

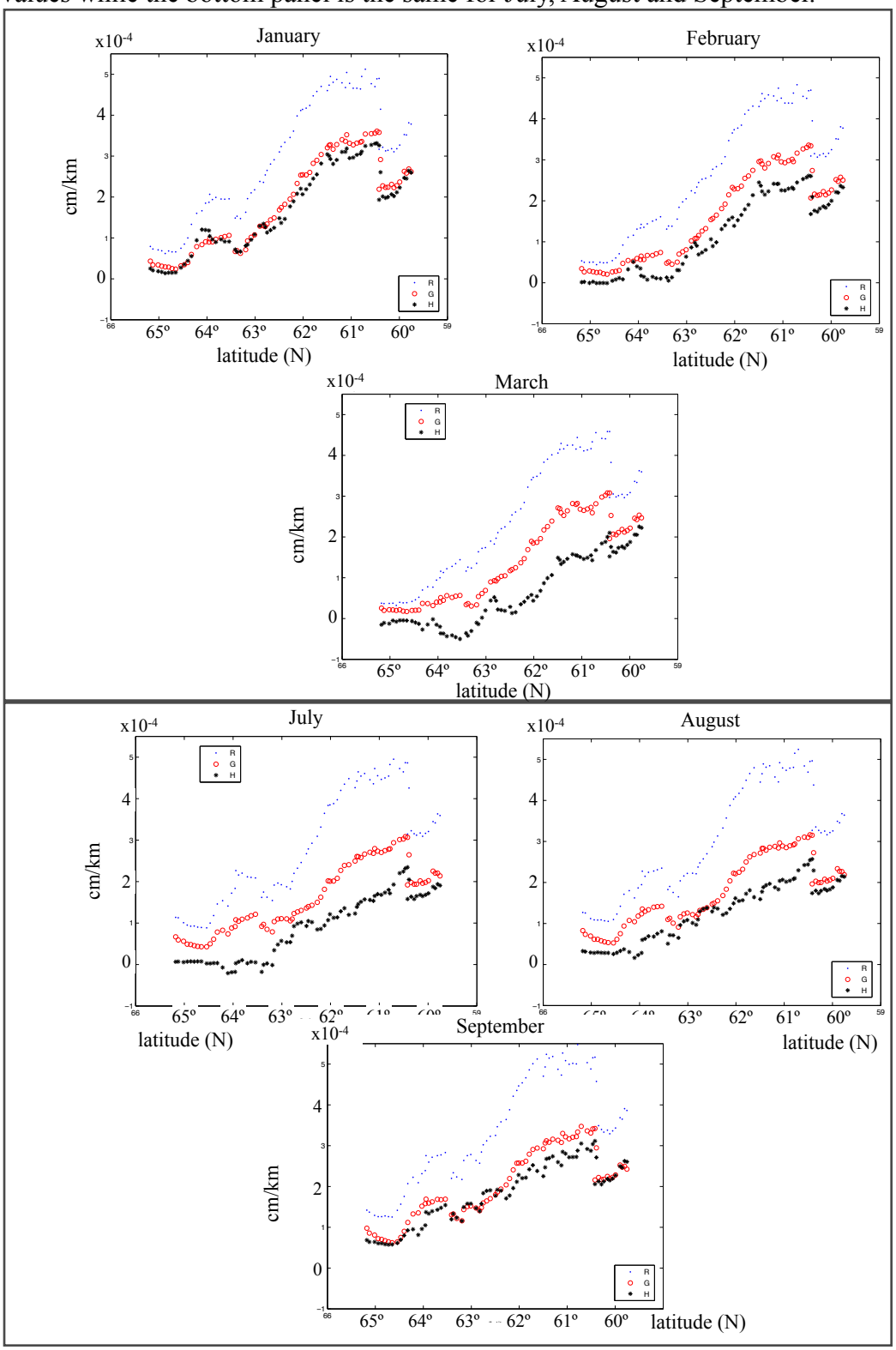

peaks in the October through December (Rykova et al., 2015). Combining these two assessments of the model results, the SSH and SSH gradients, imply that the freshwater buoyancy fluxes enhance the coastal SSH on a seasonal basis.

Next, we assess the variations in the across-shelf SSH gradient as a function of latitude, averaged for the winter and summer months in Figure 48. As expected, the G, H, and R-cases maintain their hierarchy of SSH slope throughout this region, with some overlap in magnitudes between the G and H-cases. The H-case is unique in exhibiting small fluctuations along the Greenland shelf, and it is the only model that produces a negative gradient in the higher latitudes, as seen in the March plot of Figure 48. The geographic resolution in these plots indicate that all models show a jump in the SSH gradient between 60ºN and 61ºN. This coincides with the location of Cape Desolation, which marks the beginning of the bathymetric gap and the eddy production maximum known from observations. The other main feature in the zonally averaged SSH gradients is the relative maximum in around 64ºN that occurs in all three models. This is significant because, as will be shown later, this is the location where most eddies are produced in the simulations.

## 4.3 Eddy Characteristics

Figure 49: In part A of this figure, the monthly mean salinity and velocity are shown for the three time slices in the G, H and R-cases where ICAs have been identified. A zoomed in plot surrounding the eddy is also displayed. In part B, the immediate area

a)

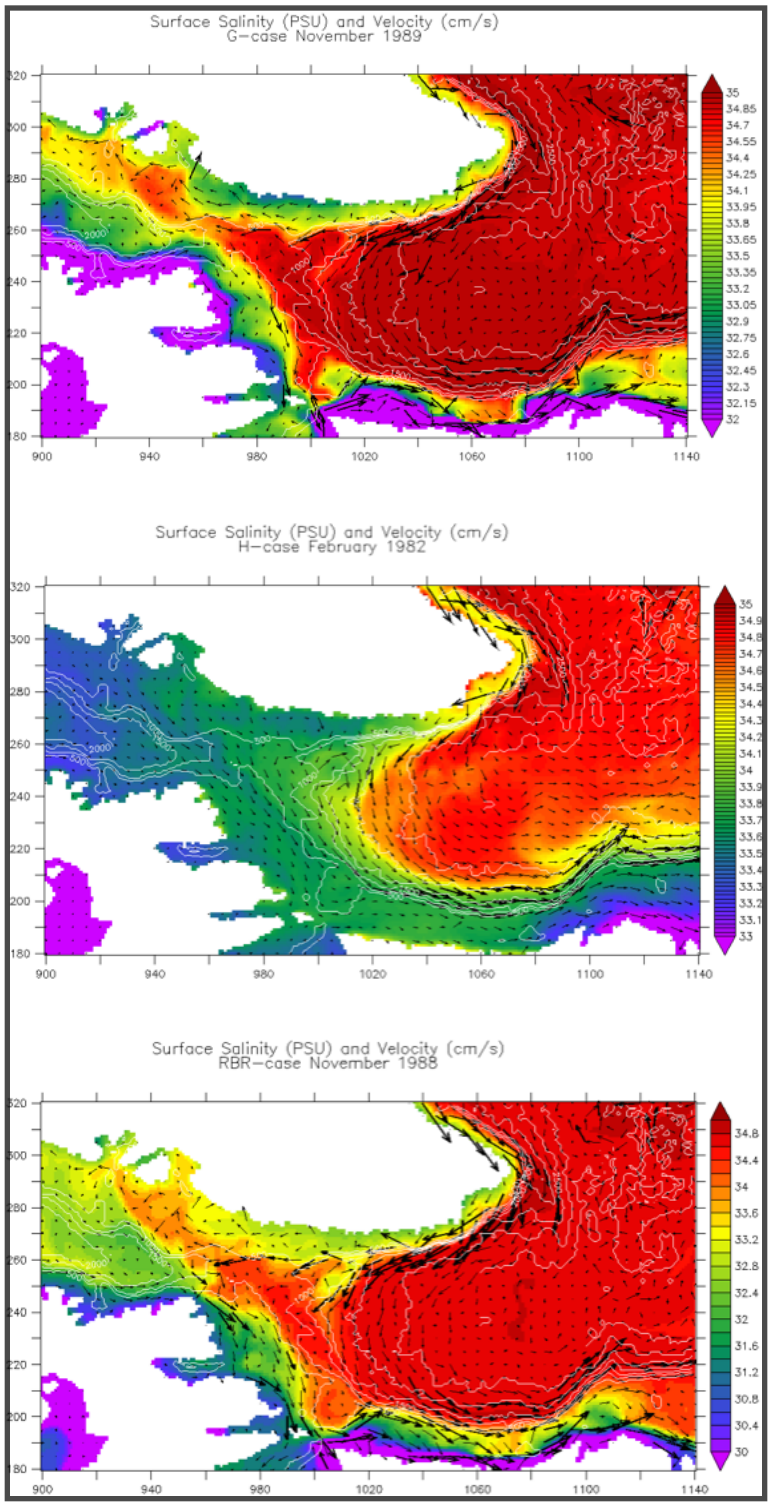

b)

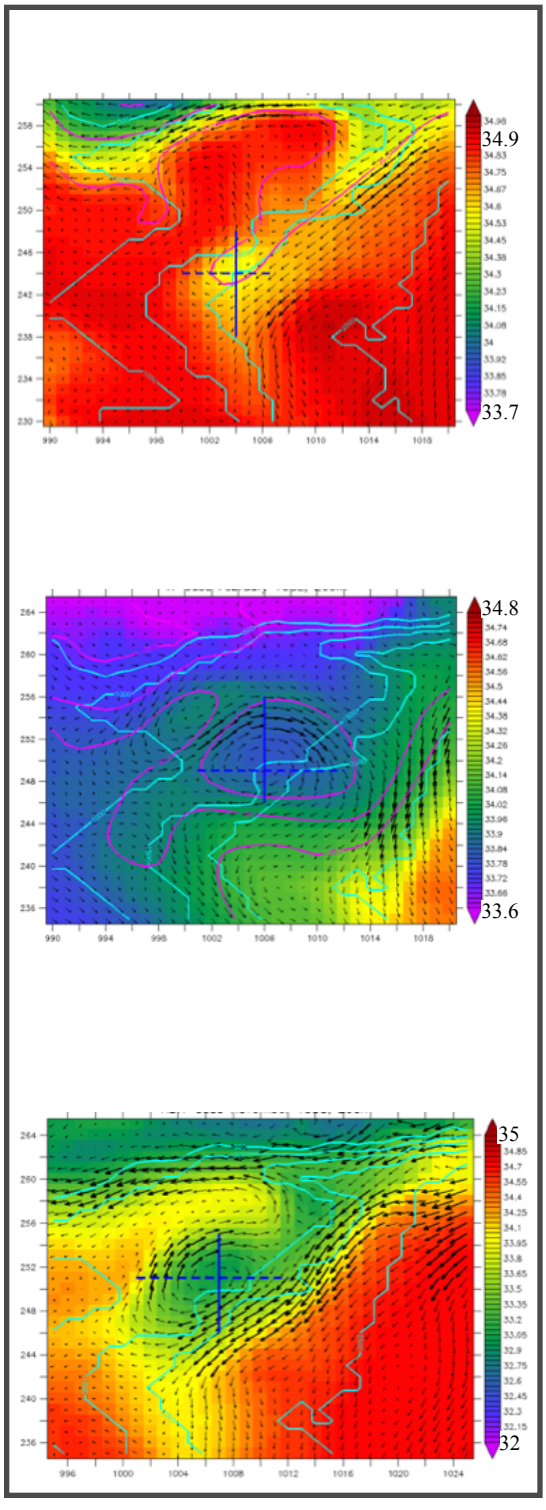

Deriving from the WGCS, the Irminger Rings, or Irminger Current Anticyclones are thought to contribute significantly to the buoyancy budget of the interior basin (Lilly et al., 2003; Straneo, 2006; Saenko et al., 2014). Because these anticyclonic eddies are able to maintain a warm core of Irminger water, their contribution to the annual heat budget of the Labrador Sea has been explored (Katsman et al., 2004; Straneo, 2006; Chanut et al., 2008). As observations have grown, the presence of fresh surface layers within these eddies has been documented, and the eddies' increased impact on Labrador Sea restratification has only recently been recognized and explored further (Hatun et al., 2007; de Jong et al., 2014; Rykova et al., 2009). This has coincided with improved assessment of freshwater in the region, showing that it plays a critical role in the ocean's buoyancy budget (Schmidt & Send, 2007; Myers et al., 2009). Moreover, insufficient freshwater in these eddies has been identified as a major shortcoming of past modeling studies that seek to represent the deep convection process of this region (McGeehan & Maslowski, 2011).

We seek to further elucidate the role of the freshwater that is carried by eddies into the interior Labrador Sea by identifying and comparing unconvected, or fresh-top Irminger Current Anticyclones (uICAs) emanating from the West Greenland Current System in the G, H and R-cases. I identified these eddies by visual inspection of the near surface (~20m depth) velocity vectors and salinity shading using plots of the mean monthly output from 1980-2009. An anticyclonic vortex in the eastern Labrador

Sea with depressed salinities compared to the surroundings is considered an uICA. The distributions of the quantities of eddies produced by the model simulations according to this method are described further here and expanded upon in the next section. The nomenclature used here follows Rykova (2010).

The R-case produces the most frequent and easily distinguishable of this type of ICA, though they have been identified in all three cases. In Figure 49a, we showcase an uICA for each case in the map-view plot of the Labrador Sea as well as in a zoomed-in plot of the eddy. In all three cases, the eddies appear in approximately the same location - in the northeastern Labrador Sea, where the 1000 and 1500m isobaths diverge from the coast of west Greenland. The eddy in the R-case has the lowest central salinity of ~33 while the G-case, with the highest, has an eddy salinity of more than 34.4. The G-case eddy also has the weakest velocity signature. Details of each respective eddy area are shown in Figure 49b, where the velocity vectors, isobaths and salinity anomalies are more clearly displayed. A residual of the eddy produced in the H-case remains in the following month, though that is one of the few instances where characteristics of an uICA last longer than a month.

Transect lines over the center of the eddies in Figure 49b depict the locations of cross sections through the surface and intermediate layer shown in Figure 50. In all three cases, the top 700m of the eddy structures show a relatively fresh surface layer and

anticyclonic velocities, but beyond that the characteristics are varied. The G-case shows a very weak surface freshwater signal and overall shows little stratification. Its velocity contours also have the least pronounced anticyclonic signal. The H-case shows a vigorous eddy reaching down to 400m. This is paired with a slowly varying

Figure 50: The vertical cross sections of salinity with velocity contours are given for the G, H and R-case eddies of the zoomed plots in the previous figure.

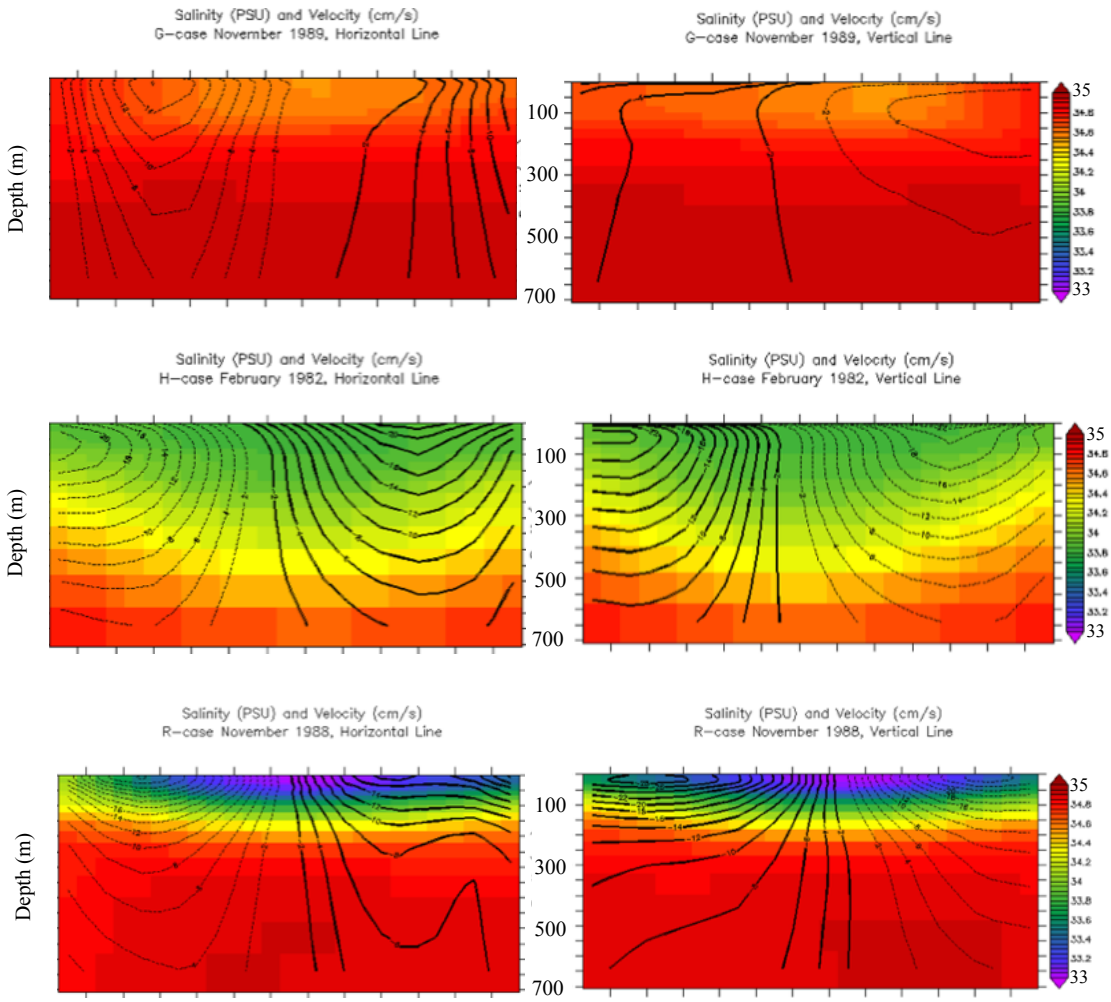

stratification and salinity down to 700m. In the R-case, the freshwater layer is sharply contained at the surface along with the strongest velocities, reaching 30 cm/s within that confined freshwater layer of the top 250-300m. Beyond that, the hydrography becomes weakly stratified and remains above the standard 34.8 reference salinity value for freshwater quantification. The surface salinity of the R-case is less than 33, which is significantly less than any other case. The eddy structure in the R-case most closely agrees with the Labrador Sea rim current characteristics, where fresh, coastal waters overlay the Irminger Current properties at intermediate depth (Rykova et al., 2015). ICAs are known to maintain this salinity structure of the boundary current system as they efficiently transport shelf properties into the interior before mixing and eroding away (Lilly et al., 2003; Hatun et al., 2007; Rykova et al., 2009).

Figure 51: An example eddy with a range of possible outlines containing the eddy. Teal lines are the model bathymetry and magenta lines indicate SSH. The shading is salinity in PSU

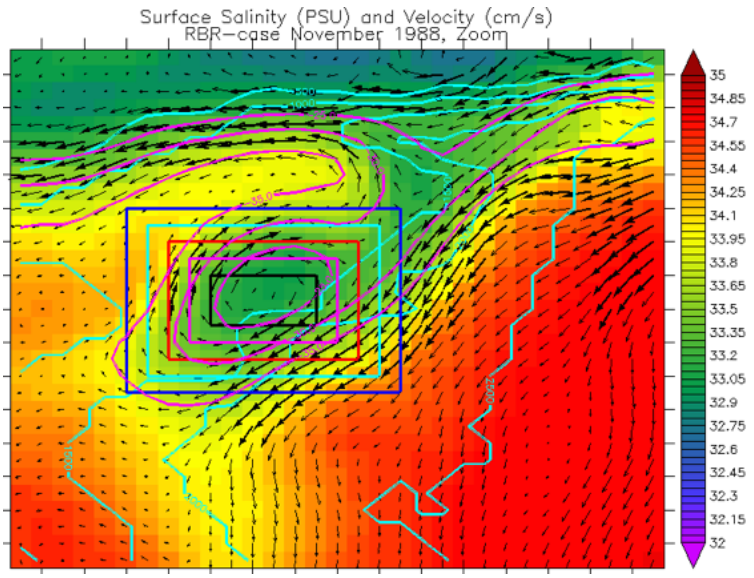

## 4.4 Eddy Census and Freshwater Quantification

We present a quantitative evaluation of the freshwater transport in uICAs for all three cases and compare the results to observational data. To quantify the freshwater contained within an uICA, we first determine the size of the eddy. We draw a number of rectangles that encompass the eddy, as determined from its map-view plot, as shown in Figure 51. We also choose a range of reference salinities to calculate the freshwater content within each of the rectangles. Varying both the reference salinity and the rectangle encompassing the eddy allows us to find the optimum size of the eddy that contains an anomalous salinity signature with respect to the ambient waters, while maximizing the freshwater content with respect to the reference salinity. The freshwater content is defined as the volume of freshwater (with salinity of 0) that must be mixed with a volume of seawater of a certain reference salinity to create the observed salinity. In other words, a fractional volume of freshwater is contained in the volume of observed seawater to produce that salinity of observed seawater relative to the reference salinity.

$$FWC = \text{sum}\left[ V_{ijk} * (S_{ref}-S_{ijk})/S_{ref} \right]$$ for the top 220m or the top 11 vertical nodes

If the volume of water has a salinity greater than the reference salinity, then it has no freshwater content, and that cell is excluded from our FWC calculation (as it contributes no freshwater to the sum). We use a series of reference salinities ($S_{ref}$) that are customized to the eddy and the range of salinities in its vicinity. Then, we calculate the freshwater content within each of the rectangular prisms, like those laid out in Figure 51.

Figure 52: The fractional volume of freshwater contained within the top 200m of the various in eddy sizes shown in Figure 51 is plotted using a range of reference salinities. The eddy diameter is calculated as the average of the two horizontal dimensions of the rectangles in Figure 51. This plot shows the sensitivity of the freshwater contained in the eddy to the eddy size for several reference salinities.

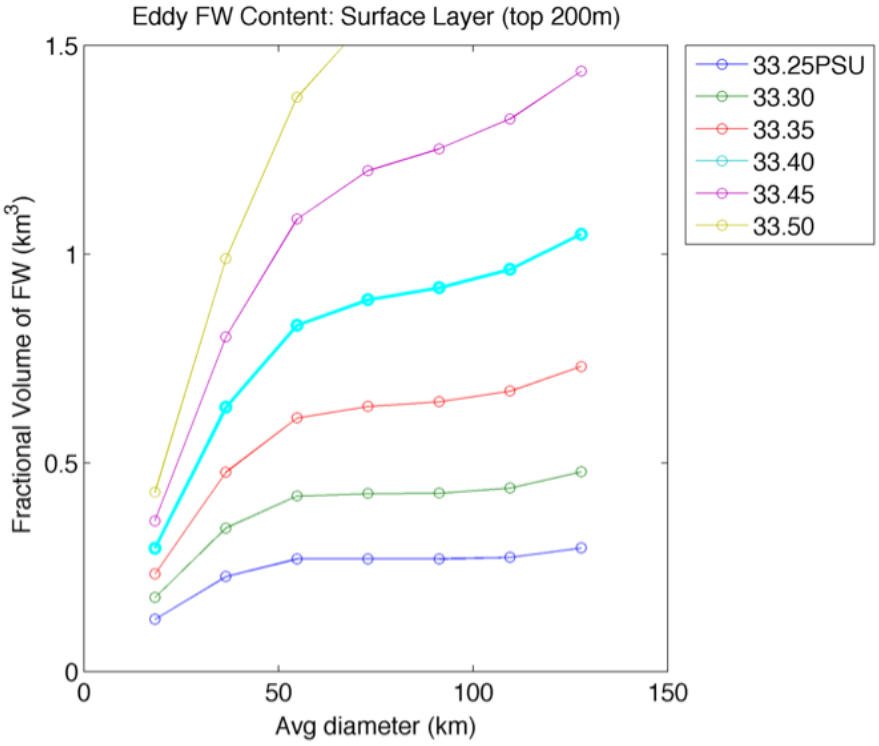

Eddy size is indicated by the diameter, which is estimated as the average distance between each of the two sides of the rectangle. The results of the spread in FWC is shown in Figure 52 for a sample eddy. It shows the sensitivity of FWC to a varying reference salinity and eddy diameter. In the cases with the lowest reference salinities, the FWC does not increase with size between 50-100km diameters. This means that the greatest salinity anomaly in the eddy compared to the ambient salinity is contained within 50-100km. With higher reference salinities, an increasing FWC is calculated due to an increasing eddy size, eventually producing a linear relationship where all grid cells have a fractional volume of freshwater associated with them. So increasing the diameter simply increases FWC by a proportional amount. This method was repeated on a handful of eddies in each of the model runs, and most of the FWC values within these eddies leveled off at an average diameter of 70km. Hence, we use this eddy diameter for all subsequent calculations of FWC within an eddy.

The other variable in the FWC calculation is the reference salinity. Typically, a value of 34.8 or 35 is used in global climate models, but other values can be used depending on the typical regional or water mass values (Holfort et al., 2008). We use two reference salinities in our eddy freshwater content quantification. The first one is the commonly used value of 34.8 so as to compare easily with other studies, and the other uses the mean salinity of the top 220m in the Labrador Sea for each of our three

model cases. This provides a way to tailor the reference salinity to a value that is representative of the unique characteristics produced in the model. Departures from this reference salinity more accurately reflect the addition of freshwater to the surface. Figure 53 shows the 1980-2009 monthly time series and values of average salinities. All three model simulations have average surface salinities that are less than 34.8 - with values of 34.5, 34.3 and 34.2 for the G, H and R-cases, respectively. The G-case has the highest mean surface salinity and the R-case has the lowest of the three simulations. These model-specific reference salinity values provide a more appropriate salinity reference for our analyses since the freshwater anomaly in each eddy should be referenced to the background salinity of each model and not only to a globally representative salinity.

Figure 53: The average salinity in the top 220m of the Labrador Sea for the entire analysis period. Average values in the G, H and R-cases are listed in the legend.

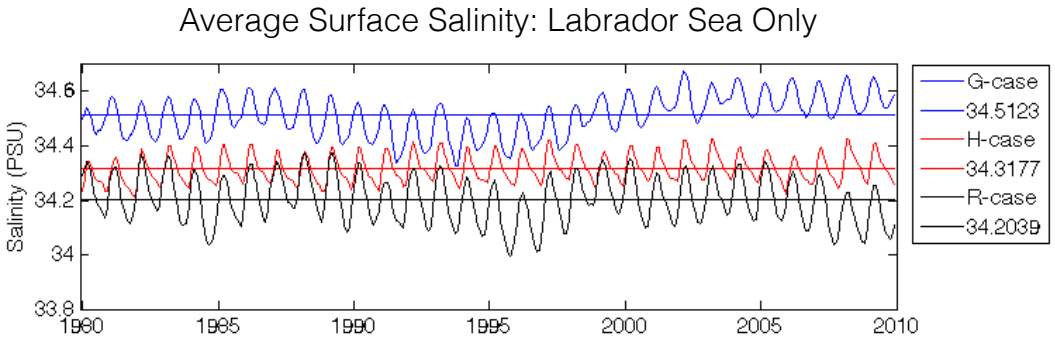

The results of the freshwater content calculations for both the standard 34.8 reference salinity and the mean surface salinity for each model are shown in Tables 2A-C for the four 70-km diameter eddies. The standard reference salinity of 34.8 results in a much larger volume of freshwater (since more grid cells contribute to the FWC calculation). The R-case eddy has the greatest freshwater content contained within it of all three models, yielding 0-40km$^3$ depending on eddy size and whether we use the local or global salinity reference. In general, using the global salinity reference produces a factor of 2-4 greater volume of freshwater per eddy (25-40km$^3$ versus 6-18km$^3$). The G-case has the lowest freshwater content, with up to 5km$^3$ for the standard reference salinity, and essentially zero with respect to its mean surface salinity. The H-case produces an eddy that contains a freshwater volume within the upper range of the R-case (33km$^3$ using the global salinity reference), but in most instances it contains less freshwater than the R-case (1-10km$^3$). With respect to the mean surface salinity for the H-case, the FWC is very low, producing at most ~2km$^3$. This is indicative of the overall low salinity state that the H-case maintains.

Irminger Current Anticyclones - whether convected or unconvected - are difficult to observe and only recently studies have focused on their properties and characteristics. The first uICAs with cold and fresh surfaces were documented with salinities of ~34.3 and temperatures that were 0.05 to 0.1 deg C cooler than ambient waters (Hatun, 2007; Lilly & Rhines, 2002). Their sizes are estimated to be 15-50km in

Table 2: The freshwater volume contained within each eddy with an estimated diameter of 70 km. The freshwater volume is referenced to the standard salinity of 34.8 and the mean surface salinity of 34.51, 34.32, and 34.20 for the G, H and R-cases respectively.

| R-case Eddies | FW Vol (km3) with Sref=34.8, D=70 | FW Vol (km3) with Sref=34.20, D=70 |
|---|---|---|
| 1988-11 | 30 | 10 |
| 1993-10 | 25 | 6 |
| 1994-10 | 28 | 7 |
| 1994-12 | 40 | 18 |
| 1998-03 | 8 | 0 |
| **G-case Eddies** | **FW Vol (km3) with Sref=34.8,D=70** | **FW Vol (km3) with Sref=34.51, D=70** |
| 1983-10 (1,2) | 6e-4,5.2 | 0,0.2 |
| 1989-11 | 3 | 0 |
| 1990-06 | 0.2 | 0 |
| 2001-03 | 0 | 0 |
| **H-case Eddies** | **FW Vol (km3) with Sref=34.8, D=70** | **FW Vol (km3) with Sref=34.32, D=70** |
| 1982-02 | 33 | 15 |
| 1985-04 | 10 | 1.5 |
| 1995-05 | 10 | 1 |
| 2002-02 | 1.1 | 0 |

diameter (Katsman & Spall, 2004; Kawasaki & Hasumi, 2014). Consensus on the frequency of ICA production in general is premature due to a shortage of studies, but

ranges vary from 2-3 per year to almost a dozen per year (Lilly & Rhines, 2002; de Jong et al., 2014; Katsman & Spall, 2004). ICAs are most commonly produced in the winter when the seasonal EKE maximum occurs (Brandt et al., 2004).

Using the method described at the beginning of section 4.3, I recorded the month and year that each eddy was identified in each of the three model simulations. The G, H and R-cases do not have a consistent pattern of uICA production among the cases nor with observations. In total, the R-case creates at least four times as many uICAs as the G and H-cases during the thirty year analysis period. The G and H-cases produce approximately equivalent numbers of ICAs. Figure 54 shows the count of the number of months per year that at least a single uICA was identified. The R-case has a near-steady production of uICAs, whereas the G and H-cases produce at most several per year. The seasonal distribution of uICAs varies within each model as well, as shown in Figure 55. There are fewer uICAs in the R-case in the late winter, whereas the H-case shows a maximum during this time and into the spring. The G-case has a slight maximum in the late spring or early summer period. The observations point towards fewer fresh-top ICAs during the winter because of the strong buoyancy loss during this period. The R-case may be representing this tendency for convection disrupting the signature freshwater signal of the uICAs. The low counts of the G-case during the summer period may be due to insufficient freshwater.

Figure 54: A tally of the number of months per year that produced at least one ICA in all three model simulations. The R-case surpassed the G and H-cases with a total of 206 months with uICA appearances during the 360 months between 1980 and 2009. The G and H-cases reached appearance counts of 52 and 60 months respectively.

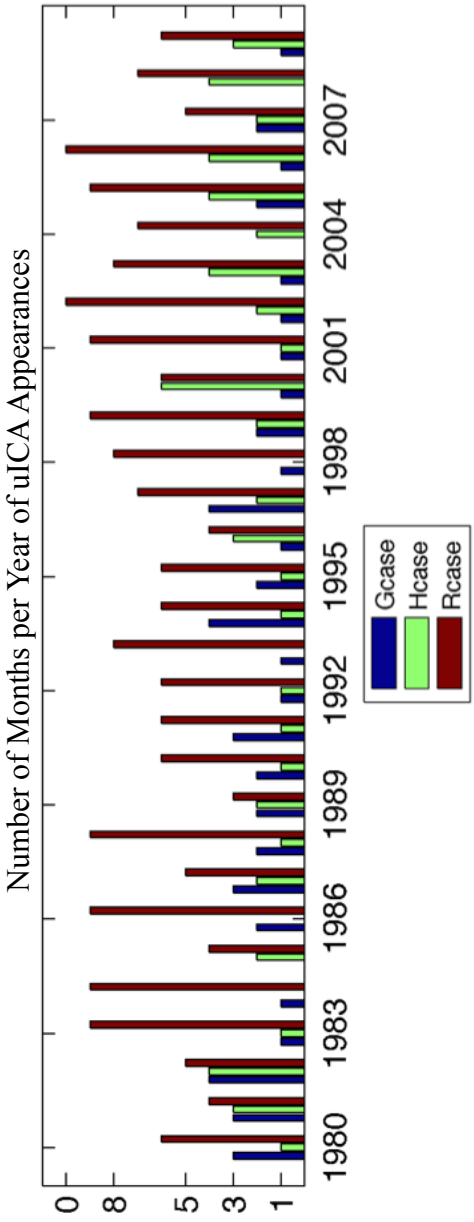

Figure 55: The number of uICA appearances per month over the 30 year simulation period. The G and H-cases have similar seasonal distributions with maximum uICA production during the restratification season. The R-case also begins to increase its production during spring and summer, and has a minimum during the late winter, in agreement with observations.

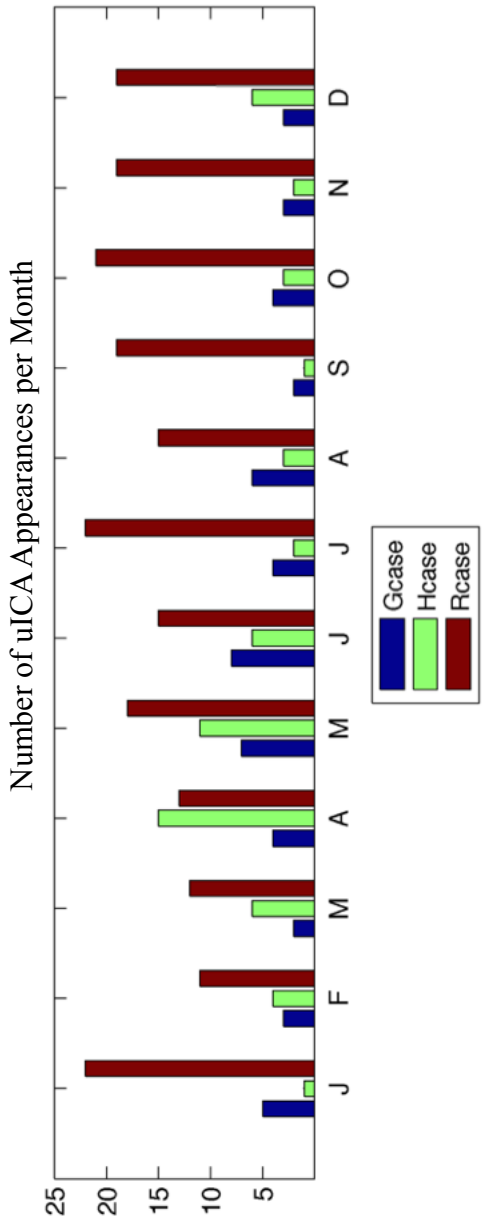

## 4.5 FWC and MLD Correlations

To quantify the ability of the G, H and R-case to transport freshwater into the interior Labrador Sea via the uICAs we calculate the correlation between the freshwater content and the mixed layer depth at each grid point. The freshwater content (FWC) is calculated in the same way as explained in the previous section, and we use a standard reference salinity of 34.8. In Figure 56 we display the Pearson's correlation coefficient at each grid cell with significance values in the 95% confidence range. No lags are introduced, assuming vertical mixing at a local grid point due to a freshwater flux occurs within a monthly time period. We continue to display and evaluate all three MLD methods because no single method produced optimum results, as evaluated in the previous section. As the FWC increases especially in the surface, the mixed layer depth should decrease because of an introduction of a buoyancy layer that causes the water column stratification to strengthen, and mixing to weaken, resulting in the pycnocline moving upward or being reset. This creates a negative correlation between FWC and MLD in deep parts of the ocean and is what we expect to be physically realistic. Thus, the realism of each model simulation can be assessed by the strength and extent of such a negative correlation. However, the opposite can occur if there is not a strong halocline near the surface. If the FWC is more uniformly distributed through depth, then that water mass may help to extend the mixed layer depth especially if the water column is already shallow and fresh. This is likely

Figure 56: Pearson's correlation coefficients in the 95% confidence range for FWC and MLD. This quantifies how strongly freshwater flux to the interior Labrador Sea affects MLD and deep convection.

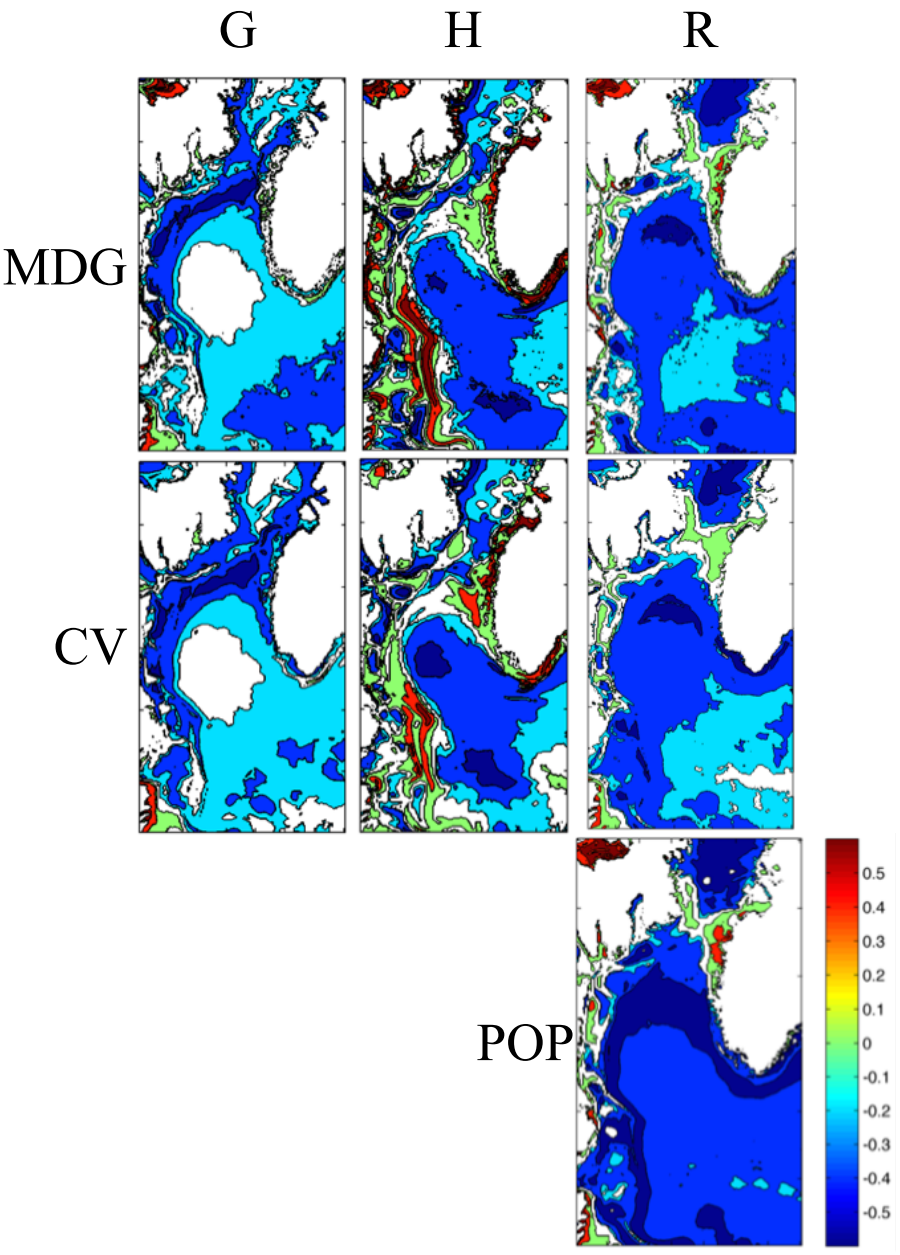

occurring in the strong positive correlations, predominantly along Labrador shelf in the H-case plots below.

Each of the model cases has a different spatial distribution and magnitude of correlation coefficients. Between the G and H-cases, the major difference is that the G-case shows insignificant correlations in the central Labrador Sea, whereas the H-case shows a significant negative relationship throughout this entire region. The H-case, however, shows a positive correlation along the shelf of west Greenland and Labrador where the G-case exhibits some of its most negative correlations. This is due to the vertical distribution of freshwater in these shallow areas. The G-case is in an overall higher salinity state due to its reduced freshwater forcing compared to the SSS restoring that the H-case receives. This can be causing the dearth of correlations in the central basin of the G-case as well as the negative relationship in the H-case.

The R-case seems to be a combination of both the G and H-cases. There are significant negative correlations throughout the Labrador Sea. Some of its strongest correlations are along the west Greenland slope, the recirculation pathway, and also near and seaward of the Hamilton Bank on the Labrador side. In the central part of the Labrador Sea, there are small but negative correlations between the MLD and FWC. There are some regions that show insignificant correlation, mostly along the Labrador shelf and other shallow regions south of Baffin Bay. Like the H-case, the R-

case shows some strong positive values near the eastern side of Davis Strait. This may be due to the low stratification of the shallow shelf region so that the freshwater flux affects the entire water column, not just a buoyant surface layer.

The main cyclonic gyre circulation contains buoyant surface waters that should exhibit strong negative correlations. From these strong boundary currents, fresh-top eddies are shed and can contribute to disrupting the deepening MLD in the interior Labrador Sea, especially on the eastern side. This is one rapid mechanism that replenishes buoyancy in the Labrador Sea after winter-time buoyancy loss related to the movement of cold air masses eastward from the land masses of Labrador and Baffin Island. Each of the model simulations represent this physically expected relationship to differing levels. The negative correlations in the boundary currents are well represented in the G and R-cases but are lacking in the H-case. The interior Labrador Sea exhibits signs of the freshwater impacting deep convection in the H and R-cases. This analysis shows that the R-case is best able to produce realistic freshwater and MLD relationships throughout the Labrador Sea.

# Chapter 5: Discussion and Conclusions

In this study we show and analyze results from three RASM simulations that differ in their treatment of freshwater forcing. The G-case and H-case are identical ice-ocean coupled simulations except in the G-case, the sea surface salinity restoring is removed and freshwater is supplied along the coasts as land runoff. The R-case is a fully coupled simulation, where the atmosphere, land, sea ice and ocean models are actively coupled and this case employs lateral boundary conditions for the ocean (POP) and atmospheric (WRF) models as well as spectral nudging applied to the upper half of the atmosphere in WRF. The G, H, and R-cases all simulate the large scale, topography-driven Labrador Sea dynamics of a cyclonic flow surrounding weakly stratified interior basin waters. However upon closer inspection, one key difference among them is that the G and R-cases produce buoyancy currents along the coast of Greenland and Labrador that do not exist or are weaker in the H-case.

The differences in the West Greenland Current System stem from the salinity and buoyancy distribution in the Labrador Sea, which are affected by the freshwater sources in each of the models. The G and R-cases allow freshwater to enter in the coastal regions from the land model, which reinforces the coastal hydrography with a corresponding SSH signal at the surface and a frontal structure at depth. The H-case, however, with its more classical ocean model set-up, receives a monthly-mean flux of

water via the restoring of surface salinity to monthly-mean climatology that by definition represents rather coarse and smooth distribution of water properties and resulting coast-to-interior gradients. It does not capture the narrow coastal stretch of low salinity overlying the continental shelves as seen in the G and R -cases, which within the accuracy of model spatial resolution mimic the natural system of runoff entering the ocean. Thus, the G and R-cases are able to create a stronger boundary current and attempt to produce a coastal buoyancy current along the coast. We refrain from labeling this as a coastal current because there has been no observations of such a flow and our model resolution may not permit the flow given the narrow Rossby radii in the shelf region (Bacon et al., 2008).

The coastal hydrographic properties near west Greenland support increased current speeds along the WGCS and the shelf. In the G and R-cases, fluid dynamics governing the ocean model are able to concentrate higher SSH and fresh coastal properties along the coast. These two factors enhance the boundary current speed by creating a sharper frontal structure or isopycnal gradient as well as by geostrophic balance (Myers et al., 2009; Rykova et al., 2015). This results in the stronger G and R-case WGCS that penetrates further northward than in the H-case. This also has a secondary effect by bringing in more heat that is able to reduce the sea ice extent along the eastern side of the Labrador Sea. The stronger flow is more prone to instabilities and generating eddies (Chanut et al., 2008; Straneo, 2006; Spall, 2004).

The reliance on model physics in the G and R-cases rather than parameterizations when subjected to these coastal conditions yields more realistic simulations.

To further explore possible causes of the difference in the coastal hydrography and current structure, we analyze the local Greenland freshwater sources, which differ greatly between the G and R-cases and are susceptible to future change. The G-case prescribes a significantly lower total runoff flux from Greenland, which is derived from the COREv2 data set. It is an order of magnitude less than the observational estimates (Bamber et al., 2012) and the surface Greenland runoff simulated by the RASM RVIC scheme in the R-case. Freshwater along the coast of Greenland in the G-case is most prevalent during the summer and fades away in the spring after the winter. The R-case, however, maintains its coastal wedge of freshwater throughout the year along the west coast of Greenland. The differences in the local flux of freshwater coming from Greenland are responsible for the stark difference in coastal salinity between the three model cases. Figure 57 shows this as well as the sharp gradient in across-shelf salinity in the G and R-cases compared to the H-case, which follows the smooth PHC field.

Despite the shortcomings of the PHC data, we use it to compare the mean monthly surface temperature and salinity of all three models against a single standard in Figures 18-19, Chapter 2. These comparisons indicate that the G and R-cases behave

Figure 57: August and January all-time mean salinity conditions at 7.5 m depth. The sharp salinity gradient from the coast of Greenland to the interior Labrador Sea is similar in the G and R-cases. Both cases are able to maintain a fresh signal along the shelves in both summer and winter, whereas the H-case salinity is more smoothly varying across the Labrador Sea.

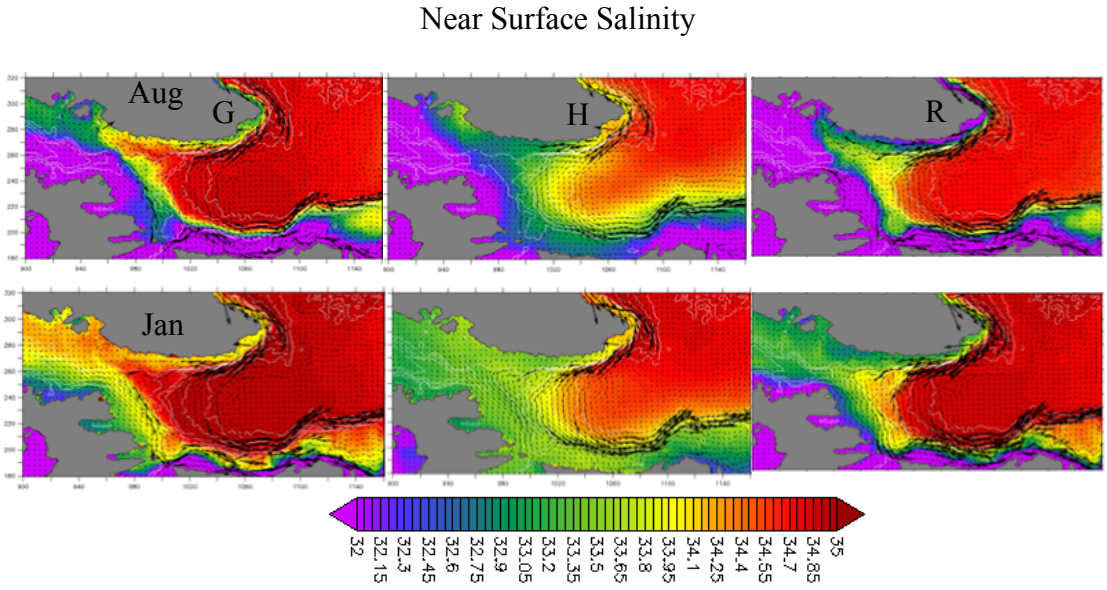


similarly, though the G-case tends to have greater magnitudes of bias with respect to the PHC. For example, both the G and R-cases tend to show a more saline recirculation path at the northern side of the Labrador basin, but the G-case is 1 unit of salinity greater than the R-case in this region (which is also 1 unit greater than the PHC data set). The winter-time coastal temperatures are cooler along the coast and warmer offshore in both the G and R-cases than the PHC. These biases in the temperature pattern are due to the representation of the WGCS in the G and R-cases. The surface component of the current system has Arctic-origin waters, whereas the interior waters has been modified due to mixing and transport. The R-case agrees best

with PHC surface temperature during the summer out of all three models, which is fitting because the PHC has a summertime bias of warm and fresh conditions.

The distinctions in the vertical variation of velocity and water properties between all three cases provide further insight into the merits of each freshwater forcing method. The cross sections of salinity with velocity contours along the MGE transect line, as shown in Chapter 2, provide details on the boundary current structure and dynamics, which through eddy generating instabilities within the WGCS exchanges some coastal and shelf waters with the interior Labrador Sea. The G-case lacks a significant interior freshwater cap throughout most of the year and in all years. During peak runoff season (JJA), the shallow coastal areas saturate with relatively fresh water compared to the interior. There is a strong freshwater cap presence in the H-case that has a weak shelf-to-interior gradient, indicative of the smooth SSS fields used for restoring, as previously mentioned. The R-case has a significant freshwater signal along the coast. This contributes to the seasonal restratification cylce and freshwater cap in the interior Labrador Sea.

In all three cases the boundary current speed increases in late summer. The stronger flow of the WGCS in the R-case of the three cases most closely resembles the observations, where measured speeds vary between 35 cm/s and 90 cm/s (Cuny et al., 2002; Rykova et al., 2015). Current depths in the G and H-cases reach 500-600m and

are more vertically constrained in the R-case, whereas observations indicate boundary current velocities of the Irminger water reach down to 1000m in the WGCS (Houghton & Visbeck, 2002; Cuny et al., 2002). However, the R-case is more conducive to the production of unconvected Irminger Current Anticyclones (uICAs, anticyclonic eddies with fresh and cold surface waters) because its velocity and corresponding hydrographic gradient is sharper under the more confined conditions. This leads to more instabilities and exchange across the continental slope of waters from the shelf with those from the interior, which can impact deep convection. The local Greenland runoff flux, which in the R-case amounts to a non-negligible and realistic freshwater flux, promotes the stronger coastal current and sharper frontal structure, which have important repercussions for the distribution of deep ocean convection in the interior Labrador Sea.

The WGCS, including its structure and variability, is crucial for the region because it provides a conduit for rapid spring-time restratification of the interior Labrador Sea, and because of its possible role in directly inhibiting winter-time deep convection due to continued eddy generation and resulting shelf-basin exchange. The eddy activity is greatly enhanced in the R-case compared to the other simulations. The number of uICAs produced in the R-case is about 4 times that of the G and H-cases. The G and H-case show a slight seasonal cycle, with peak production in the summer and spring respectively. The R-case has the least pronounced seasonal cycle, but shows a

minimum production rate in the winter. This is reasonable despite the winter-time maximum in EKE since the general IRs or ICAs are subject to winter-time buoyancy loss, which can affect their fresh-top signature.

A measure of the total eddy activity in the Labrador Sea is given by the eddy kinetic energy. I calculate maps of this field based on the monthly mean velocities, which are available for the H and G-cases and which underestimate the EKE estimated from higher frequency model output. By applying an 85% correction (Maslowski et al., 2008), one can show that the H and R-cases might be producing eddy activity comparable to observations, at least along the critical bathymetry gap region, but the G-case is ~100 $cm^2/s^2$ too small at its peak (Cuny et al., 2002). Altimetry and drifter buoys show a winter-time maximum in the EKE which is reproduced using the R-case daily mean velocity output. In addition to the frontal structure along the shelf break from the WGCS, another direct effect of freshwater on the eddy activity is associated with the SSH signal. During the summer-time, when freshwater transport along the coast is at maximum, the across-shelf SSH gradient also reaches the maximum in all three cases. However, the G and H-case show a much smaller signal compared to the R-case, which is due to the realistic and non-negligible magnitude of the Greenland runoff in the latter simulation. These effects of the freshwater on the WGCS make it more prone to instabilities and eddy production (Katsman et al., 2004; Myers et al., 2009; Rykova et al., 2015).

The hydrography within the interior Labrador Sea remains challenging to simulate realistically. In the G, H and R-cases, the monthly mean winter MLDs show an unrealistically widespread and frequent deep convection pattern. At least 15% of the interior Labrador Sea cells reach winter-time MLDs greater than 2000m for over a 10 year period (1983-1996) in the H-case. For the G and R-cases, it is at least 25%. The regularity of sustained deep convection seen here and by the monthly mean plots (Figure 28) is not supported by published observations. Instead, such levels of deep convection have been inferred during 1987-1994, but since then mixed layer depth have reached at most 1600m with most years producing MLDs around 1000m (Yashayaev & Loder, 2009; Lavender et al., 2002). Too deep MLD and strong convection signals are known problems in similar regional models of the Labrador Sea (e.g. Kawasaki & Hasumi, 2014).

Our exploration of a variety of definitions for MLD calculations did not yield much improvement on that known problem nor a consensus among the methods. The three MLD definitions analyzed are: (1) the commonly used threshold method (CV), (2) a physically based maximum density gradient method (MDG), and (3) a method implemented by the developers of POP based on a density gradient (POP). The MDG method produced the lowest monthly mean values. Although these values were still higher than what observations would suggest, they were drastically (over 1200m)

Figure 58: (a) Bathymetry (m) of the Labrador Sea depicting the location of the salinities profiles used in the next section (b) The evolution salinity properties at depth are shown below. Each simulation produces a unique water mass characteristic and formation rate.

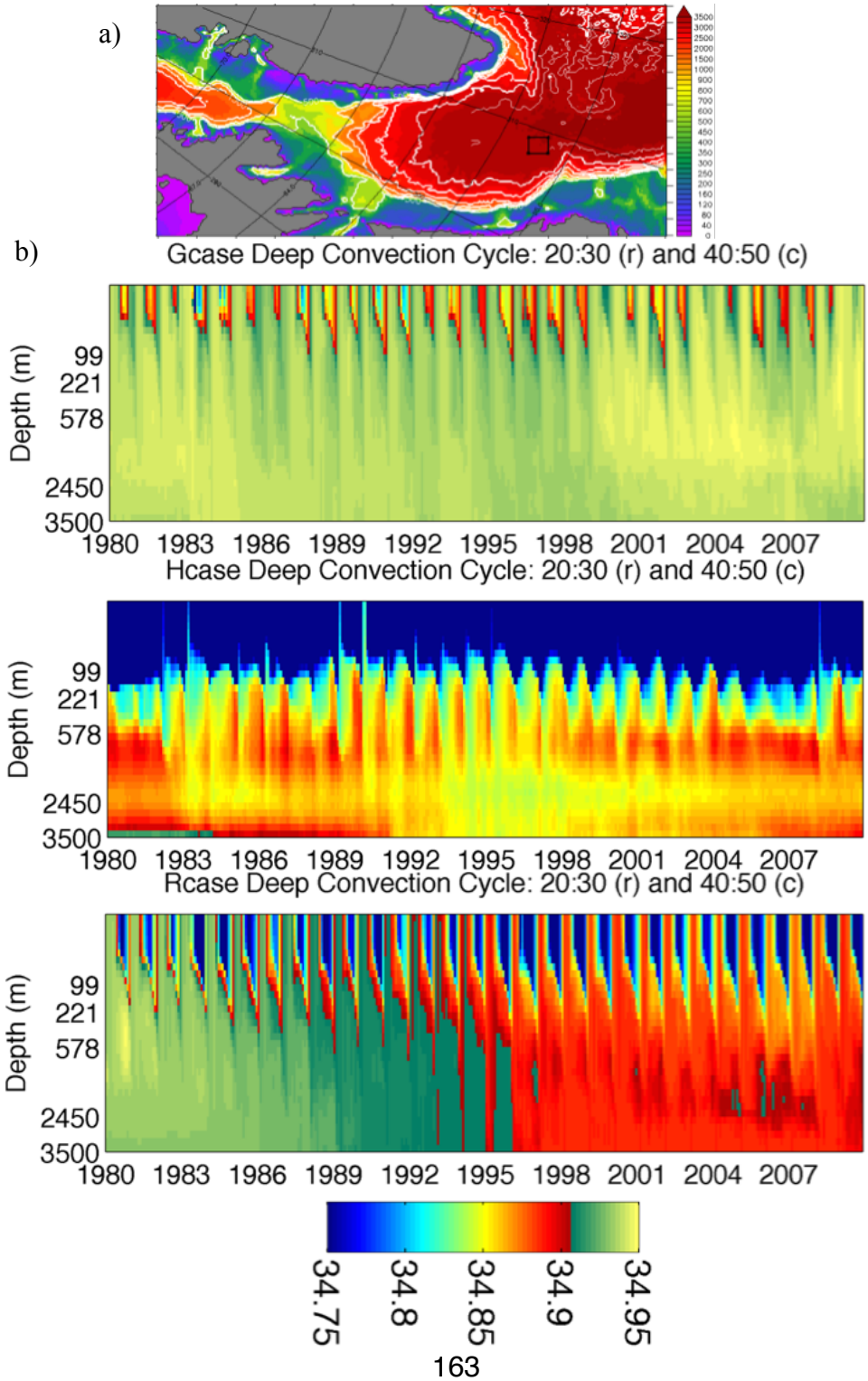

lower than the deepest MLDs defined by CV and even POP methods. By analyzing the potential density profiles in the interior basin, we observe that the density structure tends to become so weakly stratified that the greatest difference is only a little more than 0.002 kg/m$^3$, or that there is essentially no stratification. This indicates the difficulty that all methods face to discern a MLD in the interior basin and point to a major shortcoming in the model simulations that produce such weakly stratified water properties.

After examining the limitations of different MLD calculations, I analyzed the ability of the model to form deep or intermediate water masses in the Labrador Sea. We compare the hydrography in the critical region where deep Labrador Sea Water is known to form, and where each of the cases correctly produce the deepest MLDs. This region is shown in the box in Figure 58. To understand how the vertical salinity structure changes during the 30-year analysis period, I average the salinity of all grid cells in the box to produce one average salinity profile. Then, I compile the profiles for each monthly snapshot and plot the results in the depth vs. time plot of Figure 58.

The vertical variation of salinity through time in Figure 58 spans a unique range in each of the cases. The G-case undergoes a small variation in salinity throughout the entire water column, but the intermediate to deep water conditions evolve from a more saline state in the early 1980s to a slightly fresher state, before returning to the

more saline state in the early 2000s. The R-case is in a slightly more fresh regime, and its biggest signal is a steady decline in salinity at depth through the mid ‘90s, which then stabilizes throughout the rest of the simulation. It produces an annual freshwater cap that penetrates deeper than the the G-case, but not as deep as the H-case, which has a freshwater cap that exists all year. The H-case shows the strongest variation in the salinity through depth, mimicking distinct water masses and has a pronounced, multi-year freshwater signal that appears in the deep layers in the mid ‘90s. Throughout the 30-year period, there are a handful of times that a fully convected patch appears, where homogenized waters penetrate through the freshwater cap. Similarly, in the G-case there is an irregular variability in the penetration depth of the surface freshwater forcing. These characteristics are indicative of the non linear response of the convection process to the atmospheric and oceanic forcings that act on multiple timescales (Moore et al., 2015). Those forcings result in the current understanding of deep convection where multi-year phases create water masses of unique characteristics and depth (Yashayaev, 2007).

The interdecadal appearance of a particular water mass as well as an intermittent deep convection signal of the H-case show a more realistic behavior in this region of the Labrador Sea (Straneo, 2006; Yashayaev, 2007). This result is corroborated by the snapshots of hydrography along the AR7W line during 1996/1997 and 2007-2008 (Yashayaev & Loder, 2009; Pickart et al., 2002) in our analysis in Chapter 3, where

the H-case exhibits a more stratified interior water structure. In our time series of the salinity at a deep convection location in Figure 58, the R-case, however, shows more similarity to the H-case than the G-case. First, its salinity spans an overlapping range as the H-case. Secondly, its growing freshwater cap throughout the year is spans a 200m vertical range, which is closer to the H-case than the G-case and close to the 300m freshwater cap estimated by observations (Houghton & Visbeck, 2002). Finally, the two periods mentioned earlier (the first phase showing decreasing salinities and the second showing a more stable salinity at depth) is not that far from the inter-decadal phases defined by some observational studies (Pickart et al., 2002; Yashayaev, 2007). The R-case, with its reliance on model physics to distribute freshwater from the coast to the interior and to set the interior stratification of the Labrador Sea, is showing the utility of a fully coupled model. The H-case, with its classical SSS restoration method, is only useful for hindcast simulations. Any predictive study can not rely on future SSS restoring values, so improvement and development of more realistic simulations where ocean dynamics bring freshwater from the coast into the Labrador Sea through eddies are imperative.

To understand how the freshwater is distributed across the Labrador Sea in the models and how this could affect the MLD, we calculate the Pearson's R value - the linear correlation coefficient between the MLD and FWC - at a 95% confidence level. This method yields a measurement displaying the strength of the relationship between

the two variables at each cell for the 30-year simulation period with monthly frequency. When the freshwater content is referenced to 34.8, the R-case shows the most widespread negative correlation coefficients and the strongest such correlation along the cyclonic gyre circulation which is the major and most direct freshwater pathway in the Labrador Sea. This shows that the R-case has the most realistic relationship between freshwater fluxes entering each cell and MLD. Although this measurement does not isolate the freshwater signal from the eddies, the spatial distribution in the R-case is continuous and negative within the interior Labrador Sea and along the boundaries. Along the recirculation path and along the WGCS, especially near Cape Desolation, there is a strengthened signal that stretches towards the interior. This may be due to mixing and eddy formation from the major freshwater sources for the Labrador Sea (Schmidt & Send, 2007). The H-case has a strong interior basin FWC-MLD signal, but the boundary currents have either no signal or a positive signal, which we interpret as areas where the freshwater is not concentrated enough in the surface to disrupt a deepening MLD. Finally, in the G-case, there is no significant signal in the interior. This means that the freshwater does not have a strong relationship to the MLD in the central Labrador Sea, which implies that the deep convection process is not dependent on freshwater there. These differences prove that the R-case has the most realistic dynamics and the freshwater in the system is actively affecting the MLD in the central Labrador Sea.

The model configurations and forcings for the G, H and R-cases ensure that the dynamics of the Labrador Sea could be represented. The sudden and steep bathymetry along the southwest coast of Greenland is sufficiently captured by the model to trigger instabilities along the WGCS (Wolfe & Cenedese, 2006). The horizontal resolution is high enough so that RASM is eddy-permitting but not eddy-resolving in the interior Labrador Sea. Higher special resolution is one area where further improvements in modeling the Labrador Sea could be made, especially in the R-case type simulations. The current efforts by the RASM team to increase the model resolution to $1/48^{o}$ (or to ~2.4km) allow resolving the lengthscale of a typical ICA eddy hence potentially offer additional improvements but may not solve the problem entirely. The Rossby radius of deformation ($L_{def}$) changes from the coast to interior since it is affected by stratification and water depth. Therefore, along the coasts or even over the slope where critical dynamics develop, stratification is still high, hence eddy activity is locally more damped. Such details require further consideration as they are often overlooked when arguing for the spatial resolution necessary to resolve mesoscale eddies in a region.

The Labrador Sea is a climatically and globally significant region where both Arctic and sub-tropical dynamics merge. This complex area has been the focus of interdisciplinary studies because of the confluence of ocean, sea ice, atmosphere, and

glacial dynamics there (Moore et al., 2014; Zhu et al., 2014). A multidecadal trend in decreasing salinity across the North Atlantic has led to speculation on the longevity of the Atlantic Meridional Overturning Circulation (AMOC) in a warming world (Curry and Mauritzen 2005). Although some observations show a weakening and slowdown in AMOC corresponding to freshwater anomalies, models remain inconclusive on the nature of the sensitivity of AMOC to freshwater inputs (Rahmstorf, 2015; den Toom et al., 2013; Weijier et al., 2012). However, significant progress has been made in modeling studies to accurately simulate the ocean state, which provides a clearer understanding of the processes controlling AMOC. In the Labrador Sea, high resolution and a realistic freshwater treatment have been shown to critically impact the modeled state (e.g Luo et al., 2016; Grist et al., 2014) so that the role and sensitivity of AMOC in the climate can be studied more adequately. In this study, we provide additional details on the representation of freshwater sources and their impacts on the coastal ocean dynamics, mesoscale eddy activity, shelf-basin interaction and deep open ocean convection, which should help future studies of ocean and climate variability and change in this important region.

References


1. Aagaard, K. and Carmack, E. (1989). The role of sea ice and other fresh water in the Arctic circulation. *Journal of Geophysical Research,* 94(C10), 14485–14498.
2. Allison, I., Alley, R.B., Fricker, H. A., Thomas, R. H. and Warner, R. C. (2009). Ice sheet mass balance and sea level. *Antarctic Science,* 21(5), 413–426.
3. Bacon, S., Myers, P.G., Rudels, B. and Sutherland, D. A. (2008). Accessing the Inaccessible: Buoyancy-Driven Coastal Currents on the Shelves of Greenland and Eastern Canada. In Robert R. Dickson, Jens Meincke, and Peter Rhines (Eds.), *Arctic-Subarctic Ocean Fluxes: Defining the Role of the Northern Seas in Climate*, (pp. 703-722). Springer.
4. Bamber, J., van den Broeke, M., Janneke, E., Lenaerts, J. and Rignot, E. (2012). Recent large increases in freshwater fluxes from Greenland into the North Atlantic. *Geophysical Research Letters,* 39(L19501).
5. Boning, C. W., Behrens, E., Biastoch, A., Getzlaff, K. and Bamber, J. L. (2016). Emerging impact of Greenland meltwater on deepwater formation in the North Atlantic Ocean. *Nature Geoscience,* 9, 523–527.
6. Box, J. E. (2013). Greenland Ice Sheet Mass Balance Reconstruction. Part II: Surface Mass Balance (1840-2010)*. *Journal of Climate*, 26, 6974–6989.
7. Bracco, A., Pedlosky, J. and Pickart, R. S. (2008). Eddy Formation near the West Coast of Greenland. *Journal of Physical Oceanography,* 38, 1992–2002.

8. Brainerd, K. E. and Gregg, M. C. (1995). Surface mixed and mixing layer depths. *Deep-Sea Research I*, 42(9), 1521–1543.

9. Brandt, P., Schott, F. A., Funk, A. and Martins, C. S. (2004). Seasonal to interannual variability of the eddy field in the Labrador Sea from satellite altimetry. *Journal of Geophysical Research*, 109(C02028).

10. Chanut, J., Barnier, B., Large, W., Debreu, L., Penduff, T., Molines, J. M. and Mathiot, P. (2008). Mesoscale Eddies in the Labrador Sea and Their Contribution to Convection and Restratification. *Journal of Physical Oceanography*, 38,1617–1643.

11. Chelton, D. B., deSzoeke, R. A. and Schlax, M. G. (1998). Geographical Variability of the First Baroclinic Rossby Radius of Deformation. *Journal of Physical Oceanography*, 28,433–460.

12. Clarke, R. A. and Gascard, J.-C. (1983). The Formation of Labrador Sea Water. Part I: Large-Scale Processes. *Journal of Physical Oceanography*, 13,1764–1778.

13. Correlation Coefficient. Retrieved from https://www.mathworks.com/help/matlab/ref/corrcoef.html?requestedDomain=www.mathworks.com#bunkanr

14. Craig, A. P., Vertenstein, M., and Jacob, R. (2012). A new flexible coupler for earth system modeling developed for CCSM4 and CESM1. *The International Journal of High Performance Computing Applications*, 26(1), 31–42.

15. Cuny, J., Rhines, P. B., Niler, P. P. and Bacon, S. (2002). Labrador Sea Boundary Currents and the Fate of the Irminger Sea Water. *Journal of Physical Oceanography*, 32,627–647.

16. Delworth, T. L., Zeng, F., Vecchi, G. A., Yang, X., Zhang, L. and Zhang, R. (2016). The North Atlantic Oscillation as a driver of rapid climate change in the Northern Hemisphere. *Nature Geoscience,* 9.

17. Dickson, Robert R. and Brown, J. (1994). The production of North Atlantic Deep Water: Sources, rates and pathways. *Journal of Geophysical Research*, 99(C6), 12319–12341.

18. DuVivier, A., Cassano, J., Craig, A. P., Hamman, J., Maslowski, W., Nijssen, B., Osinski, R. and Roberts, A. (2016). Winter Atmospheric Buoyancy Forcing and Oceanic Response during Strong Wind Events around Southeastern Greenland in the Regional Arctic System Model (RASM) for 1990-2010. *Journal of Climate*, 29,975–994.

19. Eden, C. and Boning, C. (2002). Sources of Eddy Kinetic Energy in the Labrador Sea. *Journal of Physical Oceanography*, 32, 3346–3363.

20. Enderlin, E. M., Howat, I. M., Jeong, S., Noh, M.-J., van Angelen, J. H. and van den Broeke, M.R. (2014). An improved mass budget for the Greenland ice sheet. *Geophysical Research Letters*, 41, 866–872.

21. Ettema, J., van den Broeke, M. R., van Meijgaard, E., van de Berg, W. J., Bamber, J. L., Box, J. E. and Bales, R. C. (2009). Higher surface mass balance of the Greenland ice sheet revealed by high-resolution climate modeling. *Geophysical Research Letters*, 36(L12501).

22. Fettweis, X., Hanna, E., Lang, C., Belleflamme, A., Erpicum, M., and Gallee, H. (2013). Important role of the mid-tropospheric atmospheric circulation in the recent surface melt increase over the Greenland ice sheet. *The Cryosphere*, 7, 241–248.

23. Fettweis, X., Franco, B., Tedesco, M., van Angelen, J., Lenaerts, J.,van den Broeke, M., and Gallee, H. (2013). Estimating the Greenland ice sheet surface mass balance contribution to future sea level rise using the regional atmospheric climate model MAR. *The Cryosphere*, 7,469–489.

24. Freeland, Howard, Denman, Ken, Wong, C.S., Whitney, Frank, and Jacques, Renee. (1997). Evidence of change in the winter mixed layer in the Northeast Pacific Ocean. *Deep-Sea Research I*, 44(12), 2117-2129.

25. Gascard, J.-C. and Clarke, A. (1983). The Formation of Labrador Sea Water. Part II: Mesoscale and Smaller-Scale Processes. *Journal of Physical Oceanography*, 13, 1779–1797.

26. Gelderloos, R., Katsman, C. A., and Drijfhout, S. S. (2011). Assessing the Roles of Three Eddy Types in Restratifying the Labrador Sea After Deep Convection. J*ournal of Physical Oceanography,* 41,2102–2119.

27. Gerdes, R., Hurlin, W., and Griffies, S. M. (2006). Sensitivity of a global ocean model to increased run-off from Greenland. *Ocean Modelling*, 12, 416–435.

28. Gill., A. E. (1982). *Atmosphere-Ocean Dynamics*. Academic Press.

29. sen Gupta, A., Muir, L. C., Brown, J. N., Phipps, S. J., Durack, P. J., Monselesan, D. and Wijffels, S. E. (2012). Climate Drift in the CMIP3 Models. *Journal of Climate*, 25, 4621–4640.

30. Hanna, E., Huybrechts, P., Cappelen, J., Steffen, K., Bales, R. C., Burgess, E., McConnell, J. R., Steffensen, J. P., van den Broeke, M., Wake, L., Bigg, G., Griffiths, M., and Savas. D. (2011). Greenland Ice Sheet surface mass balance 1870-2010 based on Twentieth Century Reanalysis, and links with global climate forcing. *Journal of Geophysical Research*, 116(D24121).

31. Hanna, E., Jones, J. M., Mernild, S. H., Wood, L., Steffen, K. and Huybrechts, P. (2013). The Influence of North Atlantic Atmospheric and oceanic forcing effects on 1900-2010 Greenland summer climate and ice melt/runoff. *International Journal of Climatology*, 33, 862–880.

32. Hanna, E., Fettweis, X., Mernild, S. H., Cappelen, J., Ribergaard, M. H., Shuman, C. A., Steffen, K., Wooed, L. and Mote, T. L. (2014). Atmospheric and oceanic climate forcing of the exceptional Greenland ice sheet surface melt in summer 2012. *International Journal of Climatology*, 34, 1022–1037.

33. Hatun, H., Eriksen, C. C. and Rhines, P. B. (2007). Buoyant Eddies Entering the Labrador Sea Observed with Gliders and Altimetry. *Journal of Physical Oceanography*, 37, 2838–2854.

34. Holfort, J., Hansen, E., Osterhus, S., Dye, S., Jonsson, S., Meincke, J., Mortensen, J. and Meredith, M. (2008). Freshwater Fluxes East of Greenland. In Robert R. Dickson, Jens Meincke, and Peter Rhines (Eds.), *Arctic-Subarctic Ocean Fluxes: Defining the Role of the Northern Seas in Climate* (pp 263-287). Springer.

35. Holland, D. M., Thomas, R. H., De Young, B., Ribergaard, M. H. and Lyberth, B. (2008). Acceleration of Jakobshavn Isbrae triggered by warm subsurface ocean waters. *Nature Geoscience*, 1, 659-664.

36. Howat, I. M. and Eddy, A. (2011). Multi-decadal retreat of Greenland's marine-terminating glaciers. *Journal of Glaciology*, 57(203), 389–396.

37. Hurrell, J. W. (1995). Decadal trends in the north atlantic oscillation: regional temperatures and precipitation. *Science*, 269, 676–679.

38. Jakobsson, M., Cherkis, N., Woodward, J., Coakley, B., and Macnab, R. (2000). A new grid of Arctic bathymetry: A significant resource for scientists and mapmakers. *EOS Transactions, American Geophysical Union*, 81(9), 89,93,96.

39. Jones, Peter E. and Anderson, Leif G. (2008). Is the Global Conveyor Belt Threatened By Arctic Ocean Fresh Water Outflow. In Robert R. Dickson, Jens

Meincke, and Peter Rhines (Eds.), *Arctic-Subarctic Ocean Fluxes: Defining the Role of the Northern Seas in Climate*, (pp. 385-404). Springer.

40. de Jong, M., Bower, A. and Furey, H. (2014). Two Years of Observations of Warm-Core Anticyclones in the Labrador Sea and Their Seasonal Cycle in Heat and Salt Stratification. *Journal of Physical Oceanography*, 44, 427–444.
41. Junclaus, J.H., Haak, H., Esch, M., Roeckner, E. and Marotzke, J. (2006). Will Greenland melting halt the thermohaline circulation?. *Geophysical Research Letters*, 33(L17708).
42. Kantha, L. and Clayson, C. (2000). *Numerical Models of Oceans and Oceanic Processes*. Academic Press.
43. Katsman, C. A., Spall, M. A., and Pickart, R. S. (2004). Boundary Current Eddies and Their Role in the Restratification of the Labrador Sea. *Journal of Physical Oceanography*, 34, 1967–1983.
44. Kara, A. B., Rochford, P. A. and Hurlburt, H. E. (2003). Mixed layer depth variability over the global ocean. *Journal of Geophysical Research*, 108(C3,3079).
45. Kawasaki, T. and Hasumi, H. (2014). Effect of freshwater from the West Greenland Current on the winter deep convection in the Labrador Sea. *Ocean Modelling*, 75, 51–64.

46. Large, W., McWilliams, J. C. and Doney, S. (1994). Oceanic vertical mixing: A review and a model with a nonlocal boundary layer parameterization. *Reviews of Geophysics*, 32, 363–40.

47. Large, W., Danabasoglu, G. and Doney, S. C. (1997). Sensitivity to Surface Forcing and Boundary Layer Mixing in a Global Ocean Model: Annual-Mean Climatology. *Journal of Oceanography*, 27, 2418–2447.

48. Large, W. and Yeager, S. (2004). *Diurnal to Decadal Global Forcing for Ocean and Sea-Ice Models: The Data Sets and Flux Climatologies*. (NCAR Technical Note (NCAR/TN-460+STR). Climate and Global Dynamics Division, National Center for Atmospheric Research, Boulder, CO.

49. Large, W. and Yeager, S. (2009). The global climatology of an interannually varying air-sea flux data set. *Climate Dynamics*, 33, 341–364.

50. Lavender, K. L., Davis, R. E. and Owens, W. B. (2000). Mid-depth recirculation observed in the interior Labrador and Irminger seas by direct velocity measurements. *Nature*, 407.

51. Lazier, J. and Wright, D. (1993). Annual Velocity Variations in the Labrador Current. *Journal of Physical Oceanography*, 23, 659–678.

52. Lilly, J. M. and Rhines, P. B. (2002). Coherent Eddies in the Labrador Sea Observed from a Mooring. *Journal of Physical Oceanography*, 32, 585–598.

53. Lilly, J. M., Rhines, P. B., Schott, F., Lavender, K., Lazier, J., Send, U. and D'Asaro, E. (2003). Observations of the Labrador Sea eddy field. *Progress in Oceanography*, 59, 75–176.

54. Lorbacher, K., Dommenget, D., Niiler, P. and Kohl, A. (2006). Ocean mixed layer depth: A subsurface proxy of ocean-atmosphere variability. *Journal of Geophysical Research*, 111(C07010).

55. Luo, H., Bracco, A., and Di Lorenzo, E. (2011). The interannual variability of the surface eddy kinetic energy in the Labrador Sea. *Progress in Oceanography*, 91, 295–311.

56. Luo, H., Bracco, A. and Zhang, F. (2014). The Seasonality of Convective Events in the Labrador Sea. *Journal of Climate*, 27, 6456–6471.

57. Luo, H., Castelao, R. M., Rennermalm, A. K., Tedesco, M., Bracco, A., Yager, P. L. and Mote, T. L. (2016). Oceanic transport of surface meltwater from the southern Greenland ice sheet. *Nature Geoscience,* 9, 528–533.

58. Marsh, R., Desbruyeres, D., Bamber, J., de Cuevas, B. A., Coward, A. and Aksenov, Y. (2010). Short-term impacts of enhanced Greenland freshwater fluxes in an eddy-permitting ocean model. *Ocean Science*, 6, 749–760.

59. Maslowski, W., Clement Kinney, J., Marble, D. C. and Jakacki, J. (2008). Towards Eddy-Resolving Models of the Arctic Ocean. In M. W. Hecht and H. Hasumi (Eds.), *Ocean Modeling in an Eddying Regime*. American Geophysical Union.

60. Mauritzen, C. (1996). Production of dense overflow waters feeding the North Atlantic across the Greenland-Scotland Ridge. Part 1: Evidence for a revised circulation scheme. *Deep-Sea Research I*, 43(6), 769–806.

61. McCartney, M.S. and Curry, R.G. (1996). Labrador Sea Water Carries Northern Climate Signal South: Subpolar Signal Appears Years Later at Bermuda. *Oceanus Magazine,* 39(2). Retrieved from http://www.whoi.edu/oceanus/feature/labrador-sea-water-carries-northern-climate-signal-south

62. McDougall, T. J., Jackett, D. R., Wright, D. G. and Feistel, R. (2003). Accurate and Computationally Efficient Algorithms for Potential Temperature and Density of Seawater. *Journal of Atmospheric and Oceanic Technology,* 20, 730–741.

63. McGeehan, T. and Maslowski, W. (2011). Impact of Shelf-Basin Freshwater Transport on Deep Convection in the Western Labrador Sea. *Journal of Physical Oceanography*, 41, 2187–2210.

64. Melling, H. (2012). Sea-Ice Observation: Advances and Challenges. In P. Lemke and H.-W. Jacobi (Eds.), *Arctic Climate Change: The ACSYS Decade and Beyond*, (pp.27-114). Springer.

65. Mjell, T. L., Ninnemann, U. S., Kleiven, H. F. and Hall, I. R. (2016). Multidecadal changes in Iceland Scotland Overflow Water vigor over the last 600 years and its relationship to climate. *Geophysical Research Letters*, 43, 2111–2117.

66. Montegut, C. d. B., Madec, G., Fischer, A. S., Lazar, A. and Iudicone, D. (2004). Mixed layer depth over the global ocean: An examination of profile data and a profile-based climatology. *Journal of Geophysical Research*, 109(C12003).

67. Monterey, G. I., & Levitus, S. (1997). Climatological cycle of mixed layer depth in the world ocean. US Government Printing Office, NOAA NESDIS, 5.

68. Moon, T. and Joughin, I. (2008). Changes in ice front position on Greenland's outlet glaciers from 1992 to 1997. *Journal of Geophysical Research*, 113(F02022).

69. Moon, T., Joughin, I., Smith, B. and Howat, I. (2012). 21st-Century Evolution of Greenland Outlet Glacier Velocities. *Science*, 336, 576–578.

70. Moore, G., Pickart, R., Renfrew, I. and Vage, K. (2014). What causes the location of the air-sea turbulent heat flux maximum over the Labrador Sea? *Geophysical Research Letters*, 41, 3628–3635.

71. Moore, G., Vage, K., Pickart, R. and Renfrew, I. (2015). Decreasing intensity of open-ocean convection in the Greenland and Iceland seas. *Nature Climate Change*, 5, 877–882.

72. Myers, P. G. (2005). Impact of freshwater from the Canadian Arctic Archipelago on Labrador Sea Water formation. *Geophysical Research Letters*, 32(L06605).

73. Myers, P. G., Donnelly, C., and Ribergaard, M. H. (2009). Structure and variability of the West Greenland Current in Summer derived from 6 repeat standard sections. *Progress in Oceanography*, 80, 93–112.

74. Neelin, D. J. (2011). *Climate Change and Climate Modeling.* Cambridge University Press.

75. Nick, F. M., Luckman, A., Vieli, A., van der Veen, C., van As, D., van del wal, R.S.W., Pattyn, F., Hubbard, A. and Floricioiu, D. (2008). The response of Petermann Glacier, Greenland, to large calving events, and its future stability in the context of atmospheric and oceanic warming. *Journal of Glaciology*, 58(208).

76. Nurser, A. and Bacon, S. (2014). The Rossby Radius in the Arctic Ocean. *Ocean Science*, 10, 967–975.

77. Osinski, R., Rak, D., Walczowski, W. and Piechura, J. (2010). Baroclinic Rossby Radius of Deformation in the Southern Baltic Sea. *Oceanologia*, 52, 417–429.

78. Parkinson, C. L., Cavalieri, D. J., Gloersen, P., Jay, Z. H., and Comiso, J. C. (1999). Arctic sea ice extents, areas, and trends, 1978-1996. *Journal of Geophysical Research*, 104(C9), 202837–20856.

79. Physical Oceanographic Monitoring of the Labrador Sea. (2015). Retrieved from http://www.bio.gc.ca/science/monitoring-monitorage/azomp-pmzao/labrador/physical-physique-en.php

80. Pickart, R. S. and Smethie, W. M. J. (1998). Temporal evolution of the deep western boundary current where it enters the sub-tropical domain. *Deep Sea Research I*, 45, 1053–1083.

81. Pickart, R. S., Torres, D. J., and Clarke, R. A. (2002). Hydrography of the Labrador Sea during Active Convection. *Journal of Physical Oceanography*, 32, 428–457.

82. Rahmstorf, S. (1995). Bifurcations of the Atlantic thermohaline circulation in response to changes in the hydrological cycle. *Nature*, 378, 145–149.

83. Rainville, L. and Pinkel, R. (2006). Propagation of Low-Mode Internal Waves through the Ocean. *Journal of Physical Oceanography*, 36, 1220–1236.

84. Rattan, S., Myers, P. G., Treguier, A. M., Theetten, S., and Biastoch, A. (2010). Towards an understanding of Labrador Sea salinity drift in eddy-permitting simulations. *Ocean Modelling*, 35, 77–88.

85. Roberts, A., Craig, A. P., Maslowski, W., Osinski, R., DuVivier, A., Hughes, M., Nijssen, B., Cassano, J., and Brunke, M. Simulating transient ice-ocean Ekman transport in the Regional Arctic System Model and Community Earth System Model. *Annals of Glaciology*, 56(69), 211–228.

86. Rykova, T., Straneo, F., Lilly, J. M. and Yashayaev, I. (2009). Irminger Current Anticyclones in the Labrador Sea observed in the hydrographic record, 1990-2004. *Journal of Marine Research*, 67, 361–384.

87. Rykova, T. (2010). *The Seasonal and Interannual Variability of the West Greenland Current System in the Labrador Sea* (Doctoral dissertation). Massachusetts Institute of the Technology and the Woods Hole Oceanographic Institution. Retrieved from http://hdl.handle.net/1721.1/59755

88. Rykova, T., Straneo, F. and Bower, A. S. (2015). Seasonal and interannual variability of the West Greenland Current System in the Labrador Sea in 1993-2008. *Journal of Geophysical Research: Oceans*, 120, 1318– 1332.

89. Saenko, O. A. (2006). Influence of Global Warming on Baroclinic Rossby Radius in the Ocean: A Model Intercomparison. *Journal of Climate*, 19, 1354–1360.

90. Saenko, O. A., Dupont, F., Yang, D., Myers, P. G., Yashayaev, I. and Smith, G. C. (2014). Role of Resolved and Parameterized Eddies in the Labrador Sea Balance of Heat and Buoyancy. *Journal of Physical Oceanography*, 44, 3008–3032.

91. Schmidt, S. and Send, U. (2007). Origin and Composition of Seasonal Labrador Sea Freshwater. *Journal of Physical Oceanography*, 37, 1445–1454.

92. Semtner, A. J. and Chervin, R. M. (1988). A simulation of the global ocean circulation with resolved eddies. *Journal of Geophysical Research*, 93(C12), 15502–15522.

93. Serreze, M. C. and Barry, R. G. (2011). Processes and impacts of Arctic amplification: A research synthesis. *Global and Planetary Change*, 77, 85–96.

94. Simonsen, K. and Haugan, P. M. (1996). Heat budgets of the Arctic Mediterranean and sea surface heat flux parameterizations for the Nordic Seas. *Journal of Geophysical Research*, 101(C3), 6553–6576.

95. Smedsrud, L. H., Esau, I., Ingvaldsen, R. B., Eldevik, T., Haugan, P. M., Li, C., Lien, V. S., Olsen, A., Abdirahman, Omar M., Ottera, O. H., Risebrobakken, B.,

Sando, A. B., Vladimir, Semenov A. and Sorokina, S. A. (2013). The role of the Barents Sea in the Arctic climate system. *Review of Geophysics*, 51, 415–449.

96. Smith, R. D., Dukowicz, J. K., and Malone, R. C. (1992). Parallel ocean general circulation modeling. *Physica D*, 60, 38–61.
97. Srokosz, M., Baringer, M., Bryden, H., Cunningham, S., Delworth, T., Lozier, S., Marotzke, J. and Sutton, R. (2012). Past, Present and Future Changes in the Atlantic Meridional Overturning Circulation. *Bulletin of the American Meteorological Society*, (1663-1676).
98. Stramma, L., Kieke, D., Rhein, M., Schott, F., Yashayaev, I. and Koltermann, K. P. (2004). Deep water changes at the western boundary of the subpolar North Atlantic during 1996-2001. *Deep-Sea Research I*, 51, 1033– 1056.
99. Steele, M., Morley, R., and Ermold, W. (2001). PHC: A Global Ocean Hydrography with a High-Quality Arctic Ocean. *Journal of Climate*, 14.
100. Stewart, Robert H. (2009). *Introduction to Physical Oceanography*. Available from http://www.colorado.edu/oclab/sites/default/files/attached-files/stewart_textbook.pdf
101. Straneo, F. (2006) Heat and Freshwater Transport through the Central Labrador Sea. *Journal of Physical Oceanography,* 36, 606–628.
102. Talley, L. and McCartney, M. S. (1982). Distribution and Circulation of Labrador Sea Water. *Journal of Physical Oceanography*, 12, 1189–1205.

103. Thomson, R. E. and Fine, I. V. (2003). Estimating Mixed Layer Depth from Oceanic Profile Data. *Journal of Atmospheric and Oceanic Technology*, 20, 319–329.

104. Thomson, R. E. and Fine, I. V. (2009). A Diagnostic Model for Mixed Layer Depth Estimation with Application to Ocean Station P in the Northeast Pacific. *Journal of Physical Oceanography*, 39, 1399–1415.

105. Vage, K., Pickart, R. S., Thierry, V., Reverdin, G., Lee, C., Petrie, B., Agnew, T., Wong, A., and Ribergaard, M. H. (2009). Surprising return of deep convection to the subpolar North Atlantic Ocean in winter 2007- 2008. *Nature Geoscience*, 2, 67–72.

106. Vage, K., Pickart, R. S., Sarafanov, A., Knutsen, O., Mercier, H., Lherminier, P., van Aken, H. M., Meincke, J., Quadfasel, D., and Bacon, S. (2011). The Irminger Gyre: Circulation, convection, and interannual variability. *Deep-Sea Research I,* 58, 590–614.

107. Velicogna, I. (2009). Increasing rates of ice mass loss from the Greenland and Antarctic ice sheets revealed by GRACE. *Geophysical Research Letters*, 36(19), L19503.

108. Visbeck, Martin, Marshall, John, and Jones, Helen. (1996). Dynamics of Isolated Convective Regions in the Ocean. *Journal of Physical Oceanography,* 26, 1721-1734.

109. Vizcaino, M., Lipscomb, W. H., Sacks, W. J., van Angelen, J. H., Wouters, B., and van den Broeke, M. R. (2013). Greenland Surface Mass Balance as Simulated by the Community Earth System Model. Part 1: Model Evaluation and 1850-2005 Results. *Journal of Climate*, 26:7793–7812.

110. Vizcaino, M., Lipscomb, W. H., Sacks, W. J., and van den Broeke, M. R. (2014). Greenland Surface Mass Balance as Simulated by the Community Earth System Model. Part II: Twenty-First-Century Changes. *Journal of Climate,* Special Collection, 215–226.

111. Wain, D. J., Lilly, J. M., Callaghan, A., Yashayaev, I., and Ward, B. (2015). A breaking internal wave in the surface ocean boundary layer. *Journal of Geophysical Research: Oceans*, 120, 4151–4161.

112. Wallace, J. M. and Gutzler, D. S. (1981). Teleconnections in the Geopotential Height Field during the Northern Hemisphere winter. *Monthly Weather Review*, 109, 784–812.

113. Wolfe, Christopher, L. and Cenedese, C. (2006). Laboratory Experiments on Eddy Generation by a Buoyant Coastal Current Flowing Over Variable Bathymetry. *Journal of Physical Oceanography*, 36, 395–411.

114. World Data Service for Geophysics. *5-Minute Gridded Global Relief Data Collection (ETOPO5)*. Retrieved from https://www.ngdc.noaa.gov/mgg/fliers/93mgg01.html

115. Xie, P. and Arkin, P. A. (1996). Analyses of Global Monthly Precipitation Using Gauge Observations, Satellite Estimates, and Numerical Model Predictions. *Journal of Climate*, 9, 840–858.

116. Xu, X., Rhines, P. B., Chassignet, E. P., and Schmitz Jr, W. J. (2015). Spreading of Denmark Strait Overflow Water in the western subpolar North Atlantic: Insights from eddy-resolving simulations with a passive tracer. *Journal of Physical Oceanography,* 45, 2913–2932.

117. Yang, X., Rial, J., and Reischmann, E. P. (2014). On the bipolar origin of Heinrich events. *Geophysical Research Letters*, 41, 9080–9086.

118. Yashayaev, I. (2007). Hydrographic changes in the Labrador Sea, 1960-2005. *Progress in Oceanography*, 73, 242-276.

119. Yashayaev, I. and Clarke, A. (2008). Evolution of North Atlantic Water masses inferred from Labrador Sea salinity series. *Oceanography*, 21.

120. Yashayaev, I. and Loder, J. W. (2009). Enhanced production of Labrador Sea Water in 2008. *Geophysical Research Letters,* 36(L01606).

121. Yu, L., Gao, Y., and Ottera, O. H. (2016). The sensitivity of the Atlantic meridional overturning circulation to enhanced freshwater discharge along the entire, eastern and western coast of Greenland. *Climate Dynamics*, 46, 1351–1369.